Important Notice

UNIVERSITY OF CALGARY

Seismic modelling of CO_2 in a sandstone aquifer, Priddis, Alberta

by

Virginia Cecilia Vera

A THESIS

SUBMITTED TO THE FACULTY OF GRADUATE STUDIES

IN PARTIAL FULFILMENT OF THE REQUIREMENTS FOR THE

DEGREE OF MASTER OF SCIENCE

DEPARTMENT OF GEOSCIENCE

CALGARY, ALBERTA

FEBRUARY, 2012

UNIVERSITY OF CALGARY

FACULTY OF GRADUATE STUDIES

The undersigned certify that they have read, and recommend to the Faculty of Graduate Studies for acceptance, a thesis entitled "Seismic modelling of CO_2 in a sandstone aquifer, Priddis, Alberta" submitted by Virginia Cecilia Vera in partial fulfilment of the requirements of the degree of Master of Science.

_____
Supervisor, Dr. Donald C. Lawton,
Department of Geoscience

_____
Dr. Laurence R. Lines,
Department of Geoscience

_____
Dr. Ron K. Wong
Department of Civil Engineering

_____
Date

Abstract

The CO_2 storage potential of a shallow sandstone layer of the Paskapoo Formation, southwest of Calgary, was evaluated in this thesis. In order to assess the CO_2 monitoring viability, Gassmann fluid substitution was undertaken, followed by 2D and 3D seismic modeling in the study area. From the Gassmann approach, considerable changes of velocity and density were found with increasing CO_2 saturation. In addition, Amplitude versus offset (AVO) analysis proved to be sensitive for detecting saturation changes, especially through the evaluation of Shuey's parameters. From the seismic modelled volumes, a difference in seismic amplitude was recognized. As well, time delays of the reflectors in the injection zone and below were measured. The reflectivity coefficient decreased approximately 30% and the time delay is about 1 ms. The changes caused by the presence of CO_2 are identifiable by subtracting the monitor model data from the baseline model data. These models and simulations demonstrate the feasibility of using the Basal Paskapoo Fm. as a CO_2 storage site, given its petrophysical, stratigraphic and geological characteristics. The proposed amount of CO_2 injection is 3000 tonnes (5 injections of 600 tonnes each), a mass that can be resolved using the seismic method. Following volumetric calculations and seismic parameters it was possible to postulate that 300 tonnes of CO_2 could be detected by time-lapse seismic analysis.

Dedication

To my mom, Belkys Gonzalez and my dad, Samuel Vera

Table of Contents

Table of Contents

List of Tables

List of Figures and Illustrations

List of Symbols, Abbreviations and Nomenclature

RMS	Root Mean Square
CDP	Common Depth Point
NMO	Normal Move Out
MPA	Middle Paskapoo Sandstone A
MPB	Middle Paskapoo Sandstone B
LP	Lower Paskapoo
E	Edmonton
UD	Upper Dettachment
LD	Lower Detachment
BR	Belly River
MR	Milk River
C	Cardium
M	Mississipian
2D	Two-dimensional
3D	Three-dimensional
3C	Three-Component
G	Shear modulus
K	Bulk modulus
K_{sat}	Saturated rock bulk modulus
K^*	Dry rock bulk modulus
K_{fl}	Fluid bulk modulus
ρ	Density
V_p	P-wave velocity
V_s	S-wave velocity
A	AVO intercept
B	AVO gradient
r	Radius

Chapter One: Introduction

1.1 CO_2 Storage in Geological Formations and Seismic Monitoring

1.1.1 Problem Overview

The fast increase in greenhouse gases concentration and hypothesized global warming constitute one of society's major concerns presently. The increase of CO_2 in the atmosphere is considered by many to be the principal cause of global warming, affecting the natural equilibrium. CO_2 sequestration in geological formations represents a viable solution or at least a way of mitigation. The goal of this method is to capture CO_2 produced by anthropogenic or natural point sources and inject it into a porous layer surrounded by non-porous layers to trap the gas (Hovorka, 2008).

Using carbon capture and storage (CCS) to decrease the emissions of CO_2 in the atmosphere was proposed in the 1970's and got more relevance by the late 1980's (Benson, 2008). This technology arises as a feasible option to address issues related to the 20 billion tons of CO_2 emitted per year; this number is expected to increase in the near future (Benson, 2008). CCS represents a possibility of transition from today's high emission world to a low emission scenario, providing a chance to keep using proven fossil fuel reserves, but also start the implementation of "green" combustibles (Benson, 2008).

Some of the most important projects functioning and currently injecting millions of tons of CO_2 are Sleipner (North Sea), In Salah (Algeria), Snohvit (Norway), San Juan Basin (New Mexico) and Weyburn (Canada). These big scale projects have been undertaken by oil and gas companies, but there are many other small scale projects that attempt to perform a more detailed evaluation and study of the effects of injecting CO_2 in geological formations. An example is the CO_2MAN in Ketzin site, Germany (Wuerdemann et al., 2010). The four main objectives of CO_2MAN are: monitoring the injected CO_2, characterizing the reactions of the CO_2 with the surrounded media, confirming the effectiveness of the previous simulation and informing the public about the obtained results (Wuerdemann et al., 2010).

Carbon Management Canada Board in partnership with the University of Calgary (Institute for Sustainable Energy, Environment and Economy (ISEEE) and CREWES) proposed a project similar to CO_2MAN in Ketzin, where a reduced amount of CO_2 will be injected and monitored in a specific site in Alberta. The target is a shallow sandstone layer and the selected site was on university land south west of Calgary, near Priddis.

There are different types of geological sites that enable the storage of CO_2: depleted hydrocarbon reservoirs, coal bed methane, sandstone aquifers and carbonate rock. It is easy to understand that the most suitable site will be depleted hydrocarbon reservoirs. The injection in these sites is related to enhanced oil recovery (EOR) technique where it is known that the trap is effective in all directions. Nevertheless, the availability of these sites is limited; therefore, another option in terms of storage capacity is sandstone aquifers (Benson, 2008). Sandstone aquifers are located all over the world and their benefits include high permeability and the possibility of dissolution of the CO_2 in the formation water.

The CCS process is composed of four main steps: capture, compression, pipeline transport and underground injection. The objective of this dissertation is related to the fourth step, specifically to the prior injection modelling and assessment. CCS involves a wide range of disciplines and efforts from engineering to science. Geophysics is used for evaluation and for monitoring the injected CO_2 plume. The main tool applied by geophysicists is the seismic method, by comparing and analysing the difference in seismic images and seismic patterns before and after injecting CO_2 underground (time-lapse seismic surveys).

1.1.2 Injection in Sandstone Aquifers

As mentioned previously, the injection of CO_2 in sandstone aquifers is one of the most feasible storage targets, in terms of safe trapping and capacity. The CO_2 storage in deep aquifers is based on high porosity and permeability of the sandstone target which can be filled with the injected fluid. The CO_2 can be dissolved in the formation water (approximately 30%) and it can produce mineralization in the presence of high salinity water (Benson, 2008).

The architecture of an ideal sandstone aquifer for CO_2 storage is that it is overlaid by a series of aquitards, and particularly an impermeable layer that stops the upward flow of CO_2 (Bachu et al., 2000). These layers are mostly composed of shale or evaporitic deposits. The injected CO_2 plume will migrate according to natural hydrodynamics and the fluid buoyancy in relation with the surrounding water (Bachu et al., 1994). The dispersion caused by buoyancy will be smaller when the density difference between the injected CO_2 and the formation water is low.

1.1.3 Alberta Carbon Capture and Storage (CCS) Potential

Alberta CO_2 emissions are one of the highest in Canada, with a fast rate of increase. This is given by the production of fossil fuels, power-generation plants and oil sands production among others sources (126 Mt, or 27.5% of total Canadian emission) (Bachu et al., 2000). The most feasible solution to reduce these high rates is carbon storage in geological formations. The conditions that are required by a site for this purpose are: geological stability, adequate hydrological conditions, mature oil and gas basin (use of EOR) and economic recourses to undertake projects of high investment (Bachu et al., 2000).

The Alberta Basin meets all of these conditions. It is located in the foreland basin in the eastern flank of the Rocky Mountains and corresponds to a stable Precambrian platform very distant from tectonic plate convergence; therefore, it has no risk of earthquakes, volcanism or any other orogenic event (Bachu et al., 2000). In terms of stratigraphy, from the Upper Jurassic to Tertiary, the deposits are mostly represented by thin sandstone layers intercalated with thick shale deposits. In terms of hydrological conditions, the Alberta Basin contains many aquifer reserves especially in the southern area (Bachu et al., 2000). For depleted hydrocarbon sites, the Alberta basin has already reached its maturity and at least 35 % of its reserves have been produced (Bachu et al., 2000). Therefore, former oil traps can be now used for CO_2 storage.

For this dissertation, the emphasis will be made in the south-western Alberta potential, specifically CO_2 storage in sandstone hosted aquifers. This region is located at the edge of the deformed area of the Rocky Mountain Foothills; it is classified as very

extremely suitable zone for CO_2 sequestration (Bachu et al., 2000), as it has all confined aquifers in Upper Cretaceous formations as well as deep basin deposits, depleted oil and gas reservoirs and deep unmineable coalbeds (Bachu and Gunter, 1999).

1.1.4 Seismic Method for Monitoring CO₂ Storage

Geophysical techniques have been historically related to the hydrocarbon exploration and production. The seismic technology applied for monitoring injected CO_2 follow the same principles used for EOR. The monitoring of the CO_2 plume is a very important issue due to regulations established in order to assure the safety of large storage sites and the nearby areas (Freifelda, 2009). There are several techniques involved in monitoring during the CO_2 injection process, most of them related to borehole measurements such as well logging (porosity, temperature, pressure, velocity, formation microimager) and biochemical assessments. However a large-scale study that can give information about the size, shape and position of the plume can only be achieved by seismic surveys. It is important to mention that potential methods such as gravimetric and magnetic play an important role in identifying the differences in properties caused by plume expansion but they yield a much lower spatial resolution than the seismic method (Chadwick et al., 2006).

Monitoring using the seismic method attempts identifying the CO_2 plume in the seismic images resulting from the difference between the seismic data acquired before and after injection. What it is expected from this difference is a series of sub-horizontal high amplitude reflections with an underlying velocity pushdown (Chadwick et al., 2006). An important example of monitoring large scale CO_2 injection in a saline sandstone aquifer is given by the Sleipner Project in Norway. This initiative is driven by Statoil, with the Utsira Formation sandstone as the target unit (200-250 m thickness and 800-100m depth). This project demonstrates the viability of monitoring the CO_2 plume through the seismic method by identifying the amplitude difference and velocity pushdown caused by the velocity reduction in the presence of CO_2-saturated rock. Utsira sandstone is a relatively shallow formation which facilitates the monitoring (Chadwick et al., 2006).

The main objectives of monitoring CO_2 storage are: to demonstrate the safe storage of the CO_2 in the selected geological formation, to image the location and migration path of the injected CO_2 and finally a guarantee of early detection of any leakage potential (Chadwick et al., 2006). In order to evaluate the CO_2 plume, time-lapse images have to be generated. Therefore a seismic survey needs to be acquired before and after injection with the same survey design. The initial pre-injection survey will be the base or reference 2D line or 3D volume, depending on the scope. The next surveys would be obtained at different times with several years apart.

Before undertaking a time-lapse survey, seismic models are generated in order to estimate the expected outcome. Forward modelling is undertaken where, knowing the physical properties of the rocks, the amount of CO_2 and some historical results, the shape and characteristic of the plume can be calculated and implemented in a geological and seismic simulation (Chadwick et al., 2006). On the other hand, when the time-lapse seismic data are already available, the type of modelling to apply will be inverse modelling. In this case, from the reflectivity and velocity pushdown values are used to calculate the amount and distribution of the CO_2. For this dissertation, to forward modelling was undertaken in order to estimate the CO_2 plume geometry and simulate its seismic time-lapse response.

1.2 Study Site

The study site is on University of Calgary land near Priddis, a small community located in the Rocky Mountains Foothills, Southwest of Calgary (Figure 1-1). This area is part of the eastern flank of the Rocky Mountains and is specifically located southwest of the intersection of the Cowboy Trail and Highway 22X, approximately 10 kilometres west of Calgary's city limits.

The area evaluated for injection is located next to the Rothney Astrophysical Observatory (RAO). This land was previously donated to the University of Calgary. At this site several useful research projects have been undertaken in order to characterize this zone, using multi-component seismic and vertical seismic profiles (VSP) (Lawton et al., 2008).
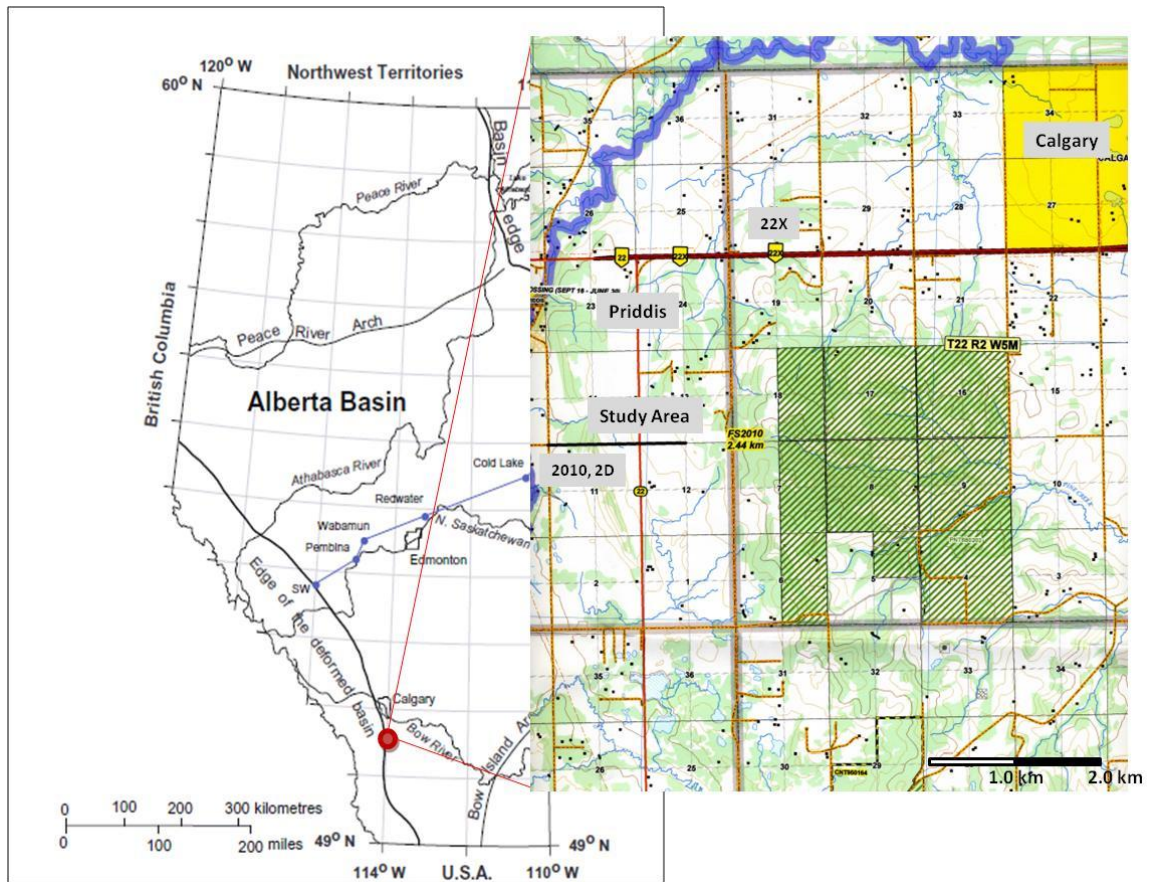
Figure 1-1: Study area location. Location in Alberta (from Bachu et al., 2000) and detail view (Modified from Priddis 2010-1 2D preliminary plan, courtesy of OutSource Seismic).

1.3 Well Data

Isaac and Lawton (2009) identified four wells located close to the area of study. These wells intersect the main formation tops and the possible target. These wells are: 7-1-023-2W5, 12-33-21-2W5, 10-22-21-2W5 and 2-33-021-2W5 (Figure 1-2). The closest well to the area of study is 12-33-21-2W5, approximately 6 km from the site. Isaac and Lawton (2010) analysed this set of wells and generated a cross-section A-A' going from south to north (Figure 1-3). Eight horizons were identified using sonic, and gamma-ray logs. These were the Middle Paskapoo sandstone "A" (MPA), Middle Paskapoo sandstone "B" (MPB), Lower Paskapoo (LP), Edmonton Group (E), Belly River (BR), Milk River (MR), Cardium (C) and Missisipian (M).

From the data, a fairly consistent sand body classified as Lower Paskapoo sandstone was mapped, and this unit is thought to extend regionally. Overlying the Lower Paskapoo sandstone there is a layer of low velocity and high gamma-ray response that can be interpreted as shale, followed upwards by more sandstone, and finally a shalier section at about 750m. This sequence is identified as the Basal Paskapoo Fm., and underlying the Lower Paskapoo Fm. is the Edmonton Group.
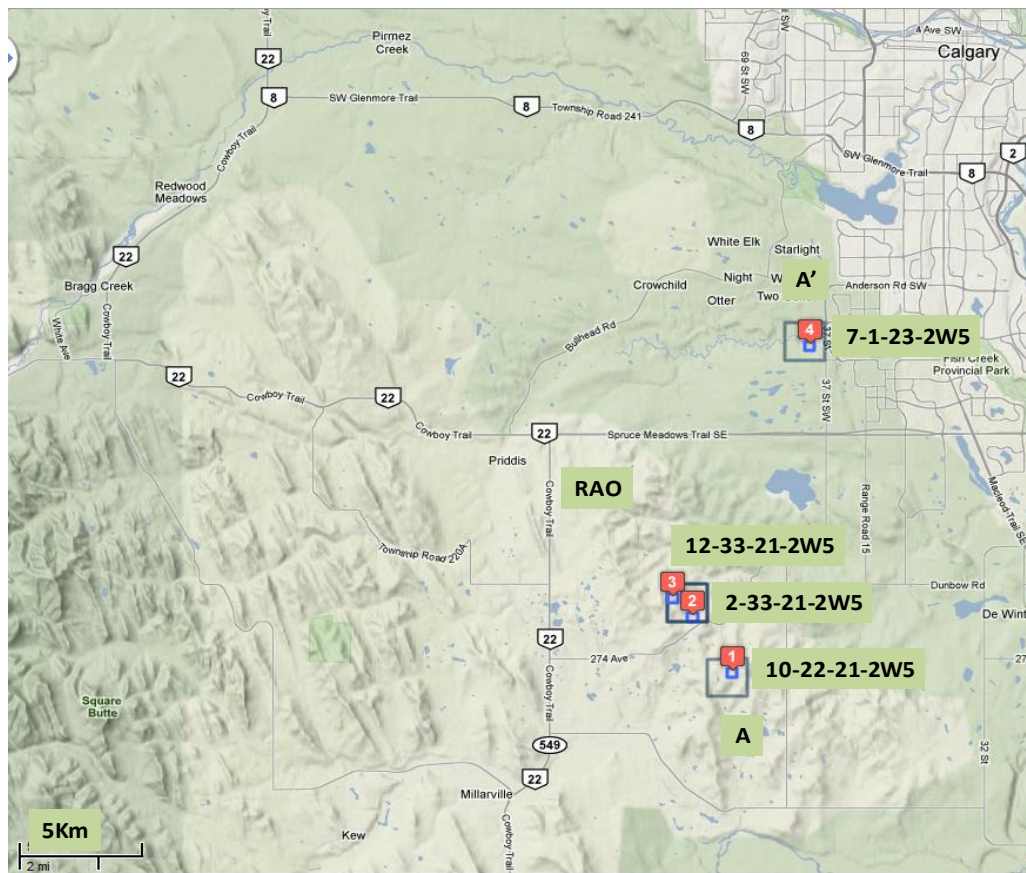
Figure 1-2: Location of the wells: 7-1-023-2W5, 12-33-21-2W5, 10-22-21-2W5 and 2-33-021-2W5 and the A-A' cross-section. The study area is identified by RAO (http://www.baseloc.com/dls/#).
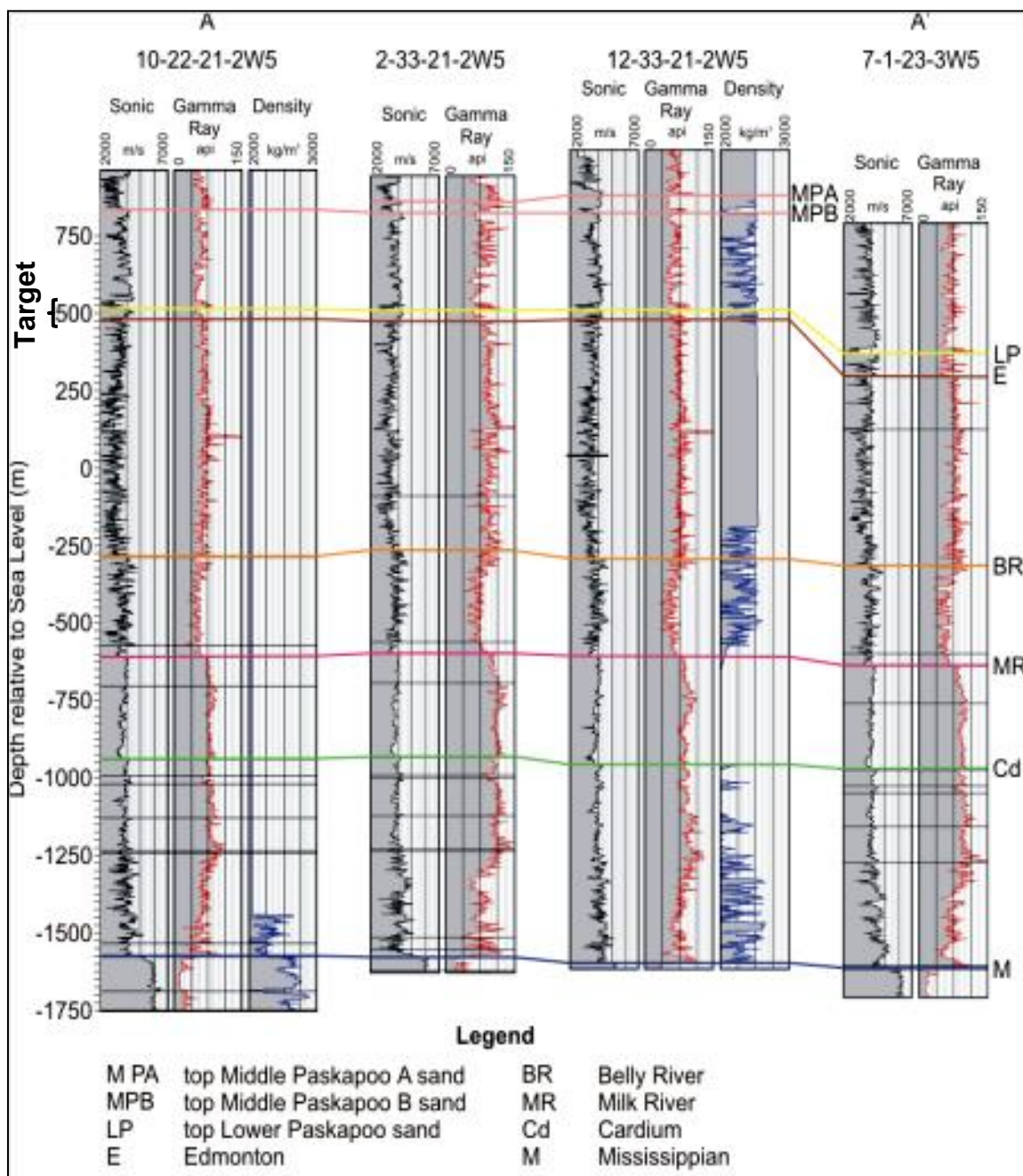
Figure 1-3: Cross-section A-A' with the four wells in the area. Note: that Lower Paskapoo sandstone presents consistent gamma-ray and sonic log characteristic. Target interval between LP and E (Modified from Isaac and Lawton, 2010).

1.4 Structure and Stratigraphy

1.4.1 Geological Framework

The study area is located at the eastern edge of the Rocky Mountain foothills in the triangle zone. This zone is between Jumping Pound and Wildcat Hills, Alberta (Slotboom et al., 1996). It is characterized by a blind thrust in the leading edge of the Rocky Mountain fold and thrust belt. In this zone the strata has wedged into the foreland succession with a blind frontal tip (Slotboom et al., 1996). The geometry of the area is defined by an amorphous flat base, beds and faults dipping toward the hinterland on the western side and some slight foreland dips on the eastern side, forming a triangle zone (Slotboom et al., 1996). Triangle zones are characterized by faults with opposite slip directions. They are related to a common lower detachment, so these faults and the lower detachment represent the triangle zone (Slotboom et al., 1996).

Cretaceous and early Tertiary rocks were deposited by the end of Laramide Orogeny phase and the beginning of the tectonic extension in the Tertiary (Dawson et al., 2008). These sediments came from a non-marine environment to the west, passing to a marine environment towards the east. This stratigraphic section covers four periods of clastic deposition composed of: Belly River, Horseshoe Canyon, Scollar and Paskapoo and four intervals of limited clastics composed of the Pakowki, Bearpaw and Battle formations (Dawson et al., 2008).

1.4.2 Stratigrapy

Three tectonostratigraphic units form the triangle zone in this area: Precambrian crystalline basement, Palaeozoic carbonate group and Mesozoic and Early Tertiary age clastic group (Slotboom et al., 1996). Figure 1-4 displays the stratigraphic column of the area. Mesozoic stratigraphic sequences present contain deformation associated with the triangle zone formation. This section is composed of inter-bedded sandstone, siltstone, shales and coals from the foreland molasse strata. These sediments were uplifted due to a series of compressional episodes that shortened and thickened the sediments in the

western margin of the craton during formation of the Canadian Cordillera (Stockmal et al., 1996).

Turonian (Cardium Formation) through Paleocene (Porcupine Hills Formation) strata correspond with foreland siliciclastic basin from marine to nonmarine sediments and some fresh water limestone (Stockmal et al., 1996). The sequence of sediments is formed of: marine to nonmarine Milk River Formation strata and marine Pakowki Formation and nonmarine Belly River Group rocks. St. Mary River Formation and Willow Creek Formation present a thickening due to considerable deformation related to the upper detachment of the triangle zone.

1.4.3 Paskapoo Formation

The Paskapoo Formation represents the sequence of interest in this study. It is a Tertiary Formation composed of continental to alluvial plain deposits of mudstone, siltstone and sandstone, with subordinate limestone and coal. Figure 1-4 is the stratigraphic sequence showing Paskapoo as an aquifer overlain by Quaternary deposits with an uncorformity. It covers most of the Interior Plains area having as correlative strata the Coalspur Formation out of the foothills towards the north (Dawson et. al, 2008). The sandstone grades to conglomerate in places, and bentonite beds are also present. The strata represent a foreland deposit of a siltstone- and mudstone-dominated fluvial system (Grasby et al., 2008). This Formation constitutes an important ground water reservoir having some high-porosity coarse-grained sandstone channels (Grasby et al., 2008). The basal Haynes Member and western portion of the Paskpaoo Formation have higher sandstone volumes than other portions of the system (Grasby et al., 2008)

The Paskapoo Formation currently represents the youngest bed rock deposits in the Western Canada Sedimentary Basin having from 0 to 800m of thickness with a thinner section in the eastern part (Grasby et al., 2008). The deposits are distributed in an asymmetric foreland basin developed between the deforming mountain front and the adjacent craton due to the western thrusting of the Rocky Mountains (Grasby et al., 2008). The main source of sediments was the Palaeozoic-Mesozoic emerging the Rocky Mountains. The strata are composed of greenish sandy siltstone and mudstone, with light

grey, thick-bedded sandstone deposited in non-marine environments (Grasby et al., 2008). A plain zone where the strata are dipping westward, forming a homoclinal wedge into Alberta syncline, is called Paskapoo Sandstone, which has the most representative sandstone channels. Outside this sandy zone, the formation is composed of more than 50% siltstone and mudstone (Grasby et al., 2008). The formation disconformably overlays fine-grained deposits with abundant coal of the upper Cretaceous Edmonton Group (Lerbekmo et al., 1990; Demchuk and Hills, 1991). Paskapoo top is overlaid by unconsolidated upper Tertiary and Quaternary deposits (Dawson et. al, 2008).
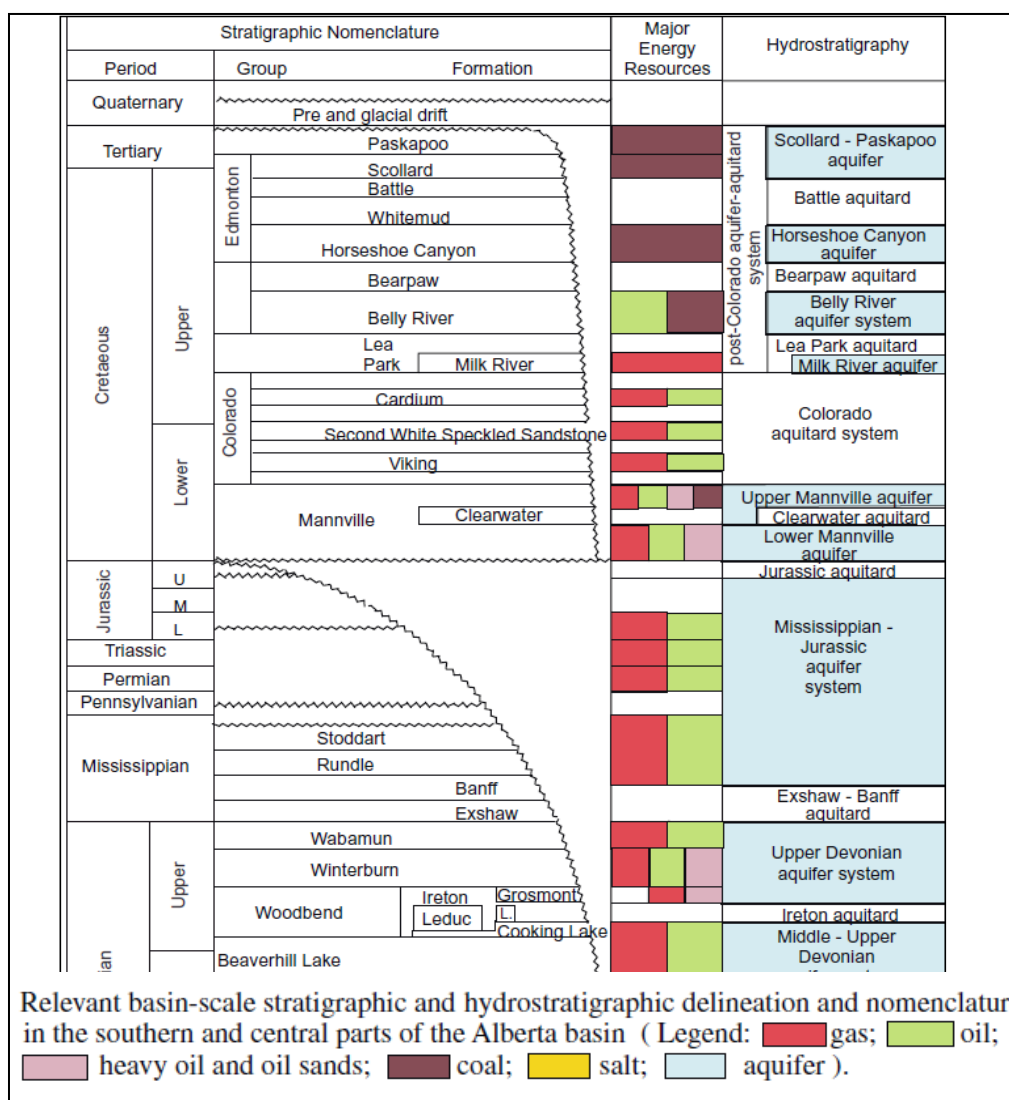
Figure 1-4: Stratigraphic sequence of the southern Alberta basin, including hydrological and fluid information (Modified from Bachu et al., 2000).

1.4.4 Structural Characteristics

As mentioned previously, the Alberta basin is located on the eastern flank of the Rocky Mountains and it represents a very stable tectonic area with "layer cake" deposits (Bachu et al., 2000). In the Rocky Mountains Foothills, from north to south there is a transition from a fold-dominated to a thrust-dominated structural styles and deformation of the sediments. Figure 1-5 shows the structural features going from the basement to Tertiary deposits. From the Upper Devonian detachment, narrow folds were formed passing to a Middle Devonian-Cambrian thrust faulted subsection (Wright et al., 2008). Between the Lower Cretaceous and Jurassic strata there is a detachment, generating a geological style dominated by faulted folds and duplexes, but above the Mississippian rocks the structures are less complex. In the eastern foothills, the Upper Cretaceous and overlying deposits often exhibit fault-bend folding. The Tertiary deposits present little deformation. They are composed of dipping layers that outcrop in the nearby area of the Rocky Mountains Foothills (Wright et al., 2008).
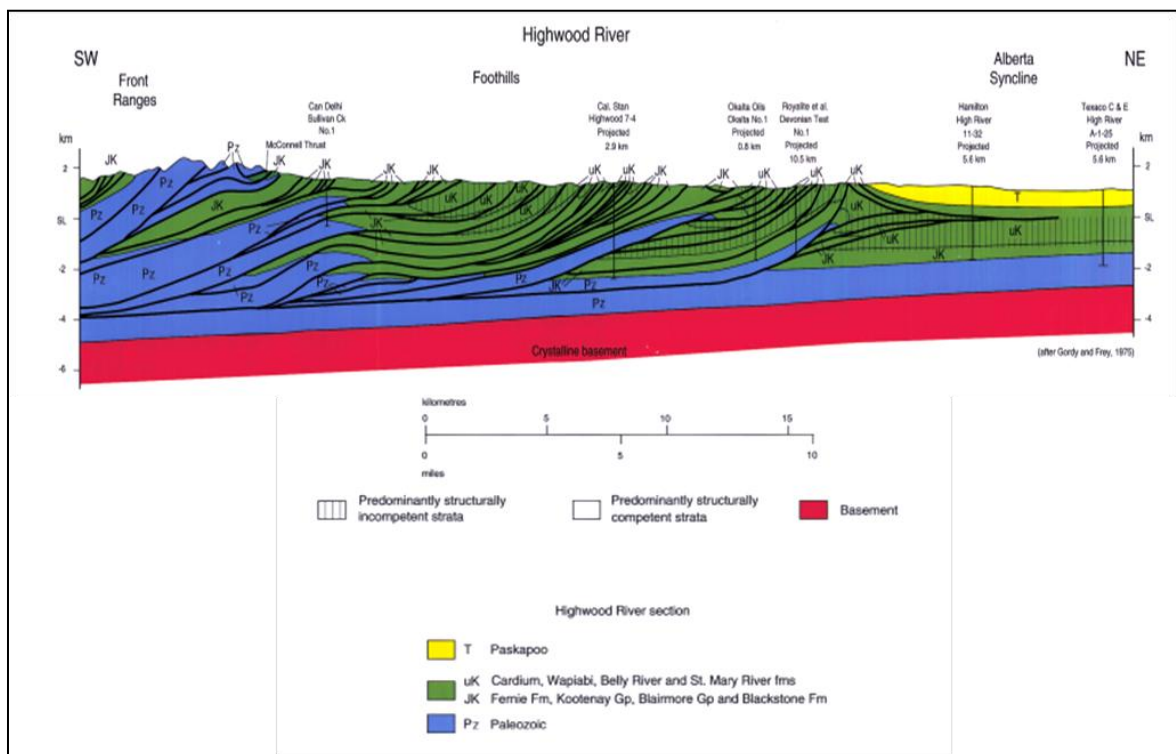
Figure 1-5: Cross-section with the structural style of the southern Rockies. The area is Highwood River and it shows a thrust dominated zone. The changes of colors are related with the age of the sediments (Wright et al., 2008).

1.5 Thesis Objectives

The main goal of this thesis is to evaluate the feasibility of monitoring a volume of CO_2 injected in a geological storage formation using the seismic method. The site chosen was a shallow sandstone aquifer of Paskapoo Formation. Three specific objectives were identified to achieve this goal. The first was the application of fluid substitution using a Gassman approach in order to evaluate the changes in the Formation properties given different CO_2 saturations. Prior to this calculation it was necessary to evaluate the physical properties of the formation such as density, velocity and porosity. These values were obtained from well log information.

Once the petrophysical changes due fluid substitution were obtained, the second objective was the generation of geological models simulating the area of study at different scales. Two geological models were created: an 8 km long 2D model and a 2.5x1 km 3D model. These models were based in seismic surveys obtained in the area and well log information. In addition, a simplified simulation of the CO_2 plume was estimated and included in the geological model as a new body.

The third objective was to undertake seismic modelling over the 2D and 3D geological models, before and after CO_2 injection, to evaluate the efficacy of time-lapse seismic surveys to monitor the injected CO_2 plume. In conclusion, evidence of measurable changes in seismic patterns were found such as reflectivity and time shift, from the injection of CO_2 in the modelled target that simulated Basal Paskapoo Sandstone.

1.6 Thesis Outline

Chapter 2 shows the two seismic surveys that were recently acquired in the area in order to characterize the possible injection zone. The first survey was a 3D volume acquired during May 2010 and the second was a 2D line acquired in August 2010. This section goes through the design of the survey, acquisition parameters, processing flow and interpretation.

Chapter 3 discuss the petrophysical and fluid substitution process applied over the formation of interest in order to define changes in properties after CO_2 injection. The

calculations were based on a Gassmmann approach and attempt to reproduce how physical properties such as density and bulk modulus will change after injection of CO_2 into the Paskapoo Fm.

Chapter 4 explains the generation of the 2D geological model and the estimated CO_2 plume. It covers the modelling and design of the structural and stratigraphic scenario and further addition of an estimated CO_2 plume. It goes over the raytracing, processing and analysis of seismic sections.

Chapter 5 follow the same principles described in Chapter 4 but for a 3D model. This includes a set of extra variables in order to design the geological model and the CO_2 plume.

Chapter 6 discusses the results and conclusions obtained from this research project.

1.7 Software

Several software packages were used in the development of this thesis:

- Hampson Russell Software: eLog and Pro4D
- Norsar 2D and Norsar 3D
- Promax
- Vista
- Kingdom Suite
- Microsoft Office

Chapter Two: : Regional Geological Model

2.1 Introduction

The main objective of this chapter is to create a baseline geological model, using as guide, seismic data in the area. It is necessary to define the regional geological structure and stratigraphy that involves the target formation, in this case Paskapoo Formation. The stratigraphic and structural background explained in Chapter 1 is complemented by the analysis of seismic data in the area. Through the seismic interpretation it was possible to define the position and structure of the main formations, as well some regional trends that validate further geological modelling. This chapter discusses all the methodologies applied to the seismic data: acquisition, processing but more important its interpretation, in order to create a detailed geological model of the area.

2.2 Seismic in the area

Several 2D and 3D surveys have been acquired in the Priddis area over the last four years. The University of Calgary owns a portion of land next to the Rothney Astrophysical Observatory, where CREWES has undertaken seismic acquisition and vertical seismic profile projects. The initial surveys acquired were a 3D volume in 2007 and a 2D line in 2009. This data helped with the trials of new seismic technology and most important, gave a good understanding of the structural scenario of the site.

With the financial help of Carbon Management Canada and ISEEE, CREWES undertook a 2010 seismic acquisition campaign in order to perform a more detailed study directed to characterize the area for monitoring CO_2 injection. A 3D survey was acquired in May, 2010 and a 2D line was acquired in August, 2010. Both were obtained using University of Calgary equipment and the labour of staff, professors and students. The 3D survey was located in the area of possible injection and the 2D survey was a regional east-west line.

Figure 2-1 is a digital elevation map, which shows the structural changes from east to west in the area of study. It is possible to see the Paskapoo sandstone ridge

outcropping. In addition, it shows the location of the two 2010 seismic surveys, the 2D line and the 3D volume. This chapter discusses the survey design, acquisition parameters, data processing and interpretation.
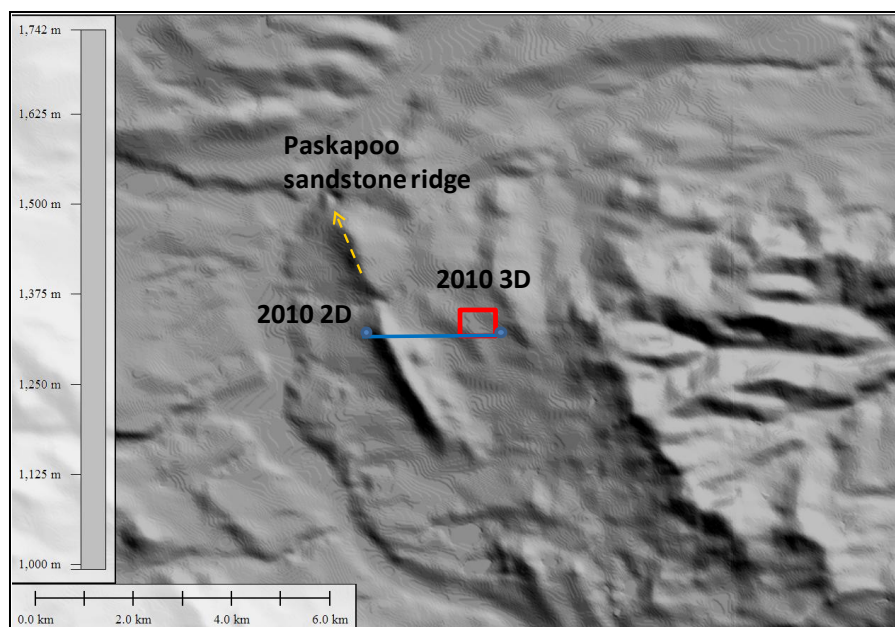
Figure 2-1: Digital elevation map with the location of the seismic surveys in the area, 3D (red square) and 2010 2D (blue line). It includes the position of the Paskapoo sandstone ridge (Map courtesy of Geological Survey of Canada, modified by Isaac and Lawton, 2010a).

2.3 2D Seismic Survey (August, 2010)

2.3.1 Survey Design and Acquisition

A 3C-2D seismic line was recorded, during the August 2010 University of Calgary geophysics field school. The line has an east-west trend from the south of the University of Calgary land at the Rothney Astrophysical Observatory towards Priddis Valley Road (Bertram et al., 2010). The line was 2500 m in length with 10 m spacing between geophones and shots at every station (Bertram et al., 2010). A total of 628 usable shots were acquired with a maximum of 488 channels per shot, with a spread of 588 3C geophones and farthest offset of 2400 m (Isaac and Lawton, 2010b). Figure 2-2 represents the CDP fold along the 2D line, showing a maximum of 350 in the center of the line with an average of 100 (Isaac and Lawton, 2010b).

The equipment specifications were: SM7 three-component geophones, 24 channel RAM units, both from ARAM Rental Corporation, SPMLite recorder and EnviroVibe source from University of Calgary. A sample shot is shown in Figure 2-3; in which it is possible to see visible reflections up to 2500 ms (Bertram et al., 2010).
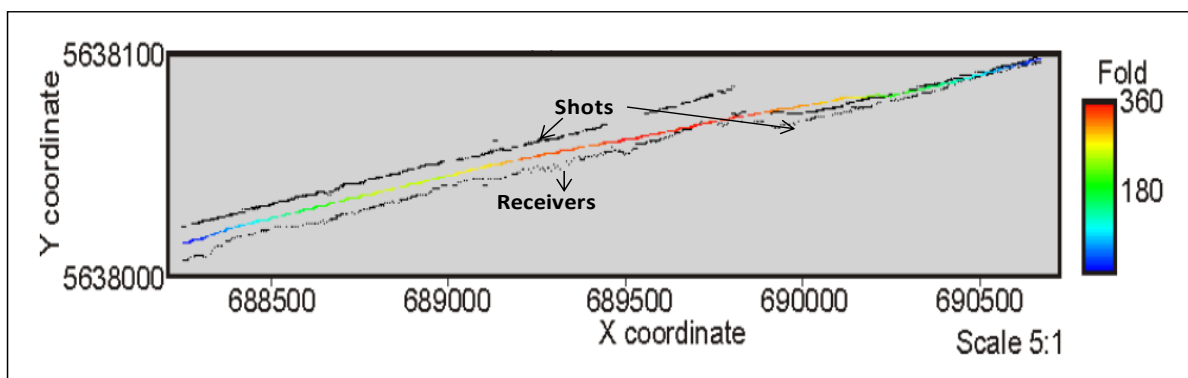
Figure 2-2: 2D line CDP fold map (color line). Include the shot and receivers position (black dots) (Modified from Isaac and Lawton, 2010b).
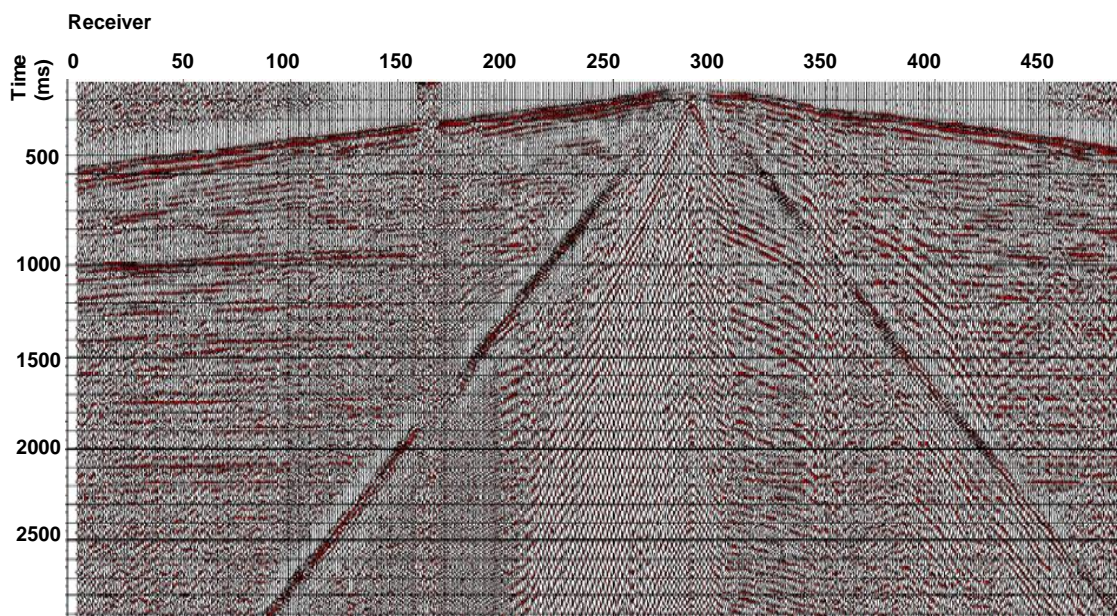
Figure 2-3: Sample shot from the 3C 2D seismic acquisition (Bertram et al., 2010).

2.3.2 Data Processing

The data processing was performed by Helen Isaac using Promax software, via a basic processing flow illustrated in Table 2-1. The goal of this processing was to properly image shallow reflectors, especially Paskapoo Formation (Isaac and Lawton, 2010b). Figure 2-4 is the processed seismic section and it is possible to see high amplitude deep reflectors and shallow reflectors dipping towards the east.

Table 2-1: Processing flow. Taken from Isaac and Lawton, 2010

Standard Flow
2D geometry assignment and binning
Elevation and refraction statics
Geometric spreading compensation; surface consistent amplitude scaling
Surface wave noise attenuation; air blast attenuation; spike ad noise removal
Predictive decovolution
Q-compensation
Gabor deconvolution
Bandpass filter 5-10-90-100 Hz
Velocity analysis
Residual statics
Post stack time migration
Pre stack time migration
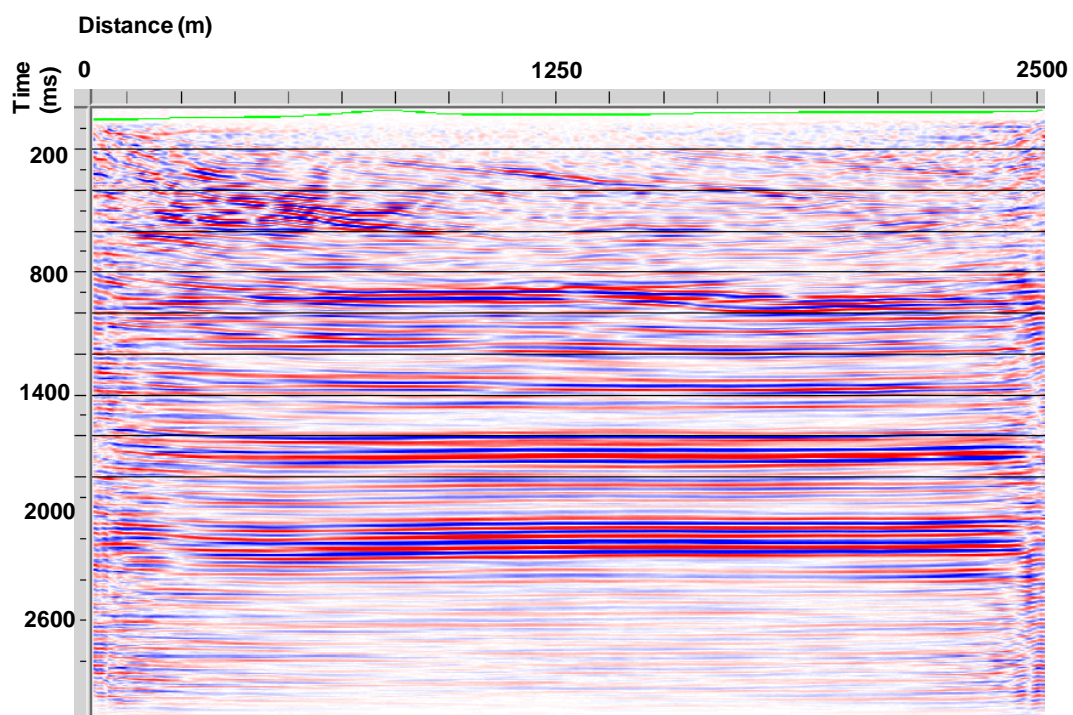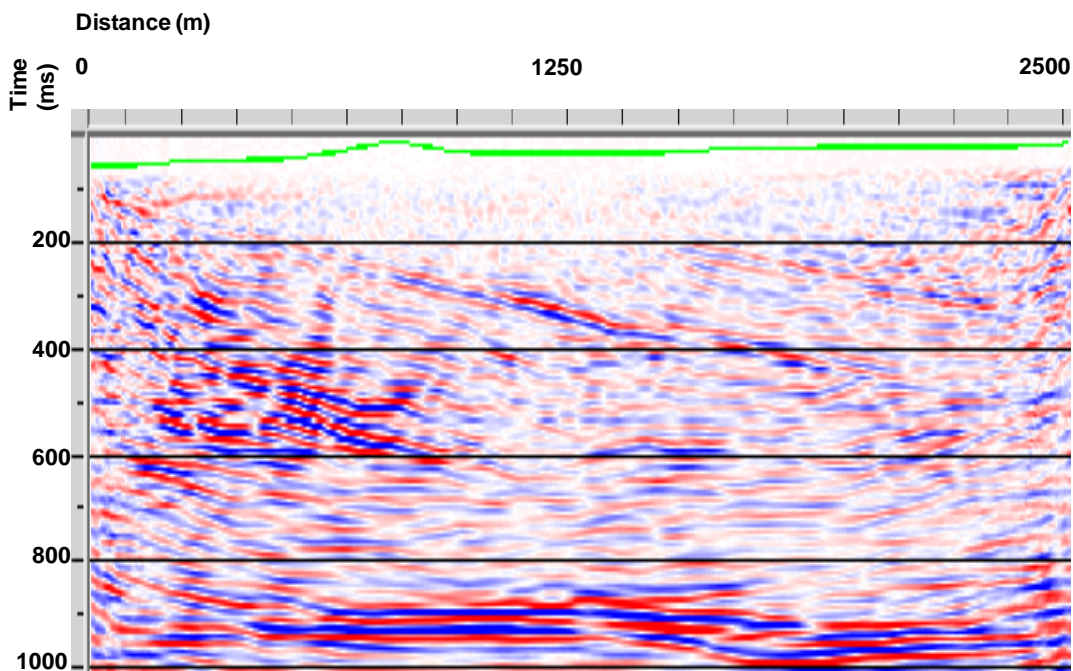
Figure 2-4: a) CDP stack section and resulting processed 3C 2D line. b) Detail of the first 1000 ms showing the shallow dipping layers (Bertram et al., 2010).

2.4 3D Seismic Survey (May, 2010)

2.4.1 Survey Design and Aqcuisition

The 3D seismic survey was acquired by CREWES during May 2010 at the Rothney Astrophysical Observatory (RAO) site. The objective of this survey was to map and characterize an area for possible CO_2 injection. The survey was composed of: seven receiver lines with east-west direction and fifteen shot lines with north-south direction. The spacing between lines, both shot and receiver, was 50 m, with shot points and geophones at every 10 m. These parameters were selected with the goal of producing high quality images of the shallow stratigraphy (Isaac and Lawton, 2010b). Figure 2-5 shows the X and Y coordinates of receiver and source location. The CDP bins are 5x5 m with an average fold of 60. The final CDP fold map is shown in Figure 2-6, yielding a maximum fold of 110 in the center of the survey.
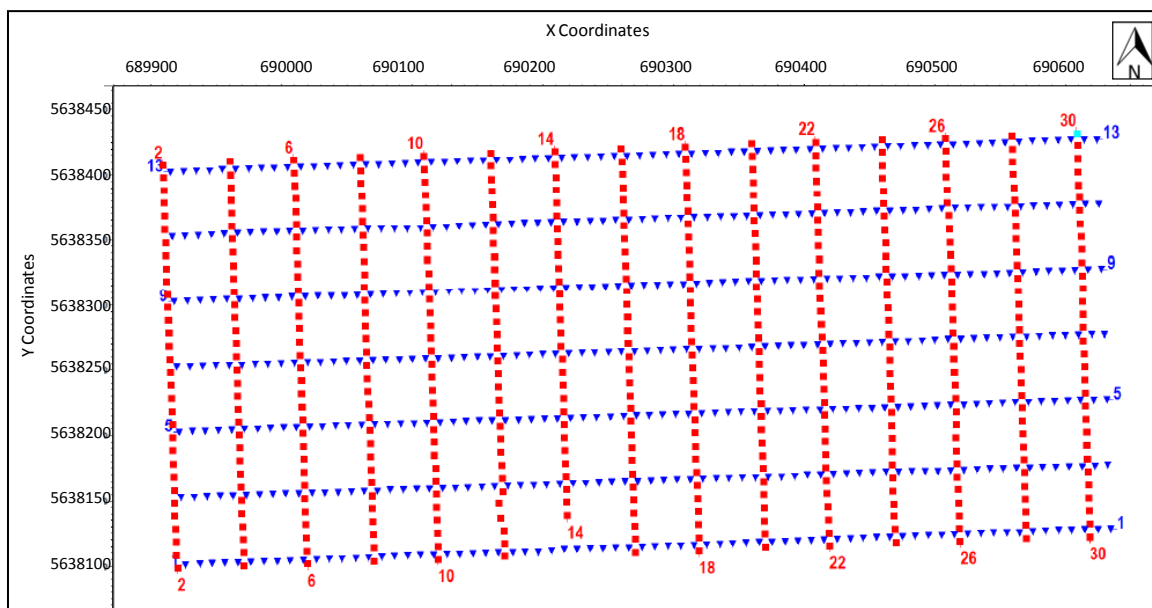
Figure 2-5: 3D survey positioning, X and Y coordinates. The receiver lines (blue) have an east-west direction and shot lines (red) have a north-south direction.
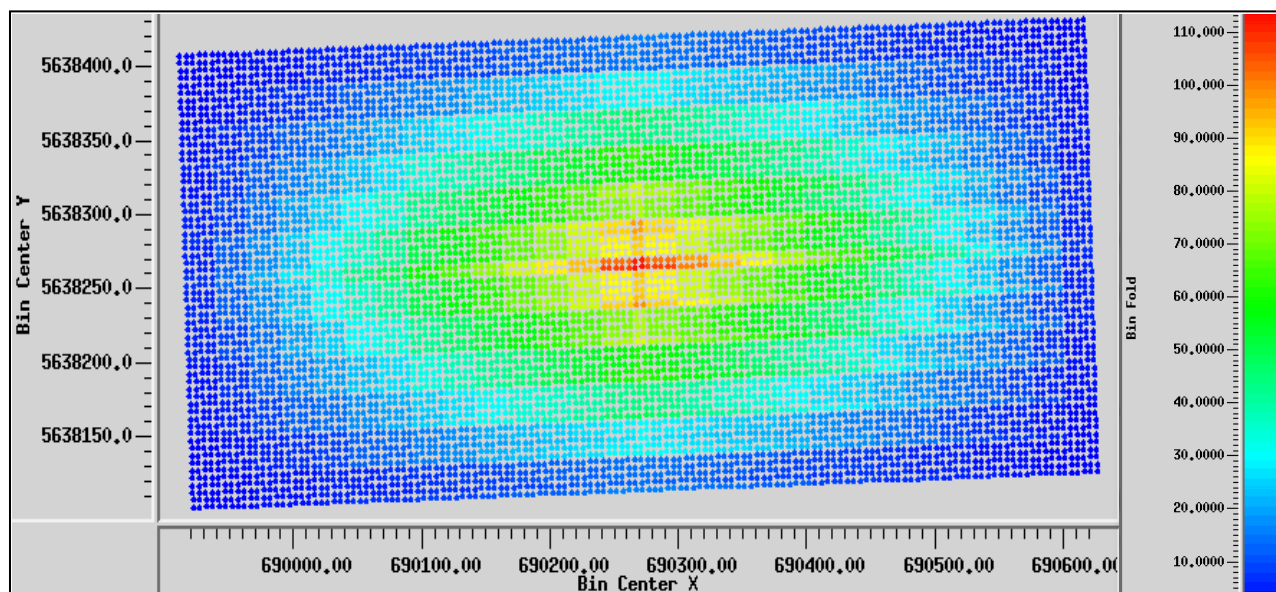
Figure 2-6: CDP fold in the Bin center X and Y plan. The higher fold values are located in the center of the survey (red), with lower values towards the edges (blue).

Given that the data was acquired during spring, the conditions were very favourable with dry soil and good weather conditions. The shot points and receivers were located using a RTK GPS, real time kinematic global positioning system (Hall et al., 2010). The equipment was composed of: 72 3C Sensors SM7 geophones in each receiver line and 24 channel RAM`s, both provided by ARAM Rental Corporation; the EnviroVibe source and SPMLite Aries recording system were provided by University of Calgary (Bertram et al., 2010). The vibe recorded with a sweep of 10 to 200Hz over 20 seconds with 4 sweeps per vibe point (Bertram et al., 2010).

2.4.2 Data Processing

The data processing was performed using Promax software with the guidance of Helen Isaac and Dave Henley. The shot gathers obtained from the acquisition were of very good quality and clear reflectors are observed. Figure 2-7 shows the shot gather from source number 74. Some reflections and ground roll noise can be appreciated. A conventional 3D processing flow was developed and it is summarized in Table 2-2.
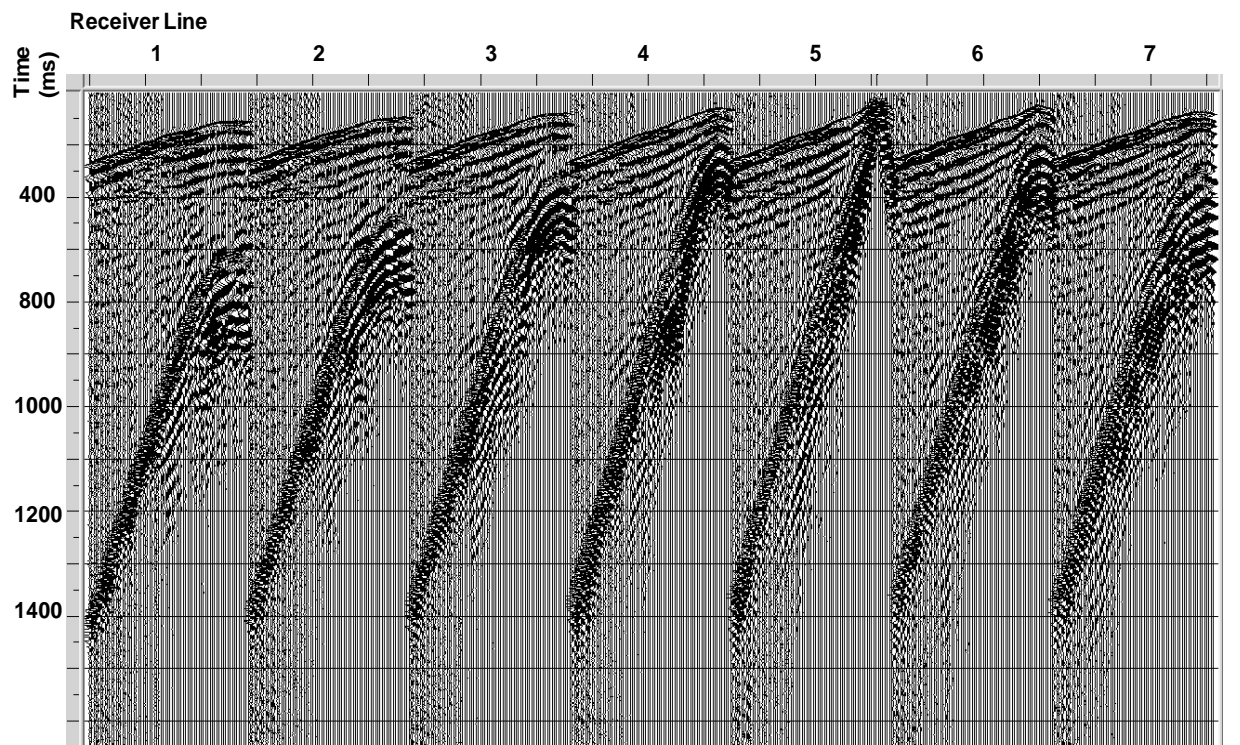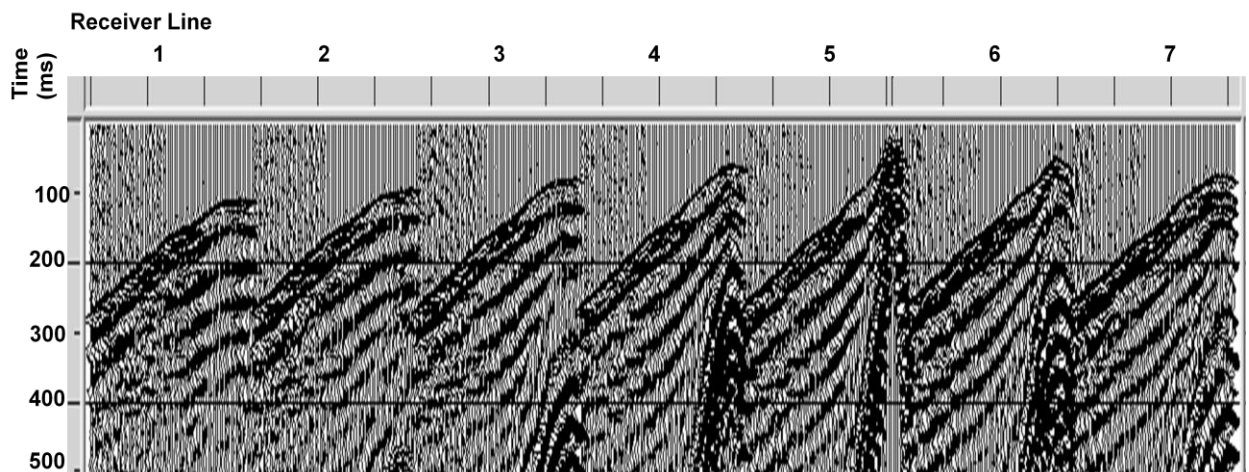
Figure 2-7: Example of a raw shot gather (a), showing strong airwave and surface wave energy, especially in the first 500 ms (b).

Table 2-2: Processing flow applied to the 2010 3D seismic data.

Standard Flow
3D geometry assignment and binning
First break picking
Elevation and statics correction
Surface wave noise attenuation; air blast attenuation; true amplitude recovery
Radial Filter
Gabor decovolution
Bandpass filter 5-10-90-100 Hz
Velocity analysis
CDP stack
Kirchhoff post stack time migration

2.4.2.1 Geometry set up:

A fundamental step before starting any data processing is to assign the right geometry distribution in order to get the data properly sorted and processed (Isaac, 2008). In this case the data imported was field data from the survey, which has in the header the field file identification number (FFID) and the channel number. The spacing of the receivers and sources is 10 m with a common midpoint of 5 m.

2.4.2.2 First break picking:

It is the first procedure to apply before any filtering (Isaac, 2008). In Promax it is possible to make use of the tool "First Break Picking", where specifying a time offset dependent window, the program selects the first breaks inside that range, picking the zero-crossing break (Figure 2-8). Generally it is very precise, except for far offsets, where data becomes noisy.
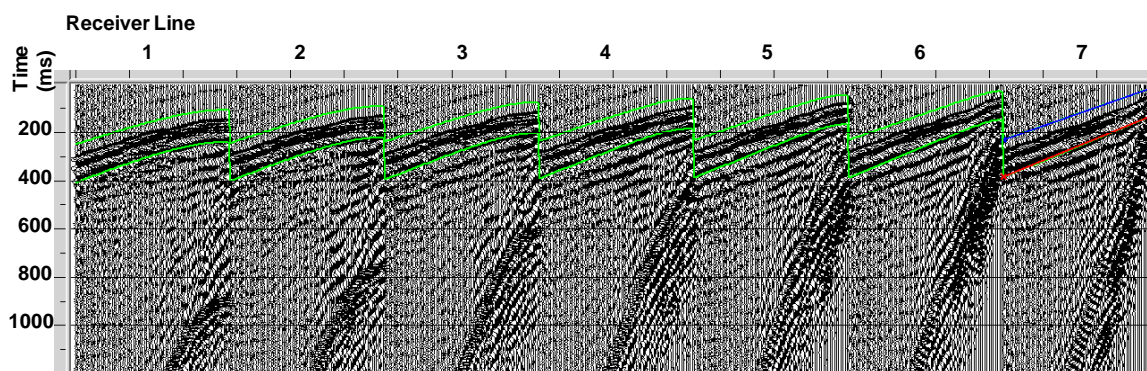
Figure 2-8: First break time window. The receiver line number 7 presents the time window selected in blue and red. The rest of the lines present the auto-selected window in green.

2.4.2.3 Elevation and Statics Correction:

In order to calculate refraction statics caused by shallow layers of weathering, the Hampson-Russell's GLI3D module was used. This tool generated a near surface model taking the first break picks previously made. The model generated in GLI3D was imported into Promax using "Apply Elevation Statics" and correct source and receivers to the new elevation datum (Isaac, 2008). The datum selected is crucial for applying velocity analysis and CDP stacks, because it will be used as a reference. In this case, the selected datum was 1260 m. An example receiver line from one shot is in Figure 2-9 after the application of static corrections.
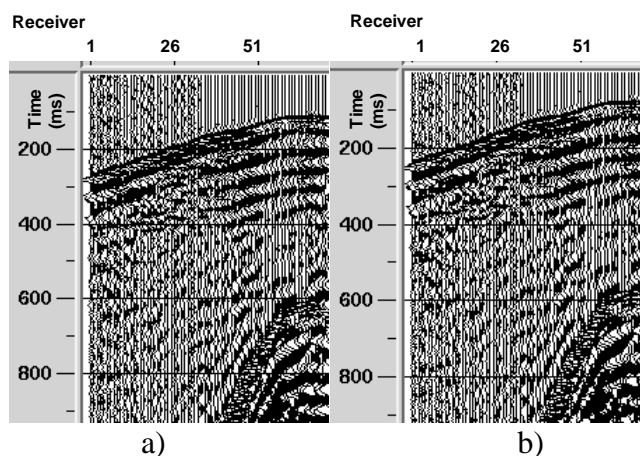
Figure 2-9: Shot gather (line number 1 and source number 60), before (a) and after (b) static corrections.

2.4.2.4 Noise attenuation

By examining to the shot gathers in Figure 2-7 it is easy to appreciate the presence of noise dominating true reflection events. This noise can be shot-generated (surface waves), externally generated (power line interference) or receiver generated (bad coupling, noise bursts) (Isaac, 2008). There are several noise attenuation tools and one of the most popular was the F-K filter. However, a relative new technique, the Radial Trace Filter, has started to gain popularity. Its goal is to reduce linear noise and recover true reflectivity events. This concept was proposed by Claerbout (1975) and developed in CREWES by Henley (1999). This technique attempts to isolate the coherent noise or ground-roll from the reflection signal by selecting a value or range of velocity traces in the R-T domain (Henley, 2003). The events aligned with this parameter will be transformed into a low-frequency signal and then subtracted in the x-t domain (Henley, 2003). Typically, reflections have higher velocities while ground-roll has much lower velocity, therefore the high velocity events should remain unaffected by this filter. This process is associated to a mute or a low-cut filter to diminish the noise low frequency signal in the x-t domain (Henley, 2003). R-T filter presents two possible configurations, fan filter and dip filter (Henley, 2003). The first one allows the attenuation of a range of noises at different velocities but generated by a single source (Henley, 2003). The second filter attenuates the nearly parallel coherent noise with a common apparent velocity but different source (Henley, 2003).

In the processing flow of the 3D Priddis survey, a succession of R-T filters was applied. First a fan filter (from -4000 m/s to 4000 m/s) and second, three dip filters (150, 260 and 330 m/s) were applied. All the filters presented different velocity dips but the same low-cut filter (8-15 Hz.). In Figure 2-10, the reduction of the coherent noise and improvement in reflection quality is evident. The final image is the result of a band pass Ormsby filter 8-12-65-85 Hz. It is important to note that before the application of the R-T filters a series of conventional noise attenuation tools were applied, including: true amplitude recovery, air blast attenuation (attenuated velocity = 330 m/s with a filter of 35-50-90-12 Hz.) and surface wave attenuation (noise velocity = 400 m/s, low frequency of 0 Hz., high frequency of 30 Hz. and a blend width of 5 Hz.).
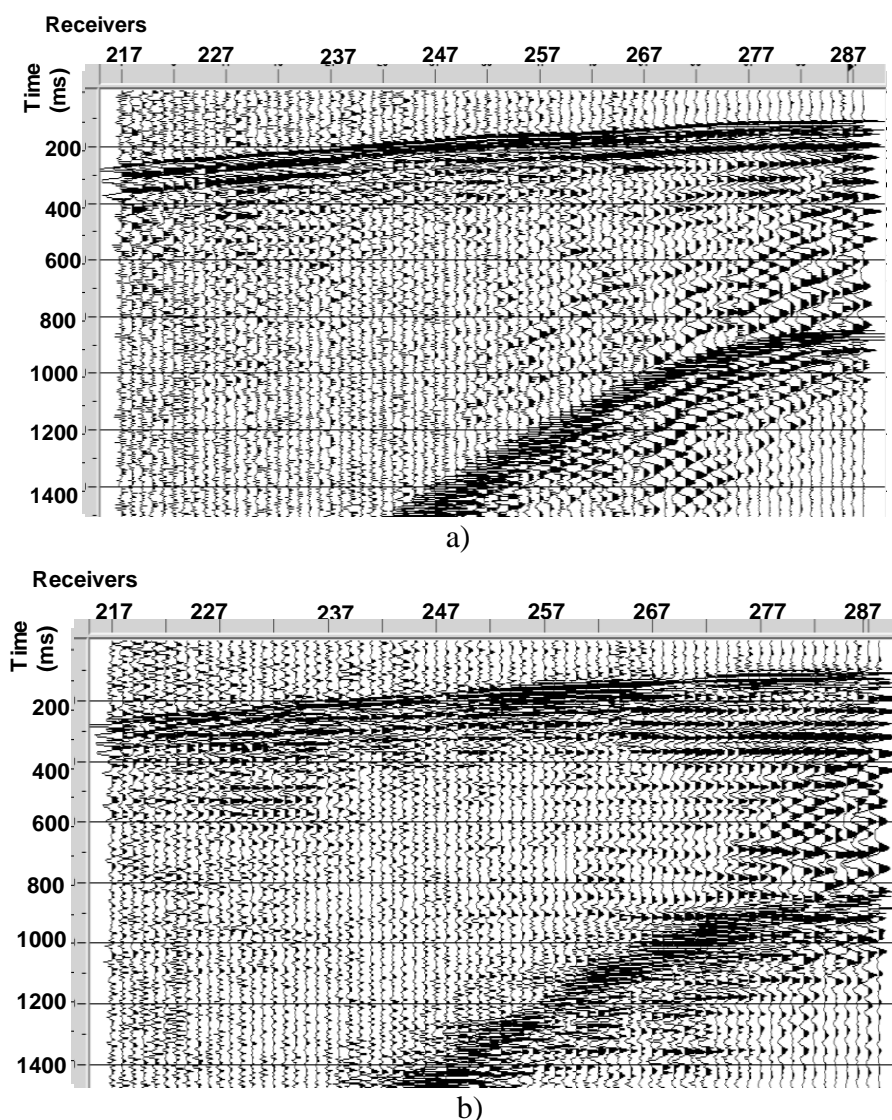
Figure 2-10: Sample shot: a) original data, b) result of applying successions of radial filters and final band pass (8-12-65-85 Hz).

2.4.2.5 Deconvolution:

This step is fundamental in the processing flow and it is based on the principle of removing the seismic wavelet from the seismic trace by applying an inverse filter (Isaac, 2008). The resulting data should have fewer multiples and have a more balanced spectrum (Isaac, 2008). The most common deconvolution methods are spiking and predictive. However, these two methods assume that the wavelet is invariant with time which means it is stationary, not taking into account the effects of attenuation, frequency

shaping and amplitude variation (Henley and Margrave, 2008). Margrave et al. (2004) proposed the use of a nonstationary deconvolution technique capable of removing the source signature and the earth attenuation effects. This method is the Gabor deconvolution which is an extension of the Wiener filter, based on the estimation of the time and frequency variant Q function or attenuation function. This function is calculated for each seismic trace using the Gabor Transform and then it is included in the deconvolution operator to remove the attenuation effect of Q (Henley and Margrave, 2008). Gabor deconvolution also boosts high frequency noise; therefore it is necessary to apply a high-cut filter during later processing. Figure 2-11 shows an example receiver line after applying Gabor Deconvolution.

a)

b)
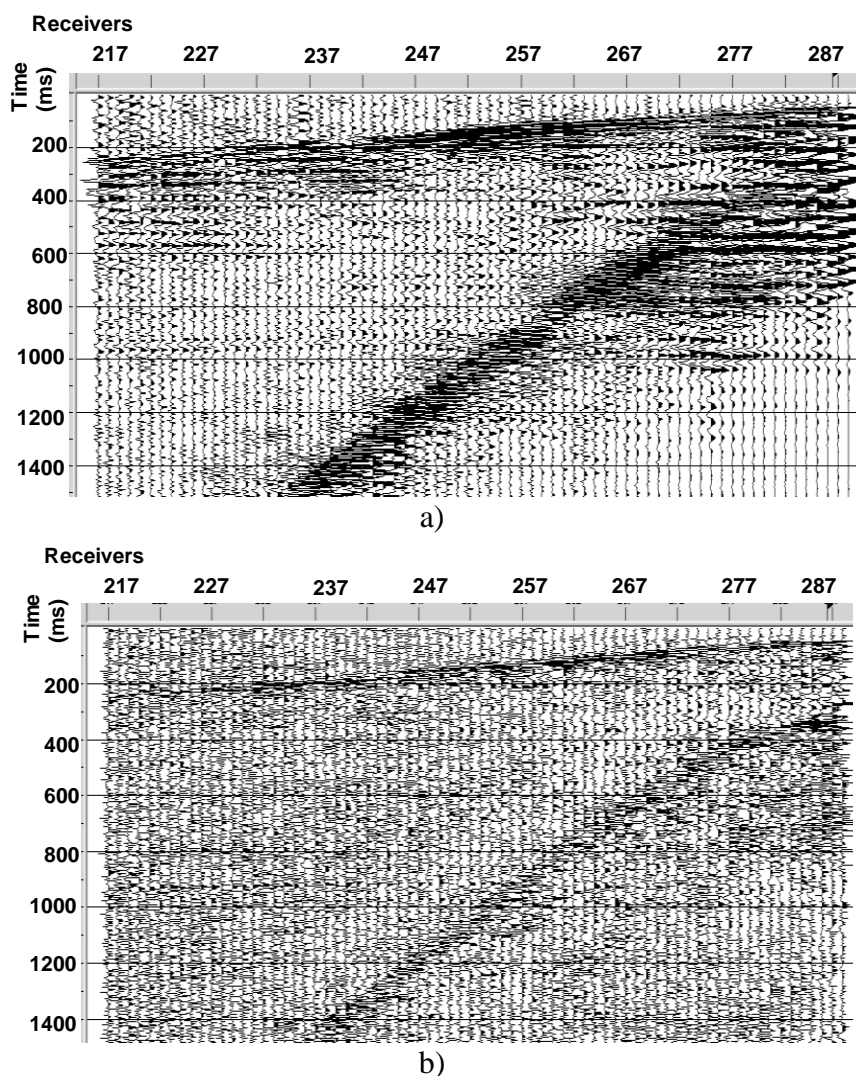
Figure 2-11: Sample line before (a) and after (b) applying Gabor Deconvolution.

2.4.2.6 Velocity analysis

Once the deconvolution was performed, it was necessary to obtain a velocity model to correct for Normal Move Out (NMO) process. NMO correction is the time displacement of the reflection events in order to make all the traces zero-offset. This process is based on the hyperbolic relationship

$$t^2 = {t_o}^2 + x^2/v_{RMS}^2 \tag{2.1}$$

where t is the recorded time at offset x , t_o is time at zero offset and V_{RMS} is the root mean squared velocity. The NMO correction is given by the difference between $t - t_o$ and it can be reduced to:

$$\Delta t_{RMS} = t - t_o = \sqrt{{t_o}^2 + x^2/v_{RMS}^2} - t_o \cong x^2/2\, v_{RMS}^2 t_0 \tag{2.2}$$

This approximation is applicable for $x << V_{RMS}t_o$. The RMS velocity was obtained using semblance analysis. This technique is based on the picking of a velocity function from CDP interval by interval through the 3D volume. The selected interval in this case was 25 CDPs. Figure 2-12 shows an example of the velocity analysis display at CDP 2912. The first panel is the semblance which displays a calculation made by the program, where it measures the amplitude of the stacked panels and creates a contour semblance plot (Isaac, 2008). The semblance is calculated through the formula:

$$semblance = \frac{1}{m} \frac{\sum_t (\sum_{i=1}^{m} f_{i,t(i)})^{\,2}}{\sum_t (\sum_{i=1}^{m} f^2{}_{i,t(i)})} \tag{2.3}$$

where m is the number of stacked traces, t is the time window of the trace sum and f is the trace amplitude. The high semblance values are presented in red colors in the contour map and they are related to the most effective velocity values in the NMO process. The black lines show the input velocity trends. Next to this is the gather showing the section in time against offset, followed by its stacked version. The final panel is the stacked version created after applying move out with the different velocity functions. The picking of the velocities is related to the selection of the highest semblance and best NMO stack in the velocity function panels. The final pick is given by the white line on the semblance panel and the red line on the NMO panel.

From the calculated velocity function, a 3D velocity model was obtained and this result should be representative of the geology. Figure 2-13 illustrates an inline and

crossline view of the 3D velocity model, resulting from the velocity picks. As expected, the model reflects the general geological scenario of flat layers in the crossline direction and dipping layers towards the west.
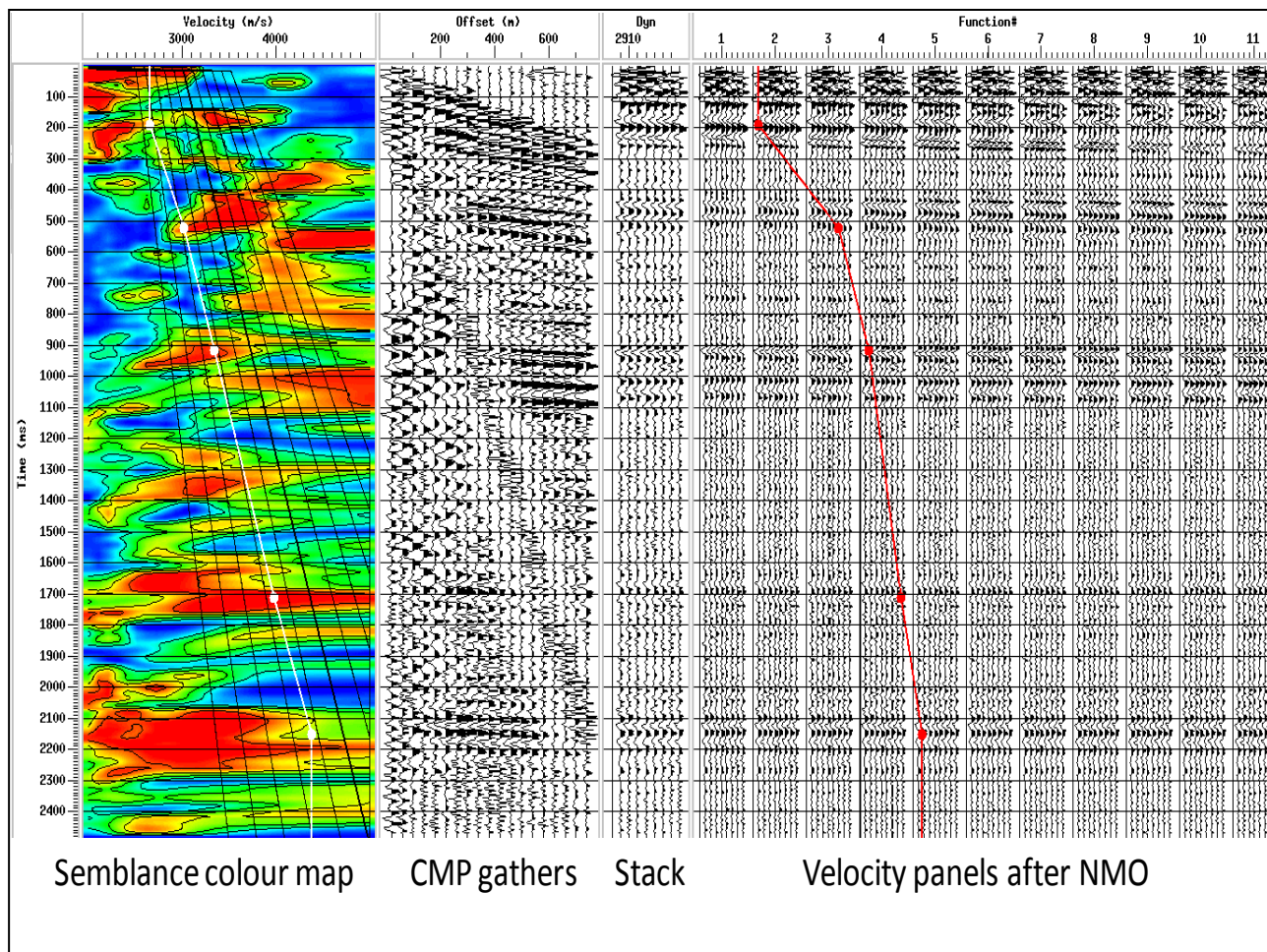
Figure 2-12: Velocity analysis with semblance, velocity panels for NMO analysis. The final velocity picks are shown by the white line over the semblance panel and the red line over the stacked seismic panels.
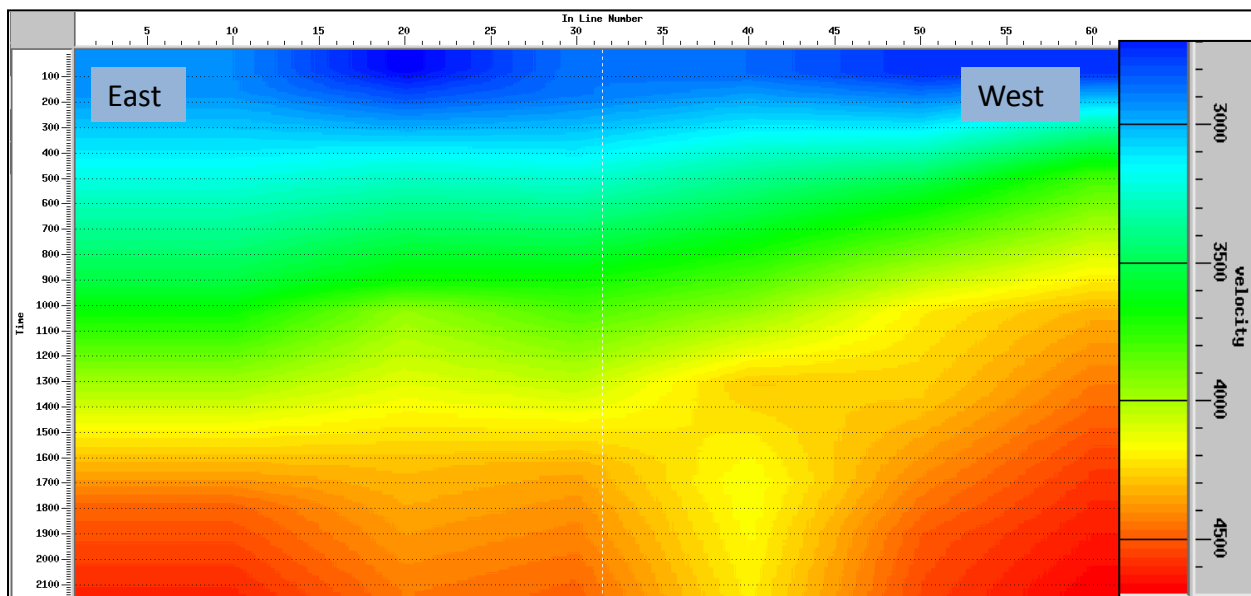
a)
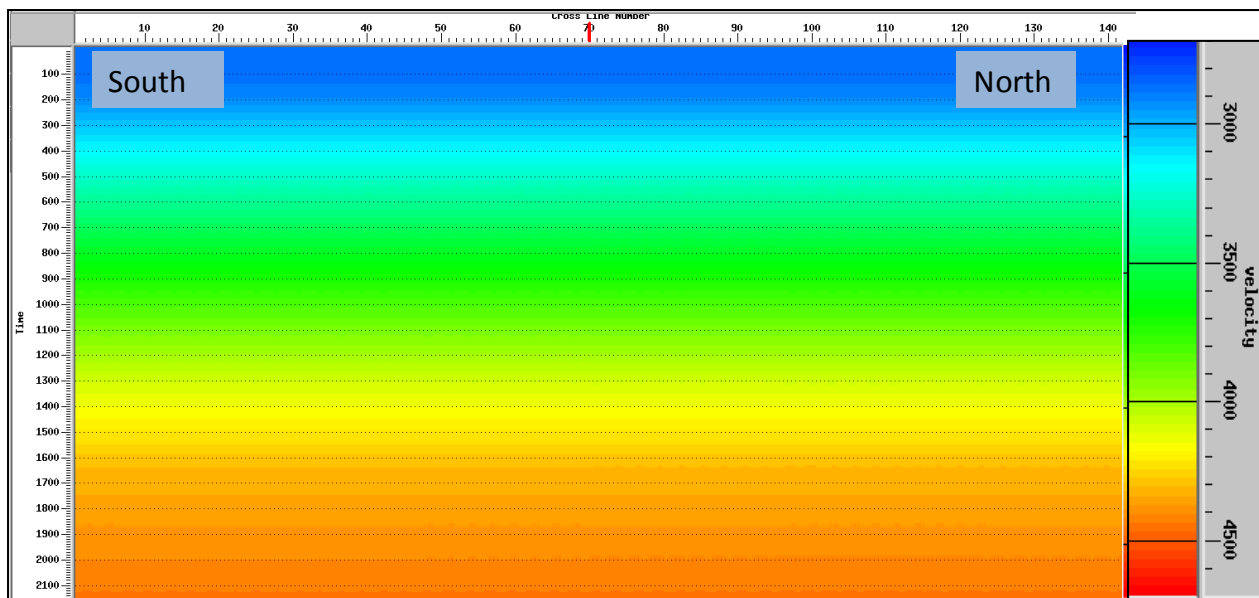
b)

Figure 2-13: Velocity model obtained from velocity picking. (a) is an inline view (east-west) and the (b) is the cross line view (south-north).

2.4.2.7 Common Depth Point Stack

The Common Depth Point (CDP) method attempts to transform the hyperbolic reflection events into a pseudo cross-sectional image that reflects the geological layering (Schneider, 1984). In order to do the stack, the NMO correction was first applied using the obtained RMS velocity. Once all the traces are zero offset it is possible to stack them and create seismic sections. Figure 2-14 is an example of an inline stacked section. There are evident strong reflections and it is possible to identify dipping layers in the shallower part.
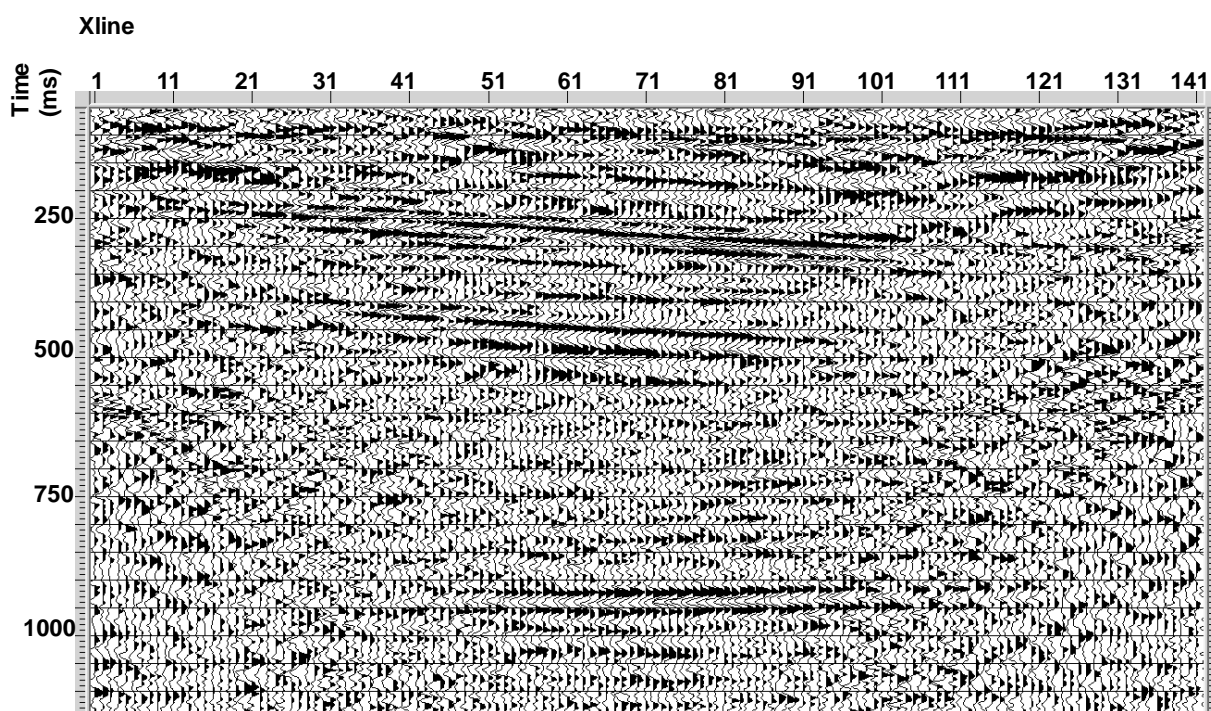
Figure 2-14: CDP stack section, in-line number 41. Flat and dipping reflections are evident in the central part of the line.

2.4.2.8 Post-stack time migration

Post-stack time migration attempts to relocate the reflections to their true subsurface positions. In this case Kirchhoff Migration was a technique applied and based on the summation of diffractions in order to migrate the data. For the Priddis survey a 3D post-stack Kirchhoff time migration was used. Examples of cross-line 54 and inline 41 migrated sections are presented in Figure 2-15. It is clear that the tendency is flat events

in the cross line direction, while the inline example show a slight dip (about 9 degrees) in the shallow reflectors (above 800 ms) and mostly flat for the deeper events.
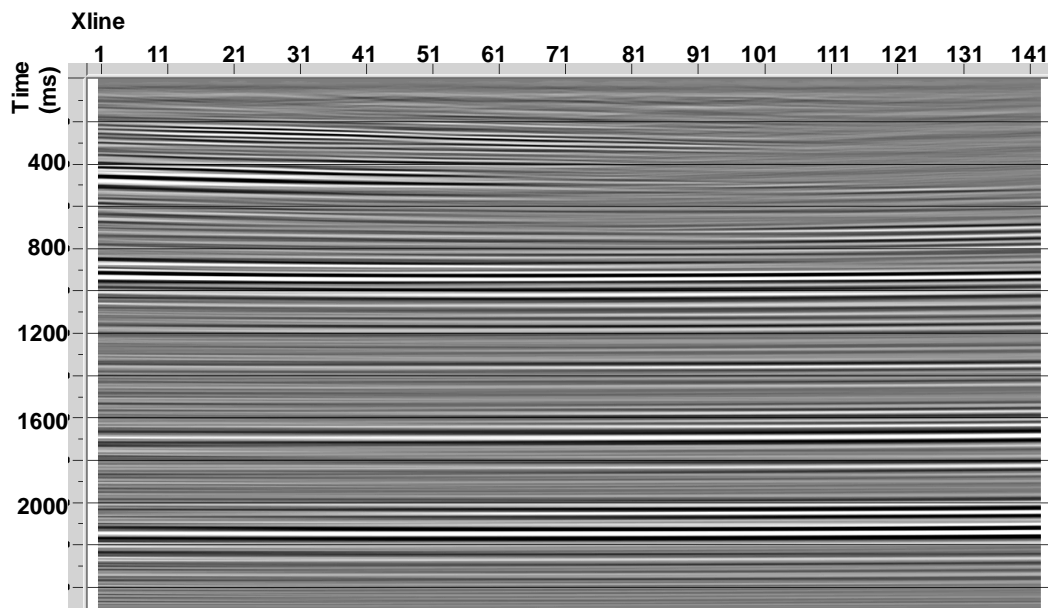
a)
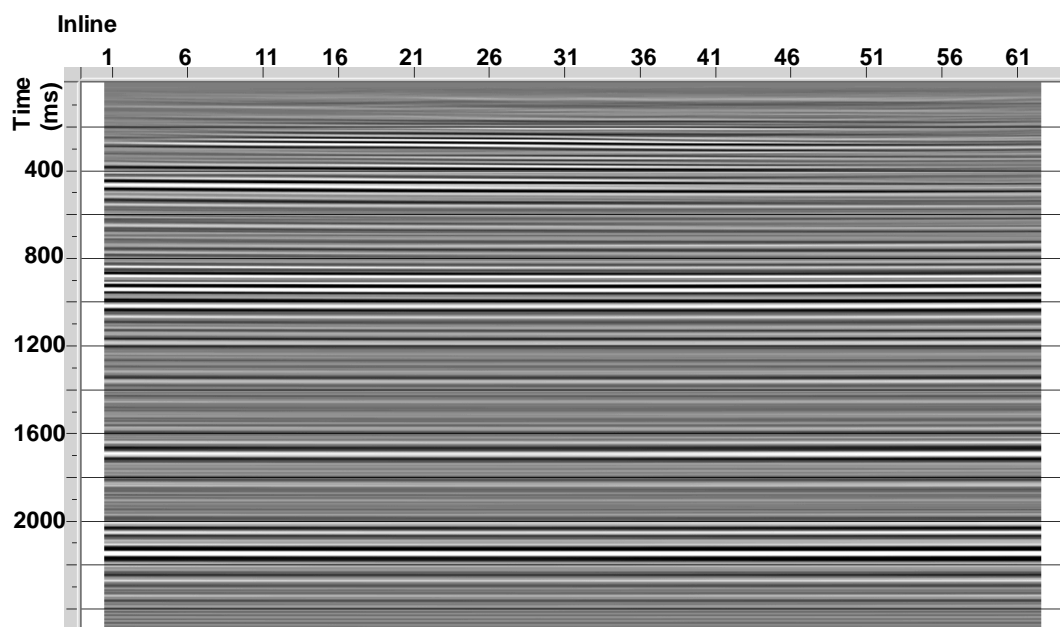
b)

Figure 2-15: Results after post-stack Kirchhoff time migration. (a) is an example of inline number 41 and (b) is the crossline number 54. The inline shows shallow dipping layers becoming flat later than 1000 msec. The crossline view shows flat reflectors.

2.5 Seismic Interpretation

The interpretation of the 3D volume was done by Helen Isaac using Kingdom Suite, having previous knowledge of the 2007 3D volume and 2009 2D line acquired in the area. Well 12-33-21-2W5 was used to identify the main horizons in the interpretation; this is the nearest well but is not within the seismic survey. It was extrapolated along strike making it possible to identify: the Middle Paskapoo A sand (MPA), Middle Paskapoo B sand (MPB), Lower Paskapoo sand (LP), Edmonton Group (E), Upper Detachment (UD), Lower Detachment (LD), Belly River (BR), Milk River (MR), Cardium (C) and Mississippian (M). UD and LD were approximately located given the imaging limitations (Isaac and Lawton, 2010a). In the case of the Paskapoo sand, it was assumed that the sandstone identified in the well logs extends regionally and it can be related to the strong dipping reflector in the seismic data (Isaac and Lawton, 2010a).

For the interpretation of the 2D line, the 3D results were used for identifying horizons. The 3D data has a 1260 m datum, which was used as reference for the correlation, and therefore a slight time shift was applied to the 2D survey (Isaac and Lawton, 2010). Figure 2-16 presents the 2D line with the synthetic seismogram tie and the correlation with the inline number 30 from the 3D survey. This synthetic was generated by extracting the wavelet from the 2D line. Another important result obtained by Isaac and Lawton (2010) it is presented in Figure 2-17, which is a depth cross-section along the profile of the 2010 2D seismic line. This section was created from depth grids generated from the seismic data interpretation using the average velocity for each of the horizons. For example for MPB, an average velocity of 3500 m/s was used for depth conversion. MPB, LP and E can be projected to the surface with a dip of approximately 35°. After the interpretation of the main horizons through the 3D survey, Isaac ad Lawton (2010), created a time-structure map for Lower Paskapoo Fm. confirming the expected trend of flat non dipping layers in the crosslines and a slight dip towards the plains. Figure 2-18 is the LP map with the scale in time and depth. The 3D survey covers what was expected to be the actual injection area; therefore it is expected to be repeated after the injection for time lapse monitoring purposes.
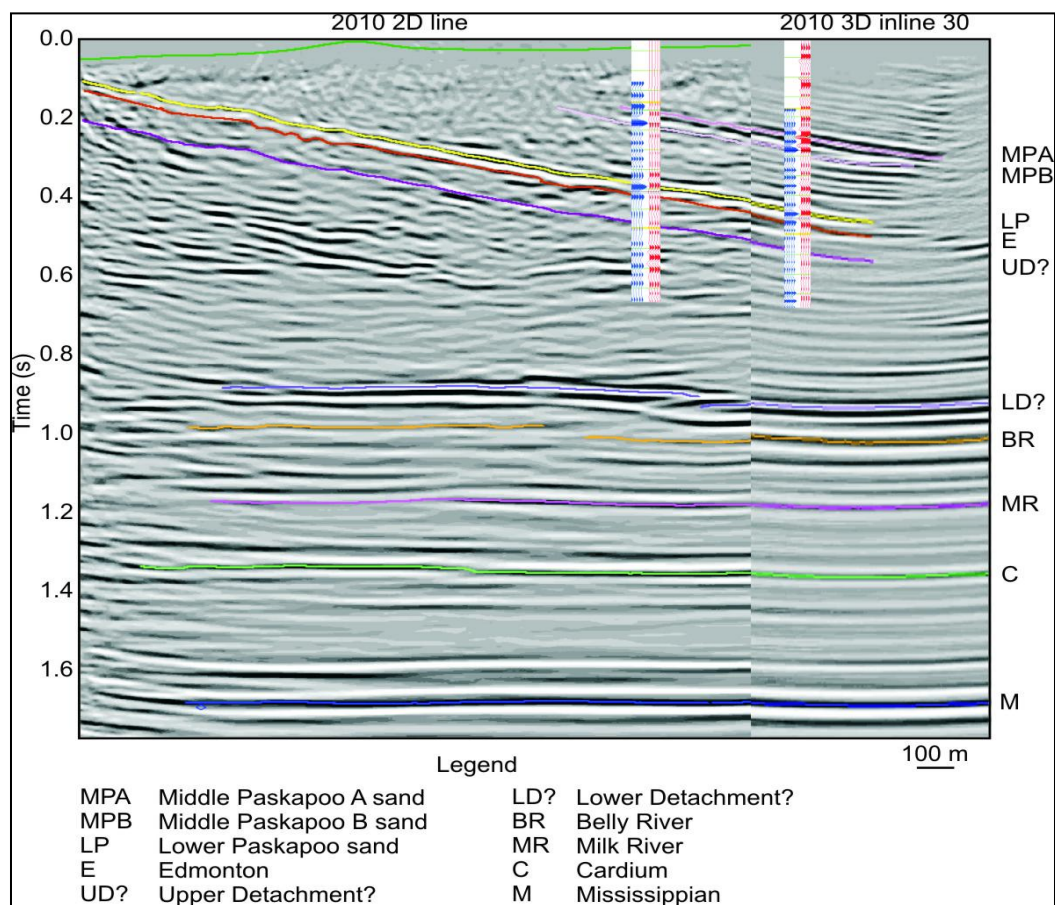
Figure 2-16: 2D line (left) correlated with the 3D survey and tie with the synthetics from well 12-33-21-2W5 (Isaac and Lawton, 2010a).
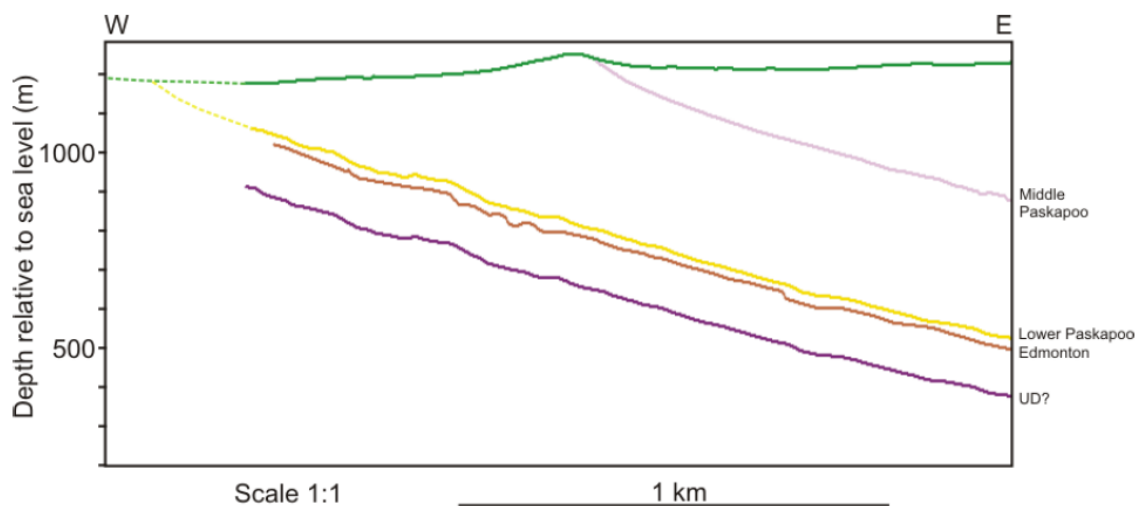
Figure 2-17: Depth cross-section along the profile of the 2010 2D seismic line (Isaac and Lawton, 2010a)
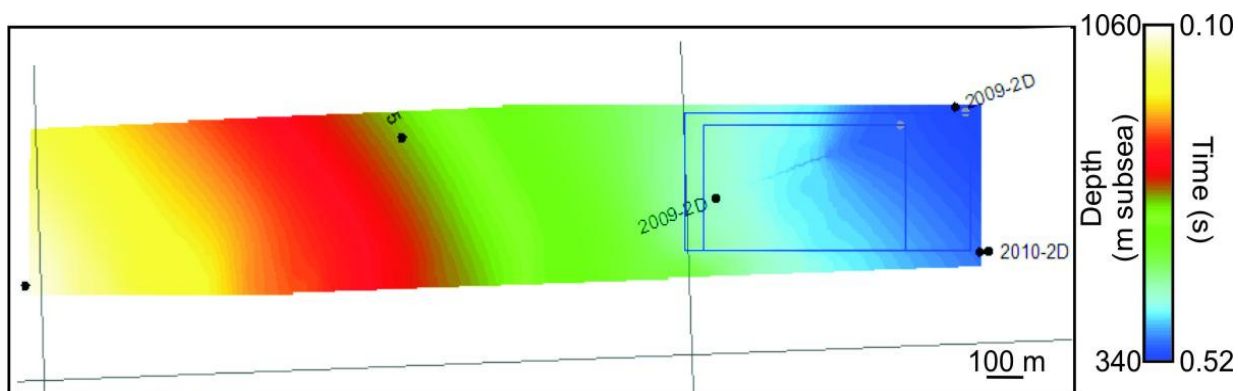
Figure 2-18: Shape map of Lower Paskapoo sand. The scale is shown in depth and time.

2.6 Discussion

The 2D and 3D seismic surveys imagine the shallow layers well. It is possible to define the structure of the formations of interest, especially Lower Paskapoo and Edmonton Group events. The 2D survey shows that the layers above UD have a dip of approximately 35° for a distance of 2.5 km. The 3D survey has a smaller scale (700x300 m) and shows the dipping events in the east-west direction and flat events in the north-south direction. The results, from both the 2D and 3D surveys, complement each other, allowing then the generation of a robust geological model.

Chapter Three: Petrophysics and Fluid Substitution

3.1 Introduction

One of the principal objectives of this dissertation is to evaluate the changes in the physical properties of the target formation due to the injection of CO_2. These petrophysical alterations are expected to be reflected in the seismic response. The principle that leads this analysis is the fluid substitution by using Gassmann Equation, which predicts the changes to bulk modulus and velocity for different pore fluids (Gassmann, 1951), in this case, substitution of pore water with CO_2.

This chapter describes the process of target selection using as reference the nearest well, 12-33-21-2W5; it explains the theory behind Gassmann fluid substitution and the results of applying it in the selected aquifer. It yields significant changes in velocity and reflectivity given the injection of CO_2. Finally simple Amplitude vs. Offset analysis was undertaken for different saturations and angles of incidence.

3.2 Paskapoo Sandstone Aquifer

As mentioned in Chapter 1, in order to select a suitable geological formation for storage CO_2, the presence of a permeable geological section overlain by an impermeable section most be found. The best example would be a clean sandstone and shale trap. The purpose of CO_2 injection for this study is to undertake the research and the analysis of CO_2 sequestration in shallow formations, which is different from industrial projects with deep injections

Having mentioned the previous conditions, the Basal Paskapoo Fm. was chosen as the injection target. Figure 3-1 shows the full target zone from the Basal Paskapoo Fm. to the top of the Edmonton Fm. Logs provided by the borehole measurements include gamma ray, P-wave velocity and density logs. The selected section is from 750-785m in the well and the log data are characterized by low gamma ray, high velocity and high density values which are typical of clean sandstone. Overlying it, there is approximately a 10 m interval with high gamma ray, low velocity and low density values interpreted as shale. This system of a permeable clean sandstone layer overlain by an impermeable

shale seams provides favourable conditions for CO_2 injection. The Lower Paskapoo top is at 770m in the area of study and the Edmonton Fm. is at 805m, obtained from the interpretation of the 3D volume (Isaac and Lawton, 2010a). As mentioned earlier, the well 12-33-21-2W5 will be used as reference and model in order to define the target properties.
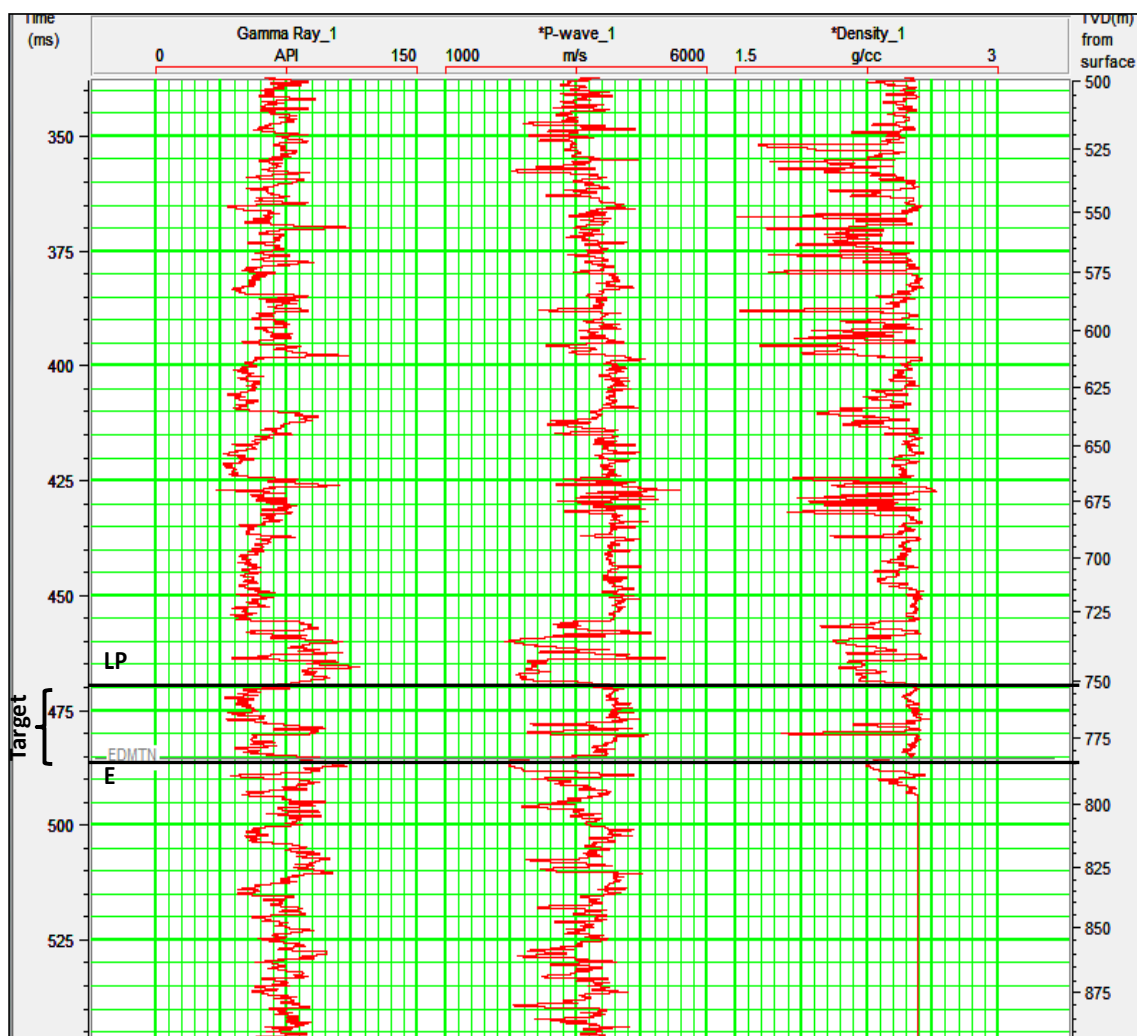
Figure 3-1: Target zone (Basal Paskapoo-Edmonton top) identified in the well 12-33-21-2W5: Gamma ray (track 1), density (track 2) and P-wave (track 3). Lower Paskapoo in blue dashed line.

3.3 Gassmann Fluid Substitution

3.3.1 Theory

Fluid substitution modeling is an important tool in reservoir characterization. In this case, fluid substitution equations were used to predict and evaluate CO_2 injection in the study area, based on well log information, particularly density and sonic logs.

Gassmann's approach is one of the theories used in fluid substitution modelling (Smith et al., 2003). This approach includes three major assumptions: the rock is homogeneous and isotropic, the pore space is completely connected and the fluids are moveable. While many of the proposed models requires several and complicated inputs, Gassmann relations reflect the changes in P-wave and S-wave velocity due to saturation changes with simple inputs. Density and P-wave velocity logs are initial inputs and the imported parameters during substitution are matrix bulk modulus (K_o), frame or dry rock bulk modulus (K^*), porosity (φ) and rock shear modulus (G) (Smith et al., 2003). The changes in fluid saturation will modify the fluid content and therefore, the bulk density (ρ_b) and fluid bulk modulus (K_{fl}) (Smith et al., 2003). Gassmann establishes empirical formulations that relate the saturated rock bulk modulus (K_{sat}) with: porosity, dry rock bulk modulus, mineral matrix bulk modulus and pore filling fluid bulk modulus (Smith et al., 2003). The saturated rock bulk modulus (K_{sat}) was calculated using the following expression:

$$K_{sat} = K^* + \frac{(1 - \frac{K^*}{K_0})^2}{\frac{\varphi}{K_{fl}} + \frac{1 - \varphi}{K_0} - \frac{K^*}{K_0{}^2}} \qquad (3.1)$$

showing that K_{sat} has to be accomplished in a series of steps. Initially, it is necessary define rock parameters such as bulk modulus, shear modulus and bulk density. Bulk modulus (K) is the ratio between the stress increment ($\delta\varepsilon$) and volume strain ($\delta\sigma = \Delta V/V$):

$$K = \frac{\delta\varepsilon}{\delta\sigma}, \qquad (3.2)$$

while shear modulus (G) is the ratio between shear stress and strain (Smith et al., 2003).

Bulk modulus (K) and shear modulus (G) can be related to compression velocity or P-wave velocity (V_p), shear velocity or S-wave velocity (V_s), and bulk density (ρ_b) all of them in saturated state, using the following two equations:

$$K = \rho_b \left(V_p{}^2 - \frac{4}{3} V_s{}^2 \right) \tag{3.3}$$

$$G = \rho_b V_s{}^2 \tag{3.4}$$

Since the shear modulus is insensitive to fluid changes, it will remain constant during the substitution (Smith et al., 2003). Bulk density (ρ_b) is calculated through following expression:

$$\rho_b = \rho_0 (1 - \varphi) + \rho_{fl} \varphi \tag{3.5}$$

where ρ_o is matrix density, ρ_{fl} is fluid density and φ is porosity. Bulk density is going to change depending on the fluid saturation during the substitution.

The first step in Gassmann's substitution is to define porosity values from well log data or to calculate them from density log values or any other log that could give this information (Smith et al., 2003). By rearranging equation 3.5, is possible to get porosity from density values:

$$\varphi = \frac{\rho_0 - \rho_{0b}}{\rho_0 - \rho_{fl}} \tag{3.6}$$

In order to substitute fluids it is necessary to establish their properties. In this case, the two fluids in discussion are water (or brine) and CO_2. Density and bulk modulus values could be obtained from laboratory measurements but in most of the cases some empirical relations are used such as the equations of Batzle and Wang (1992). These yield the density and bulk modulus knowing temperature, pressure, gravity of the fluid (°API in oil) and concentration (ppm in brine). With these input values, a good approximation of fluid properties can be made at certain conditions. Some researchers caution that using the Batzle and Wang (1992) equations as well Gassmann (1951) relations which were developed for a gas-oil-water scenario, might not represent the reality of a CO_2 fluid substitution (e.g. Xu, 2006). The resulting fluid bulk modulus (K_{fl}) after mixing two or more fluids is given by the expression:

$$K_{fl} = \left[\sum_{i=1}^{n} \frac{S_i}{K_i} \right]^{-1} \tag{3.7}$$

where S_i is the saturation and K_i is the bulk modulus of each fluid. This expression can be simplified in the following equation in the case of water and a CO_2 mixture:

$$K_{fl} = \left[\frac{S_w}{K_w} + \frac{(1 - S_w)}{K_c} \right]^{-1} \tag{3.8}$$

where S_w is water saturation, $S_c = 1 - S_w$ is CO_2 saturation, K_w is water bulk modulus an K_c is CO_2 bulk modulus.

Applying the same reasoning explained before, the fluid density (ρ_{fl}) is given by:

$$\rho_{fl} = \sum_{i=1}^{n} S_i \rho_i \tag{3.9}$$

$$\rho_{fl} = S_w \rho_w + (1 - S_w) \rho_c \tag{3.10}$$

where ρ_i represent the density of each fluid, ρ_c is CO_2 density and ρ_w water density.

Fluid bulk modulus and fluid density will manifest the fluid substitution changes and therefore, they will affect the model and define the variations in parameters for seismic modelling.

To establish matrix characteristics, one that needs to determine the matrix bulk modulus (K_o). These values are tabulated for main mineral components such as quartz and calcite among others. Most of the time, the matrix is composed of different kinds of minerals, and in case that fractional content information is available, the bulk modulus can be calculated using Voigt- Reuss-Hill (VRH) equation. It is possible to obtain the bulk modulus (K_{vrh}) using Voigt and Reuss bulk modulus respectively (K_{voigt} and $K_{reuss)}$ (Smith et al., 2003):

$$K_{vrh} = \frac{1}{2} \left[K_{(Voigt)} + K_{(Reuss)} \right] \tag{3.11}$$

Reuss equation is the average of the harmonic mean (it represents the low band), and for the mixture of two components it can be expressed as:

$$K_{(Reuss)} = \left[\frac{F_1}{K_1} + \frac{F_2}{K_2} \right]^{-1} \tag{3.12}$$

On the other hand, the Voigt equation is the average of the arithmetic mean (it represents the upper band):

$$K_{(Voigt)} = [F_1 K_1 + F_2 K_2] \qquad (3.13)$$

K_1, K_2 are the bulk modulus of each mineral and F_1, F_2 are the fraction of mineral in the rock (Smith et al., 2003). In this case, only a single mineral composition was used, assuming clean sand ($K = 38$ GPa).

Another method used to calculate the matrix bulk modulus is Hashin and Shtrikman (1963) which assume a homogeneous mix of minerals and has narrower upper bound than Voigt but keeps the lower bound of Reuss. Hashin-Shtrikman upper bound can be obtained with the following equation:

$$M^{HS} = K^{HS} + \frac{4}{3G^{HS}} \qquad (3.14)$$

where M^{HS} is the P-wave modulus and K^{HS} and G^{HS} are the bulk modulus and shear modulus resulting of the equations:

$$K = K_1 + \frac{\varphi}{(K_2 - K_1)^{-1} + (1 - \varphi)(K_1 - \frac{4}{3}G_1)^{-1}} \qquad (3.15)$$

$$G = G_1 + \frac{\varphi}{(G_2 - G_1)^{-1} + \dfrac{2(1 - \varphi)(K_1 - 2G_1)}{5G_1(K_1 - \frac{4}{3}G_1)}} \qquad (3.16)$$

K_1, G_1 and K_2, G_2 are the bulk modulus and shear modulus of each mineral. The Hashin-Shtrikman lower bound can be related to Reuss relation (Nolen-Hoeksema, 2000). The relation between Voigt, Reuss and Hashin-Shtrikman curves can be seen in Figure 3-2.

To define frame properties or dry rock bulk modulus (K^*), equation 3.1 can be rearranged:

$$K^* = \frac{K_{sat}\left(\frac{\varphi K_o}{K_{fl}} + 1 - \varphi\right) - K_o}{\frac{\varphi K_o}{K_{fl}} + \frac{K_{sat}}{K_o} - 1 - \varphi} \tag{3.17}$$

Bulk modulus (K_{sat}) for the saturated rock is obtained from equation 3.3, and the rest of the elements are obtained from previous steps (Smith et al., 2003). This property is calculated for a saturated rock and remains constant in fluid substitution. Shear modulus, matrix bulk modulus and porosity remain constant as well. Once that we have K* it is possible calculate the rock bulk modulus (K_{sat}), using equation 3.1, for any water/ CO_2 saturation values recalculating each time K_{fl}, ρ_{fl}, and ρ_b (Smith et al., 2003).
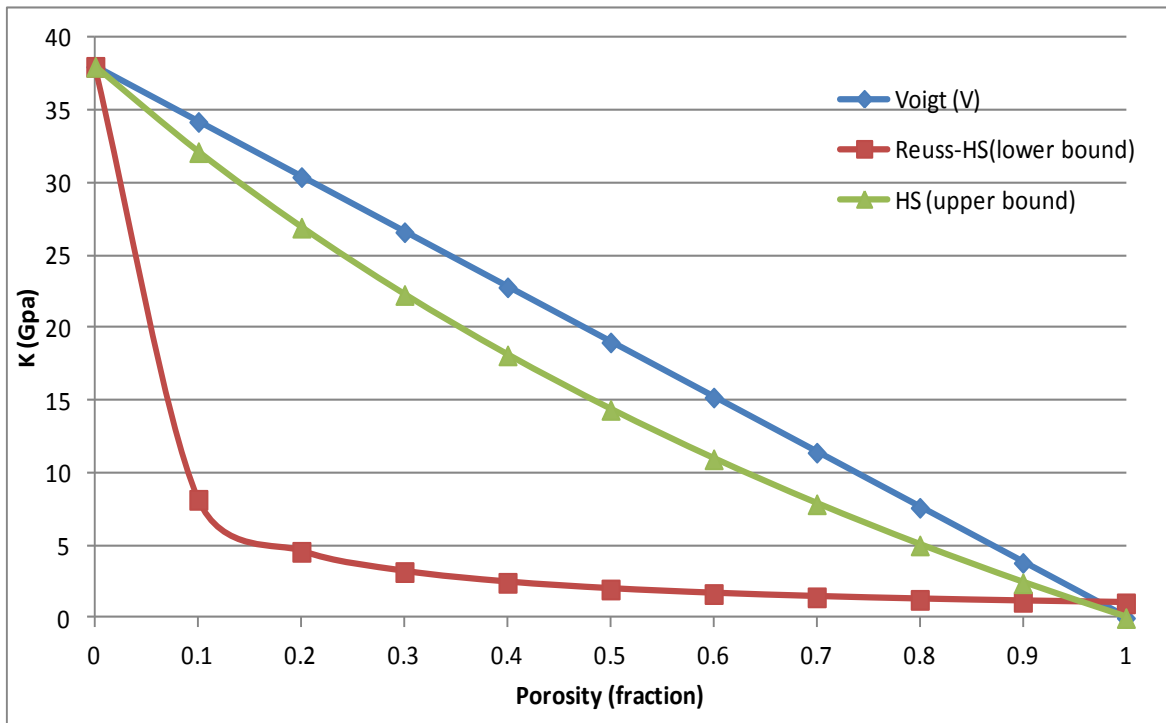
Figure 3-2: Curves of Reuss (R), Voigt (V) and Hashin-Shtrickman (HS), showing bulk modulus variation with the porosity. Using $K_o = 38$ GPa and $G_o = 44$ GPa, clean sandstone parameters (after Hashin and Shtrikman, 1963).

The final step consists of P-wave (V_p) and S-wave velocity (V_s) calculation using the new rock bulk modulus values (K_{sat}) for different CO_2 saturations, using the following equations:

$$V_p = \sqrt{\frac{K_{sat} + \frac{4G}{3}}{\rho_b}}$$ (3.18)

$$V_s = \sqrt{\frac{G}{\rho_b}}$$ (3.19)

The shear modulus (G) calculated from equation 3.4 and the bulk density (ρ_b) is recalculated for each saturation value using equation 3.5 (Smith et al., 2003).

The effects of fluid substitution in a certain formation or stratigraphic section could be evaluated by the changes in P-wave velocity and S-wave velocity during the injection.

3.3.2 Methodology

Gassmann equations were used to estimate the changes in the P-wave velocity and the S-wave velocity after fluid substitution. Having density and sonic log values in the section identified as Basal Paskapoo, an average value for both were obtained, which were used for the input in fluid substitution. The S-wave velocity at 100% water saturation is calculated using equation 3.20:

$$V_s = \frac{V_p}{1.9}$$ (3.20)

where 1.9 is taken as a average value of V_p/V_s (Hyndman, 1979). From the density log, a porosity log was created using equation 3.5. Matrix density will be given by theoretical sandstone density value of 2650 kg/m^3 and the fluid density of fresh water is 1000 kg/m^3.

With all the elements, CO_2 substitution was performed. First, complete water saturation condition is set. In order to solve the Gassmann equation (equation 3.1), it was necessary to follow the steps described previously.

1) Calculate porosity value from equation 3.6 using the bulk density for 100% water saturation.

2) Define fluid properties: bulk modulus and density. As mentioned, these values depend on pressure and temperature and can be calculated with Batzle-Wang equations (Smith et al., 2003). Due to the lack of precise information, the temperature (T) at the study site was estimated using geothermal gradient (G_t):

$$T(410m) = G_t(410m) + T(surface) \quad\quad\quad (3.21)$$

and the pressure (P) was calculated using hydrostatic pressure gradient (H_p):

$$P = H_p h \quad\quad\quad (3.22)$$

where H_p=9.792 kPa/m and the chosen depth (h) is 750m.

The geothermal gradient considered is 27 degrees C/km in Alberta (Hitchon, 1984) and estimating a surface temperature of 15° C, the approximate temperature in the Paskapoo sand is 35° C. For the pressure, the column above the objective (h) will be 750 m having a pressure of 7.510 MPa.

With these values and Batzle-Wang calculations it is possible to obtain the CO_2 bulk modulus $K_c = 0.02$ GPa and density $\rho_c = 340$ kg/m^3. The expected phase of CO_2 under this conditions would be close to super critical, as we can see in the graph of Piri et al., (2005) shown in Figure 3-3. The estimated water bulk modulus is $K_w = 2.39$ GPa, and fresh water density $\rho_w = 1000$ kg/m^3 due to information about salinity of the area, such as Grasby (2008), who analysed the chemical composition of aquifers in Paskapoo Formation and found a concentration of calcium ~20mg/l^3.

Having the individual characteristics of each fluid, K_{fl} and ρ_{fl} were then calculated using equations 3.8 and 3.10 respectively, at different CO_2 saturation states.

3) Define matrix properties: K_0 matrix and ρ_0 matrix. In this case we consider that the matrix is composed of perfect sandstone (quartz), so the K and ρ values are theoretical values of this mineral and they are not affected by pressure or temperature conditions. Since $K_0 = 37$ GPa and $\rho_0 = 2650$ kg/m^3. According to lithological and stratigraphical characteristics, Paskapoo Formation contains clay and limestone.

4) Calculate bulk density by equation 3.5 with each new fluid density.

5) Calculate frame bulk modulus using equation 3.17 and introducing some of the previously mentioned values for 100% water saturation. K_{sat} is calculated with equation 3.3. K* value remains constant and is not affected by the substitution.

6) Calculate the rock bulk modulus (K_{sat}) with equation 3.1. This element and bulk density (ρ_b) is going to define the P-wave velocity further values. K_{sat} will vary according to the resultant K_{fl}.

7) Determine P-wave velocity and S-wave velocity values with equations 3.18 and 3.19, calculating previously the shear modulus G by equation 3.4. The bulk density and the rock bulk modulus were recalculated with each CO_2 saturation value in increment of 10% yielding giving eleven P-wave velocity and S-wave velocity values.
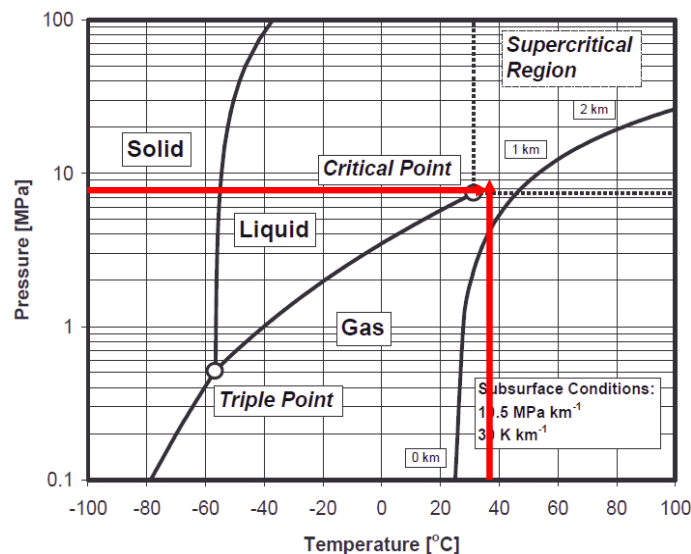
Figure 3-3: Temperature and pressure phase diagram for pure carbon dioxide. The red arrows represent the pressure (7.510 MPa) and temperature (35.7^o C) in the target. It shows that the CO_2 is in super critical phase (After Piri et al, 2005).

3.3.3 Fluid Substitution Result over the Sandstone Target

Gassmann equations were developed using a Microsoft Excel spread sheet. Important results are the P-wave velocity, the S-wave velocity, the P-wave velocity change, the S-wave velocity change and Vp/Vs change, all of them for CO_2 substitution from 0% to 100% saturation (Table 3-1). The P-wave velocity values drop abruptly

between 0 to 0.2 CO_2 saturation, and starts to increase slowly after 0.3 CO_2 saturation, as shown in Figure 3-4; this trend was reported by Domenico (1977). From equation 3.18, this is evident from the relation of P-wave velocity with K_{sat} and ρ_b. With CO_2 saturation increasing the rock bulk modulus (K_{sat}) decreases and therefore the P-wave velocity decreases. However, at the same time the bulk density (ρ_b) diminishes and thus the P-wave velocity will increase. From 0 to 0.2, the decrease in K_{sat} values is more dominant than the decrease in ρ_b resulting in an overall decrease in the P-wave velocity, but from 0.3 CO_2 saturation, the lower density values cause a subtle increase in the P-wave velocity. The maximum decrease in P-wave velocity is 7 %.

On the other hand, the S-wave velocity increase is small, but it is directly proportional to CO_2 saturation (Table 3-1 and Figure 3-5). From equation 3.19, is possible to see that the S-wave velocity change depends only on bulk density variations since the shear modulus remains constant and it is not affected by fluid substitution. However, the average increase of the S-wave velocity with respect to 100% water saturation is only 0.7%.

Table 3-1: Gassmann fluid substitution results and input values (porosity, P-wave velocity, S-wave velocity, bulk modulus, Vp/Vs and shear modulus). Depth of 750 m in the well site. Reservoir thickness 35 m.

Water Sat	CO_2 Sat	K_{fl} (GPa)	Density fluid (kg/m^3)	Bulk density (Kg/m^3)	K_{sat} (GPa)	V_p (m/s)	V_s (m/s)	V_p change (%)	V_s change (%)	V_p/V_s (change) (%)	dt(ms)
1	0	2.390	1000	2505.08	27.72	4189.00	2204.74	0.000	0.000	0	0
0.9	0.1	0.186	934	2499.28	21.69	3895.45	2207.29	-7.008	0.116	-7.115	1.22
0.8	0.2	0.097	868	2493.48	21.51	3890.84	2209.86	-7.118	0.232	-7.333	1.24
0.7	0.3	0.065	802	2487.69	21.45	3892.12	2212.43	-7.087	0.349	-7.410	1.23
0.6	0.4	0.049	736	2481.89	21.42	3894.99	2215.01	-7.019	0.466	-7.450	1.22
0.5	0.5	0.040	670	2476.09	21.40	3898.52	2217.60	-6.934	0.584	-7.474	1.21
0.4	0.6	0.033	604	2470.30	21.38	3902.41	2220.20	-6.842	0.702	-7.490	1.19
0.3	0.7	0.028	538	2464.50	21.37	3906.50	2222.81	-6.744	0.820	-7.502	1.17
0.2	0.8	0.025	472	2458.70	21.37	3910.73	2225.43	-6.643	0.939	-7.511	1.15
0.1	0.9	0.022	406	2452.91	21.36	3915.06	2228.06	-6.540	1.058	-7.518	1.13
0	1	0.020	340	2447.11	21.36	3919.46	2230.70	-6.434	1.178	-7.523	1.12
								6.83	0.64	7.43	1.1914

Depth(m)	Porosity	Vp_1(m/s)	Vs_1(m/s)	K*(GPa)	Vp/Vs	Gsat(Pa)
750	0.09	4189.000	2204.737	25.44461	1.9	1.22E+10
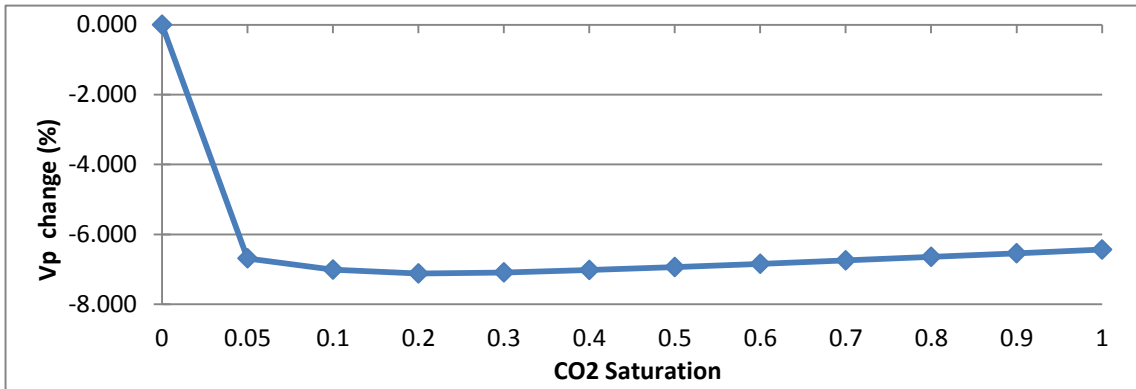
Figure 3-4: P-wave velocity change versus CO_2 saturation (after Domenico, 1977)
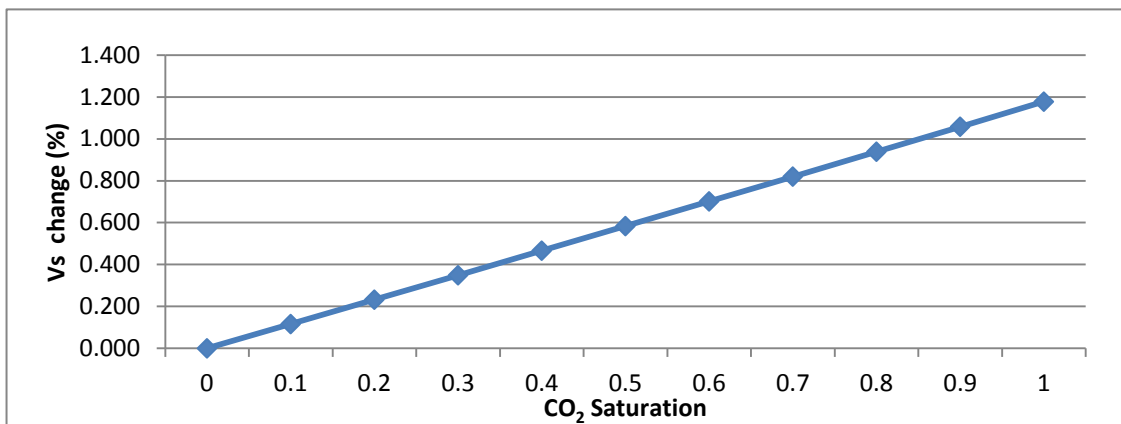
Figure 3-5: S-wave velocity change versus CO_2 saturation

Vp/Vs decrease with CO_2 saturation due to the increase of Vs and a decrease in Vp (Table 3-1) with a maximum decrease of 8%. Figure 3-6 shows a sharp drop from 0 to 0.1 CO_2 saturation, becoming nearly constant for higher values. An extra element included in Table 3-1 is the time delay. The time delay of the basal reflector was calculated using the equation:

$$\Delta T = T_2 - T_1 = 2h\left(\frac{1}{V_2} - \frac{1}{V_1}\right) \tag{3.23}$$

where h is the thickness of the layer (35 m), V_2 is the P-wave velocity of the injection zone for the given saturation stage and V_1 is P-wave velocity for 0% CO_2. As CO_2 saturation increases a time delay trough the reservoir is produced; it takes more time for the P-wave to travel the through the zone of interest. The average two-way delay time is 1.2 msec.
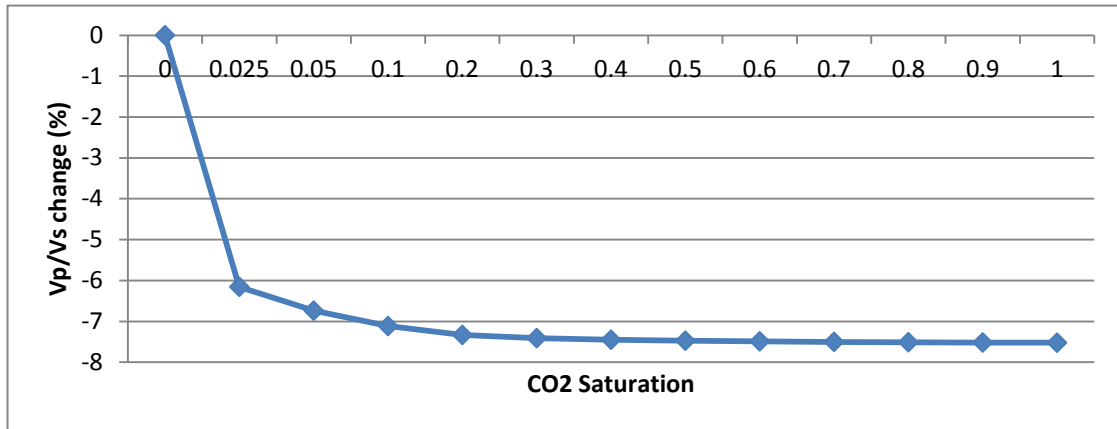
Figure 3-6: P-wave velocity/S-wave velocity change versus CO₂ saturation

After applying fluid substitution over 750-785m in 12-33-21-2W5 well, synthetic seismic traces for each CO_2 saturation states were generated, some alteration can be evaluated. Figure 3-7 shows Gamma Ray (track1), P-wave velocity and S-wave velocity (track 2), density (track 3) and synthetic seismograms at different CO_2 saturation values, 0 % to 100 %. The first synthetic trace represents the 100% water saturation or 0% CO_2 saturation. The subsequent traces increase 10% CO_2 saturations until 100% stage. It is now possible to evaluate property changes due to CO_2 substitution, specifically: velocity, time delay and amplitude of the wavelet.

The parameters selected to generate the synthetic seismogram were: zero phase 70 Hz Ricker wavelet. A 70 Hz frequency is a reasonable value to be used for shallow depth; furthermore, it would be possible to resolve the target zone which has 35 meters of thickness. This frequency provided the resolution requirements in the area of interest:

$$\lambda = \frac{V}{f} \tag{3.24}$$

where V is the P-wave velocity in the layer of interest, f is the frequency and λ is the wave length. Calculating with the corresponding values:

$$\lambda = \frac{4189 \frac{m}{s}}{70 \frac{1}{s}}$$

$$\lambda = 59.84 \, m$$

$$\lambda = 59.84 \, m$$

$$Resolution \sim \frac{\lambda}{4} \tag{3.25}$$

$$Resolution \sim 15.06 \, m$$

it was found that the resolution is approximately 15 m and the thickness of the layer is 35 m.

Figure 3-8 shows the synthetic seismogram with different CO_2 saturation values. The variation between synthetic traces is subtle. Looking at the basal reflection (785 m) a subtle time shift is evident from 0 to 100% CO_2 saturation. Small amplitude changes in the top reflection (750m) are visible with increasing CO_2 saturation (Figure 3-9). Changes in the P-wave velocity correspond with the variations in traces (Figure 3-10); there is a P-wave velocity reduction. The main decrease occurs from 0 to 20% CO_2 saturation, but no changes are evident at higher CO_2 saturation.
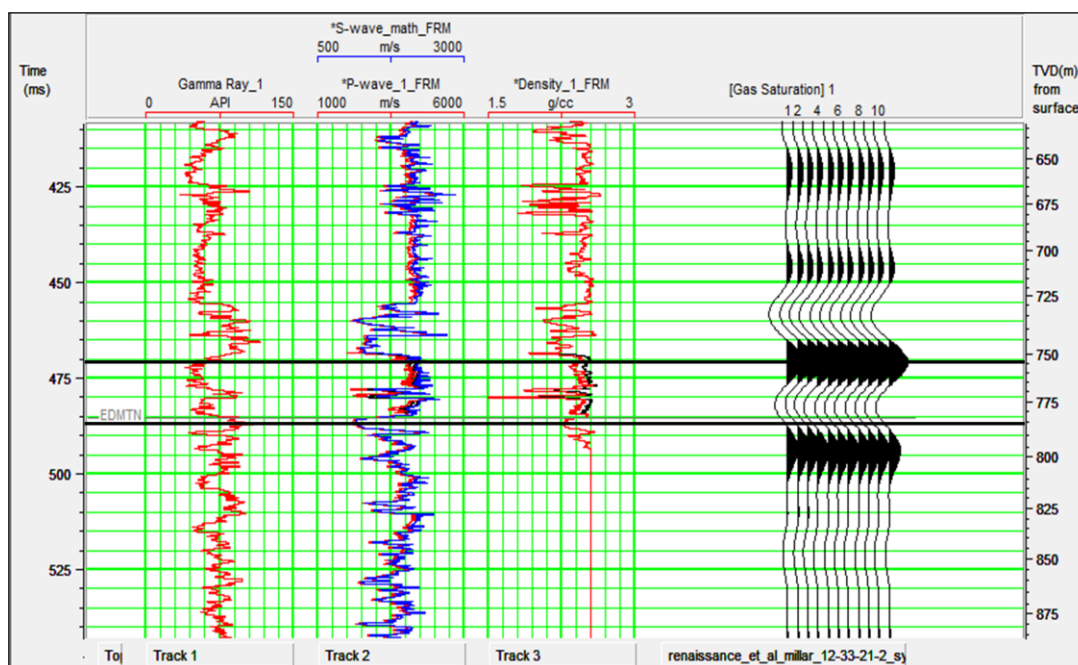
Figure 3-7: 12-33-21-2W5 logs: Track 1: Gamma ray in red, Track 2: P-wave in red and S-wave in blue both after fluid substitution,   Track 3: in red density after fluid substitution and in black before substitution (clear diminution of density after the substitution), Final tracks: synthetic traces at different CO_2 saturation values, going from 0% to 100% (1-10).
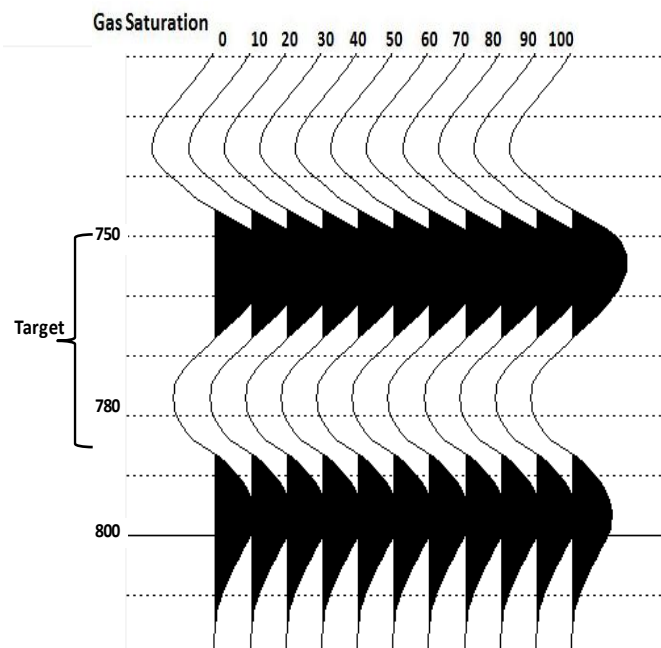
Figure 3-8: Synthetic seismograms for different saturation values. Zone of fluid substitution is shown by the brackets (770-785m).
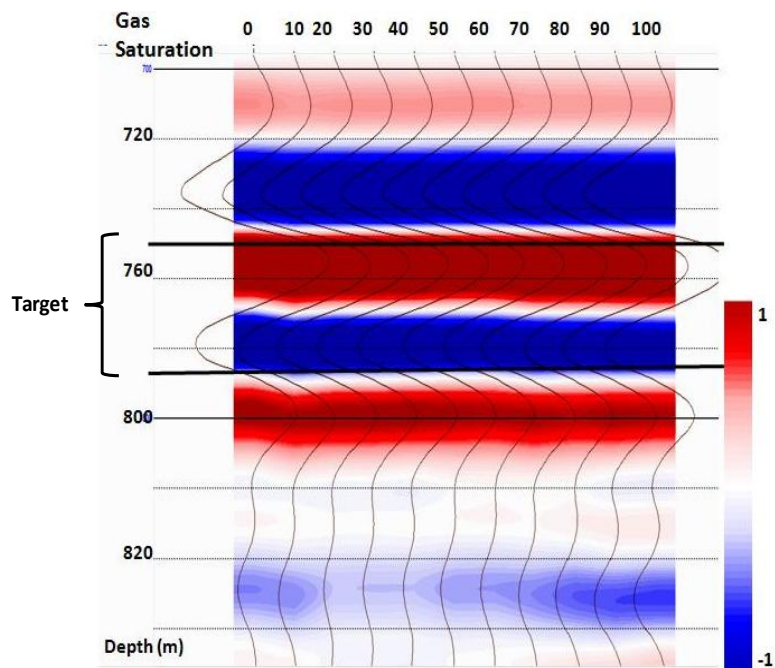
Figure 3-9: Synthetic traces, amplitude variation with increasing CO_2 saturation. Amplitude changes are evident at the top of the injection zone (750 m)
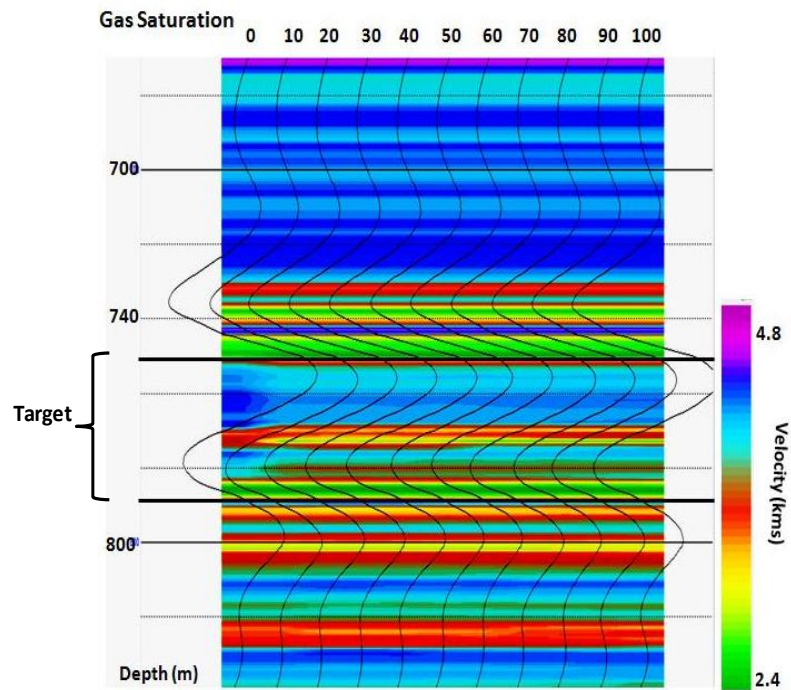
Figure 3-10: Synthetic traces, velocity variation with increasing CO$_2$ saturation. The P-wave velocity has an evident decrease from 0 to 20% CO$_2$ saturation but there is no appreciable change for higher CO$_2$ saturation.

3.3.4 AVO Analysis

It has been proven earlier that P-wave velocity and S-wave velocity present changes with CO$_2$ saturation. However, an important element for seismic monitoring of the CO$_2$ is the Amplitude Vs Offset (AVO) analysis. AVO combines V_p, V_s and ρ, to calculate the changes in amplitude with the angle of incidence, therefore should be more sensitive in the discrimination of CO$_2$ (Brown and Bussod, 2007). The method used was Shuey approximation which is a less complex approximation to the Zoeppritz equation (Shuey, 1985). It calculates the reflection coefficient for diverse geological models and different angles of incidence (Shuey, 1985). This approximation used for two-layers models (Figure 3-11), layer 1 is the medium above the injection zone and layer 2 is the injection target. The variables involve are: V_{p1}, V_{s1} and ρ_1 are the P-wave velocity, S-wave velocity and density of the layer 1. V_{p2}, V_{s2} and ρ_2 are the P-wave velocity, S-wave velocity and density of the layer 2. The values for the layer 1 were calculated from the log information resulting in $V_{p1} = 3497$ m/s, $V_{s1} = 1665$ m/s and $\rho_1 = 2390$ kg/m^3. The

values for layer 2 will depend on the CO_2 saturation and were calculated earlier through Gassmann. V_{p2}, V_{s2} and ρ_2 are summarized in Table 3-2. Even with a 100% CO_2 saturation V_p, V_s and ρ of layer 2 will be higher than in layer 1. This characteristic reflects a AVO Class 1 were the sand has higher impedance than the surrounding media (generally shale) (Rutherford and Williams, 1989). The reflection coefficient of the sand is positive at zero offset and starts decreasing with offset, only reaching negative values in far offsets (Rutherford and Williams, 1989).
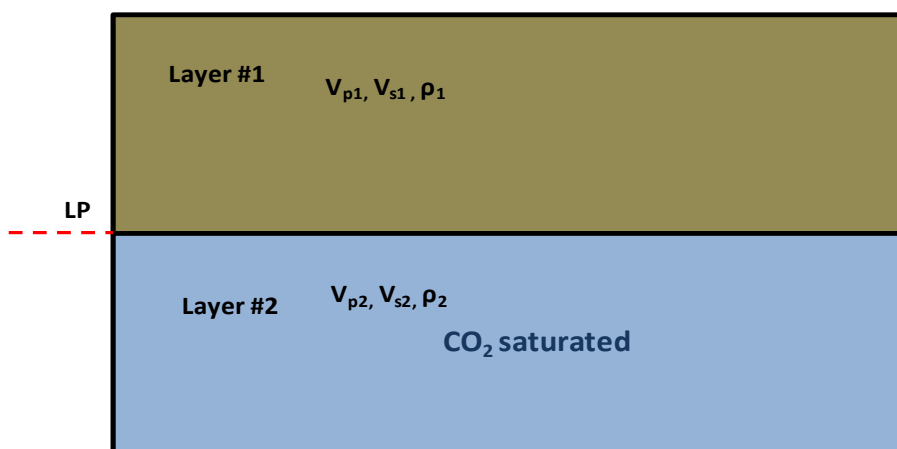
Figure 3-11: Two layers model for Shuey's equation: Layer #1 is the medium above the target zone, Layer 2 is CO_2 saturated. Both layers are separated by Lower Paskapoo top (LP).

Table 3-2: V_p, V_s and ρ values for layer 2, at different CO_2 saturation levels.

CO_2 Saturation	Bulk density (Kg/m^3)	V_p (m/s)	V_s (m/s)
0	2505.08	4189.00	2204.74
0.1	2499.28	3895.45	2207.29
0.2	2493.48	3890.84	2209.86
0.3	2487.69	3892.12	2212.43
0.4	2481.89	3894.99	2215.01
0.5	2476.09	3898.52	2217.60
0.6	2470.30	3902.41	2220.20
0.7	2464.50	3906.50	2222.81
0.8	2458.70	3910.73	2225.43
0.9	2452.91	3915.06	2228.06
1	2447.11	3919.46	2230.70

Several variables and equations need to be developed before obtaining the final Shuey's equation. First we have that V_p is the average P-wave velocity obtained from:

$$V_p = \frac{\Delta V_p}{2},$$

$$(3.26)$$

where $\Delta V_p = V_{p2} - V_{p1}$. V_s is the average S-wave velocity obtained the same way:

$$V_s = \frac{\Delta V_s}{2},$$

$$(3.27)$$

where $\Delta V_s = V_{s2} - V_{s1}$. ρ is the average density given by :

$$\rho = \frac{\Delta \rho}{2},$$

$$(3.28)$$

where $\Delta \rho = \rho_1 - \rho_2$. σ_1 and σ_2 is the Poisson ratio in layer 1 and 2. σ is the average Poissons ratio:

$$\sigma_1 = \frac{\Delta V_{p1}^2 - 2V_{s1}^2 \rho}{2(V_{p2}^2 - V_{s1}^2)}$$

$$(3.29)$$

$$\sigma_2 = \frac{\Delta V_{p2}^2 - 2V_{s2}^2 \rho}{2(V_{p2}^2 - V_{s2}^2)}$$

$$(3.30)$$

$$\sigma = \frac{\Delta \sigma}{2}$$

$$(3.31)$$

where $\Delta \sigma = \sigma_2 - \sigma_1$ is the Poisson ratio variation. A_0 and B_0 are coefficients for the calculation of Shuey's equation, calculated:

$$A_0 = B_0 - 2(1 + B)\frac{1 - 2\sigma}{1 - \sigma}$$

$$(3.32)$$

$$B_o = \frac{\Delta V_p / V_p}{\frac{\Delta V_p}{V_p} + \frac{\Delta \rho}{\rho}}$$

$$(3.33)$$

Finally Shuey's approximation can be expressed as:

$$R_i = R_o + \left(A_o R_o + \frac{\Delta \sigma}{(1 - \sigma)^2}\right) sin^2 \theta_i + \frac{\Delta \sigma}{2V_p}(tan^2 \theta_i - sin^2 \theta_i) \quad (3.34)$$

where: R_i is the reflection coefficient for the incident angle θ_i and can be expressed as R_{pp} (only includes P-P reflection), R_o is the reflection coefficient at zero offset

$$R_o = \frac{V_2\rho_2 - V_1\rho_1}{V_2\rho_2 + V_1\rho_1} \tag{3.35}$$

Shuey's equation can be reduced to:

$$R_{pp} = A + B\sin^2\theta_i + C(\tan^2\theta_i - \sin^2\theta_i) \tag{3.36}$$

where A is the reflection coefficient at zero offset, B, called gradient and describes the small angle behaviour (<30 degrees) and C describe large angles (Brown and Bussod, 2007). For small offset geometries, the equation can be simplified:

$$R_{pp} = A + B\sin^2\theta_i \tag{3.37}$$

The changes in amplitude versus offset (AVO) were evaluated first, calculating the parameter A (equation 3.35) and B of Shuey's equation (3.34). Both parameters are related to the velocity and density; therefore, changes with CO_2 saturation are expected. Table 3-3 summarizes the results, showing decreases in both parameters, A decreases approximately 25% and B decreases approximately 13%. Comparing these results with the results obtained from Gassmann substitution of V_p (change of 7 %), V_s (change of 0.7 %) and V_p/V_s changes 8%) (Table 3-1), it is possible to see that the changes in the AVO parameter, A and B are considerable higher. In conclusion, it has been shown that Shuey's parameters are more sensitive to the CO_2 saturation changes. The values A and B vs. CO_2 saturation are represented in Figure 3-12 showing that for higher concentrations of CO_2 the amplitude will decrease. Zero offset reflectivity (A) has a quick decrease from 0% to 10% CO_2 saturation having a subtle decrease in the subsequent stages. CO_2 will reduce the bulk density and therefore the reflectivity contrast. B (gradient) vs. CO_2 saturation, shows a different tendency, having the same significant decrease from 0% to 10%, but starts subtle rise after 20% CO_2 saturation similar to V_p vs. CO_2 saturation graph (Figure 3-4).

Table 3-3: Changes in AVO parameters: *A* and *B*, with CO_2 saturation.

CO_2 Saturation	*A* (R_0)	*B* (grad)	*A* change (%)	*B* change (%)
0	0.14674	-0.2248	0	0
0.1	0.11068	-0.2582	-24.58	-14.83
0.2	0.10895	-0.2586	-25.76	-15.04
0.3	0.10796	-0.2584	-26.43	-14.95
0.4	0.10717	-0.2580	-26.97	-14.78
0.5	0.10646	-0.2576	-27.45	-14.57
0.6	0.10579	-0.2571	-27.90	-14.35
0.7	0.10515	-0.2565	-28.34	-14.12
0.8	0.10452	-0.2560	-28.77	-13.88
0.9	0.10390	-0.2555	-29.19	-13.63
1	0.10329	-0.2549	-29.61	-13.38
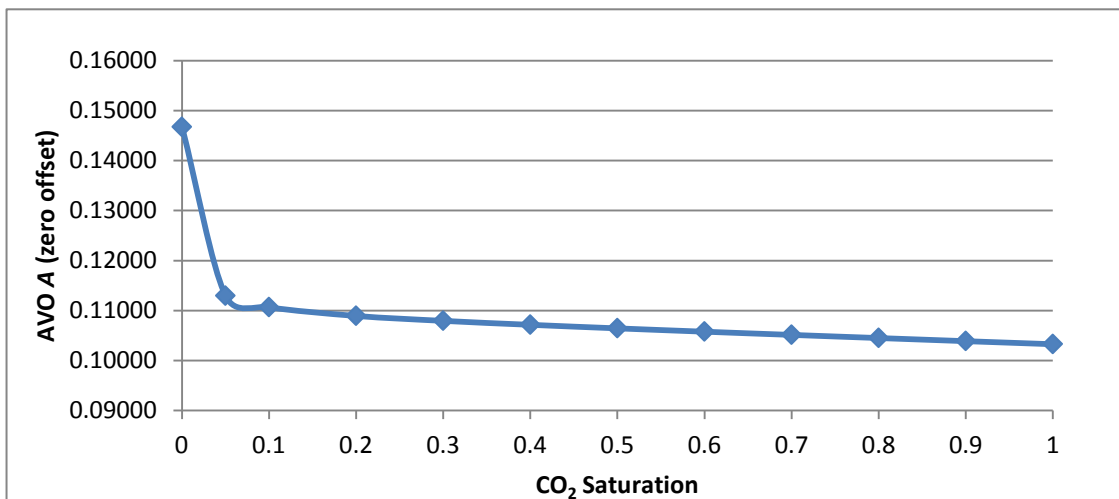
a)
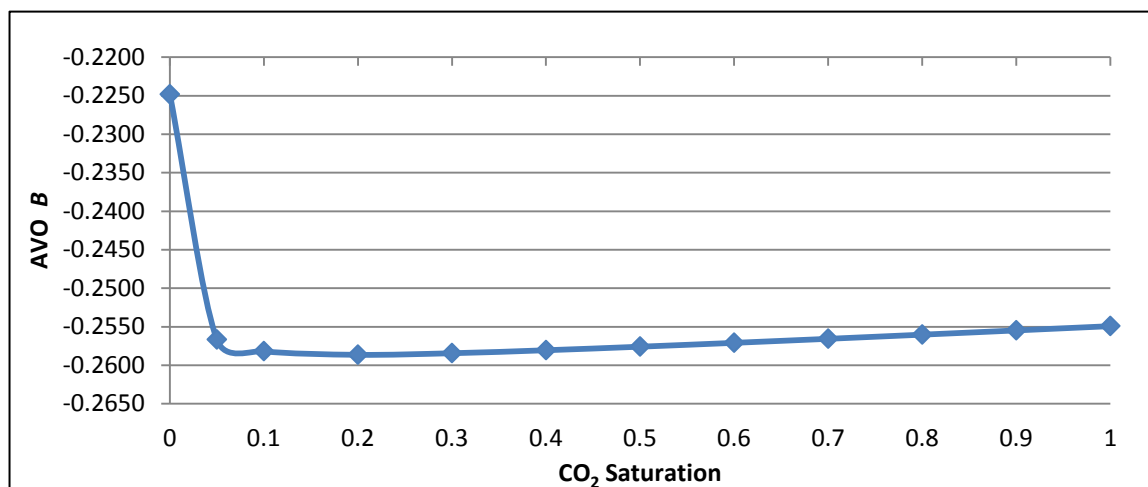
b)

Figure 3-12: Shuey's approximation parameters: A (a) and B (b) vs. CO_2 saturation.

In addition, the P-wave reflectivity (R_{pp}) with respect to the offset or angle of incidence was evaluated. Shuey's approximation (equation 3.36) was applied for three CO_2 saturation stages: 0%, 20% and 60%, taking a maximum angle of 25 degrees which is close to the incident angle for the maximum offset. Table 3-4 shows the R_{pp} values at different stages of CO_2 saturation (0%, 20% and 60%) and with different incidence angles. The graph presented in Figure 3-13 shows the curves at each saturation stage. The reflectivity decreases with increasing incident angle. As expected, the curve shows the tendency of an AVO Class 1 where the reflectivity decrease without reaching negative values for small angles ($< 30^o$). In terms of CO_2 saturation, all the curves have the same trend, with a significant drop between 0% to 20%.

Table 3-4: R_{pp} coefficient values at different CO_2 saturation stages (0%, 20% and 60%) and its changes with the angle of incidence.

Angle (Degrees)	R_{pp} (0%CO_2)	R_{pp} (20%CO_2)	R_{pp} (60%CO_2)
0	0.147	0.112	0.109
5	0.145	0.110	0.107
15	0.132	0.095	0.092
25	0.107	0.065	0.063
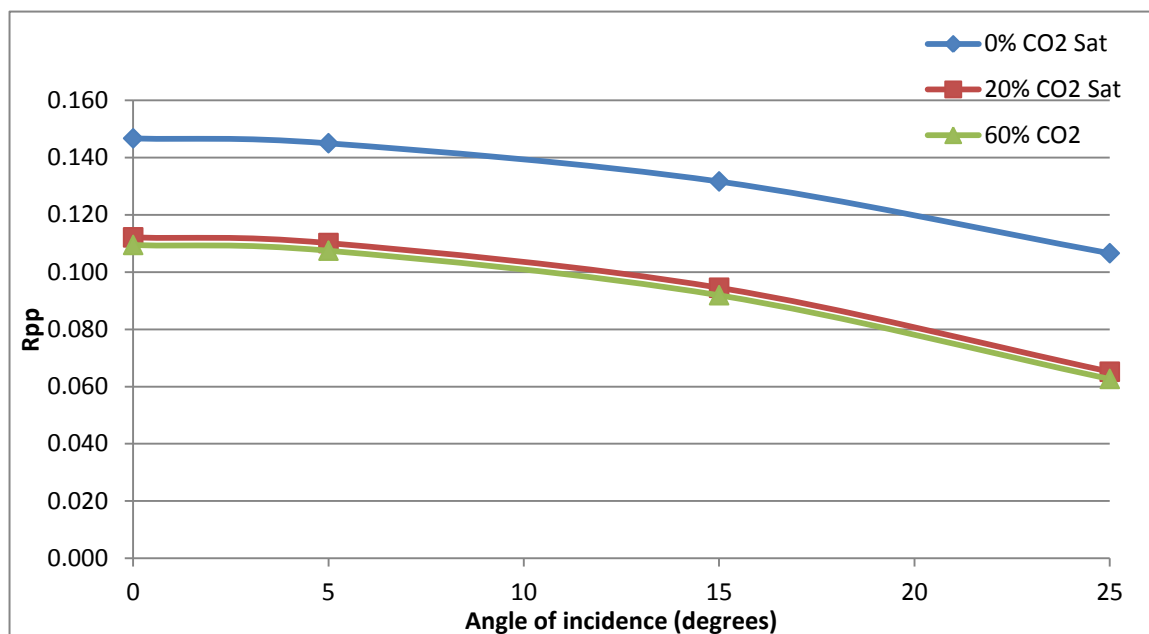
Figure 3-13: R_{pp} vs Angle of incidence with different CO_2 saturation stages (0%, 20% and 60%).

3.4 Discussion

It was found that Gassmann theory is a practical and useful tool for fluid substitution models. Direct evaluation and synthetic seismograms reflect the effects of CO_2 saturation. Applying this principle over the selected target, proves that is possible to observe subtle changes (specially in P-wave velocity) even with small CO_2 concentrations. In addition, AVO analysis using Shuey's approximation demonstrates that the AVO parameters (*A* and *B*) prove to be sensitive to CO_2 saturation increment. The biggest change will occur from 0 to 20 % CO_2 saturation, and it will have a slight decrease for the next stages. Evaluating the changes in reflectivity due to incident angle, it was found that for larger angles, the reflectivity decreases.

Chapter Four: 2D Seismic Modelling

4.1 Introduction

This chapter discusses one of the fundamental objectives of this thesis; the seismic modelling and feasibility of monitoring a CO_2 volume after being injected into Lower Paskapoo sandstone aquifer. First, a 2D geological model of the site was generated to represent the structure and stratigraphy of the Rothney Observatory area. In addition, the size and shape of the plume according to the final injection volume was estimated. This plume was included as a new interface in the geological model and it represents the post-injection scenario. Subsequently, a 2D seismic simulation was performed using the geological model, reproducing the seismic response of the model before and after CO_2 injection. The final objective was to evaluate the time-lapse difference to demonstrate whether seismic data can be used to monitor the CO_2 plume in the sandstone target.

4.2 2D Local Geological Modelling

4.2.1 Local Geological model design

A 2D geological model of the area was generated using Norsar2D software. The model represents the structure in the zone of interest in an 8 km long cross-section, within the eastern Rocky Mountain Foothills. The idea of developing a long section is to include all the outcrop information, making it possible to observe any up-dip migration. The main elements evaluated in order to create the geological model were: geological background, regional model and well log information.

The geological background, given in Chapter 1, was used as reference in order to understand the local geology. A cross-section with the structural style of the southern Rockies was presented in Figure 1-5, characterized by flat layers in the outer Foothills, but increasingly dominated by folds and faults towards the hinterland. There is a low deformation of the Tertiary deposits that outcrop in the nearby area of the Rocky Mountains Foothills (Wright et al., 2008). This information was combined with the seismic interpretation of the 2010 surveys described in Chapter 2 to develop a more

accurate model. The 800x600 m 3D model shows a gentle east-west dip and flat layers in the north-south directions direction. The 2.5 km 2D line shows a more extensive dipping area, therefore higher degrees, including outcropping reflectors of Middle Paskapoo (Figure 2-17). From the seismic interpretation the key formation tops were identified that were part of the model: Middle Paskapoo A sand (MPA), Middle Paskapoo B sand (MPB), Lower Paskapoo sand (LP), Edmonton Group (E), Upper Detachment (UD), Lower Detachment (LD), Belly River (BR), Milk River (MR), Cardium (C) and Mississippian (M). In this case, only the layers from MPA to ED were included in the seismic modelling.

In terms of stratigraphy and layering it was necessary to make use of the well information. In Chapter 3 it was explained the target selection from the well 12-33-21-2W5 as a reference log and data source. In order to decide what layers or interfaces to include, the main shallow formation tops identified in the logs and seismic were taken into consideration. Basal Paskapoo is the sandstone target, between LP and E (770-805m at the approximate site of injection). In addition to the mentioned tops, fourteen more tops were estimated from the gamma ray and sonic logs, composed of sandstone and shale. From the log information, the velocity and density values were estimated between each of the layers. Finally, eighteen layers were defined in the model and the average velocity and density between each of them were obtained from the log information. Table 4-1 summarizes the velocity and density values for each layer.

Table 4-1: Velocity and density values for each layer of the 2D model. The target layer, LP, is marked in yellow

Layers	Interfaces	Depth to top(m)	Velocity (m/s)	Density (kg/m^3)
1	Surface-Shallow	0	1900	2300
2	Shallow-MPA	100	2860	2250
3	MPA-MPB	265	3498	2390
4	MPB-4	380	4216	2509
5	#4-#5	420	3326	2430
6	#5-#6	440	3900	2493
7	#6-#7	485	3630	2337
8	#7-#8	570	4022	2473
9	#8-#9	590	3823	2239
10	#9-#10	610	4215	2430
11	#10-#11	635	3647	2273
12	#11-#12	650	4161	2426
13	#12-#13	670	3131	2272
14	#13-#14	675	4200	2438
15	#14-#15	730	3382	2305
16	#15-LP	752	4246	2504
17	LP-E	770	3426	2280
18	E-#18	805	4131	2505
19	#18	985	2547	2280

4.2.2 Resulting Geological Model

The model was created using Norsar2D Model Builder. This tool allows you to define the architecture of the geological structure by creating a series of interfaces. The position of each interface is given by the positioning of a series of points in an X and Y coordinates that together will form the line of the interface. In this case the rectangular position is given inside the limits of X= (0.0, 8.0) and Y= (0.0, 1.2) km. Once the interfaces are created, the space between each of them represents a block. The blocks have specific properties such as density, P-wave velocity and S-wave velocity. Density and P-wave velocity values were obtained from well logs shown in Table 4-1, while S-wave velocity was calculated using Vp/Vs equal to 1.9. The compilation of blocks and interfaces form the baseline geological representation shown in Figure 4-1. Towards the

Foothills, in the west, the surface dips increase to about 35°, and flatten towards the east. The 16th layer is the sandstone target, between 770-805 m depth, in the injection area, surrounded by Lower Paskapoo Formation and Edmonton Group.
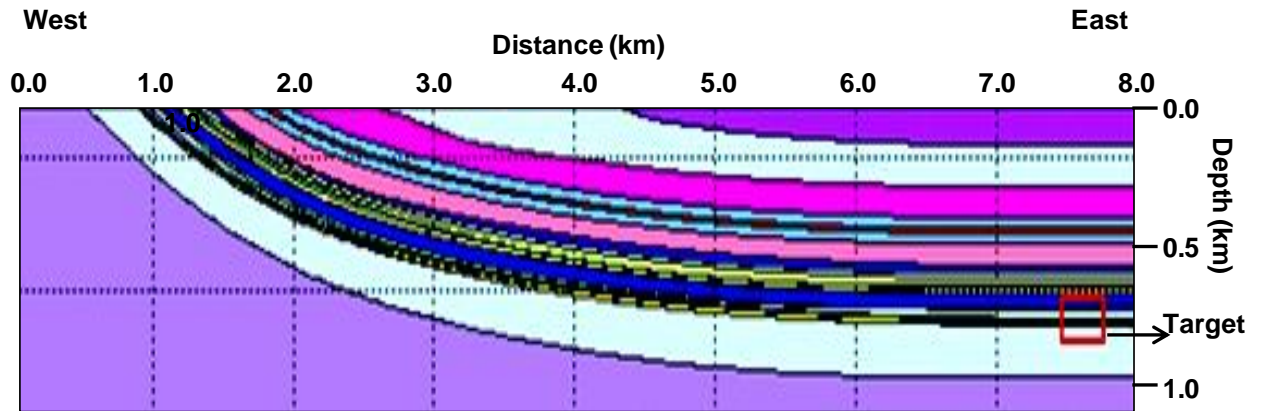
Figure 4-1: 2D geological model of the area. Target layer marked by an arrow and injection zone with a red square.

4.3 Simulated CO$_2$ plume

There are several techniques that can be applied in order to estimate the volume of CO$_2$ trapped in geological formations, based on similar methods used in oil and gas and ground water reservoirs (Frailey, 2009). They are two fundamental types: static and dynamic. The first approach requires rock and fluid properties while the second method requires information about active injection, injection volumes and reservoir pressure (Frailey, 2009). The technique selected for this project is static, more specifically the volumetric method, which is based on the following formula:

$$G_{CO2} = Ah\phi E \tag{4.1}$$

where G$_{CO2}$ is the CO$_2$ volume, A is the area, h is the thickness, ϕ is the porosity and E is the efficiency which can be equated to average saturation as well. G_{CO2} is given by:

$$G_{CO2} = m/\rho \tag{4.2}$$

where m is the mass of CO$_2$ and ρ is the density under the specific temperature and pressure conditions.

The geometry of the expansion considered in this project is a disk or cylindrical dispersion, having an area of:

$$A = \pi r^2 \tag{4.3}$$

where r is the radius of the disk of CO_2 expansion. By rearranging the volumetric formula and introducing the previous expression, r is obtained using the following equation:

$$r = \sqrt{G_{CO2}/\pi h \phi E} \tag{4.4}$$

The simulated amount of CO_2 was 3000 tonnes, considered to be the maximum injected mass after 3 years of injection. It is important to notice that even when the estimation of the plume size was made in 3D the presented geological model is in 2D, therefore the calculated cylinder was translated into a rectangular shape. The disk model can be seen in Figure 4-2.
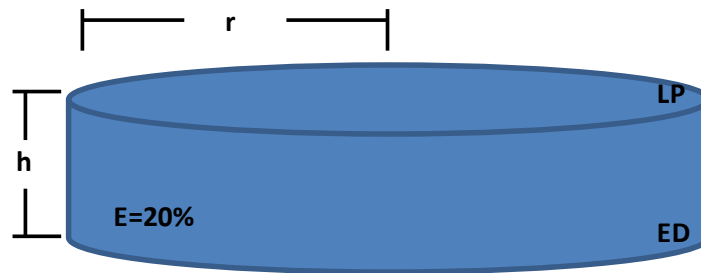
Figure 4-2: Representation of the plume geometry. r = ratio, h = thickness, E = saturation, between Lower Paskapoo (LP) and Edmonton (ED).

The disk is located between Edmonton (ED) and Lower Paskapoo (LP) formations having: a thickness: $h = 35$ m, porosity $\phi = 9\%$ and a CO_2 density under the LP conditions ρ (CO_2) = 340 kg/m³. The efficiency would be considered as the saturation of CO_2. The size of the plume was estimated for 20% CO_2 saturation, E=0.20. Using equation 4.2, the calculated volume is:

$$V_{LP-ED} = \frac{3,000,000 \text{ kg}}{340 \text{ kg/m}^3}$$

$$V_{LP-ED} = 8,823.53 \text{ m}^3$$

From equation 4.4, it is possible to calculate now the radius of the disk:

$$r_1 = \sqrt{\frac{V_{LP-ED}}{h\phi E_{20\%}\pi}}$$

$$r_1 = \sqrt{\frac{8,823.53 m^3}{1.978 m}} = 66.79 \text{ m}$$

giving as a result of approximately 67 m. The diameter would be approximately 140m and, as previously mentioned, this represents the base and top of the rectangular plume in the 2D model.

4.4 Post CO_2 injection

After the injection of CO_2 the described plume is expected to fill a space in the sandstone target, to an efficiency factor E. As a result, the same geological model will be utilized but including, in the case of the 2D model, a rectangular plume. To introduce this plume, two new interfaces were added (Figure 4-3) These interfaces combined with the top and base of the target zone, represent the rectangular block. The block corresponding to Lower Paskapoo was divided in three intervals. Blocks 1 and 3 (Figure 4-3) have the same property values corresponding with 0% CO_2 saturation. Block 2 is the injection zone, with density and velocity values obtained from Gassmann fluid substitution.
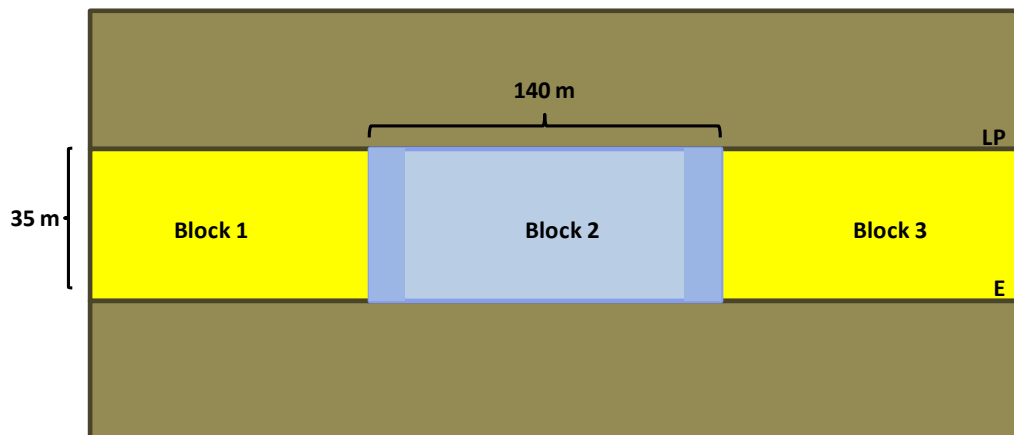
Figure 4-3: CO_2 plume inserted in the 2D model. Block 1 and 3 present the 0% CO_2 saturation properties and Block 2 is the CO_2 plume.

The properties inside the injection zone will depend on CO_2 saturation. In this case, six (6) scenarios were modelled: 0%, 20%, 40%, 60%, 80% and 100% CO_2 saturation, changing parameters for each saturation stage. Table 4-2 list the properties that the plume will have depending on the saturation level.

Table 4-2. Density and P-wave values in the target zone depending on the CO_2 saturation.

CO_2 Saturation	Bulk density (kg/m^3)	V_p (m/s)
0	2505	4189
0.2	2493	3891
0.4	2482	3895
0.6	2470.	3902
0.8	2459	3911
1	2447	3919

4.5 2D Seismic Modelling

Once the geological model was generated, a 2D seismic survey was designed. The purpose of this model is to represent a regional seismic scenario that includes the dipping layers, therefore an 8km long 2D line was designed (Figure 4-4). The receivers are located every 10 m and the shot points every 40 m. Norsar2D ray tracing tool was used in order to obtain the reflectivity events which are based on Zoeppritz equations. There were 120 receivers per shot, with a spread of 60 each side of the shot. Finally six different models for the different CO_2 saturation levels (0%, 20%, 40%, 60%, 80% and 100%) were generated using this survey geometry.

Once the shot simulation was finished, it was possible to generate synthetic seismograms, having as inputs the seismic events that resulted from the raytracing and a selected wavelet which is a zero phase Ricker wavelet with frequency 70 Hz. That selection was explained in Chapter 3 as a reasonable frequency needed to resolve the target. The final result was a series of six sequences of shot gathers (0%, 20%, 40%, 60%, 80% and 100% CO_2) in SEG-Y format. Figure: 4-5 is an example of a shot gather for 100% CO_2 saturation. It is possible to identify the eighteen interfaces.

Distance (km)
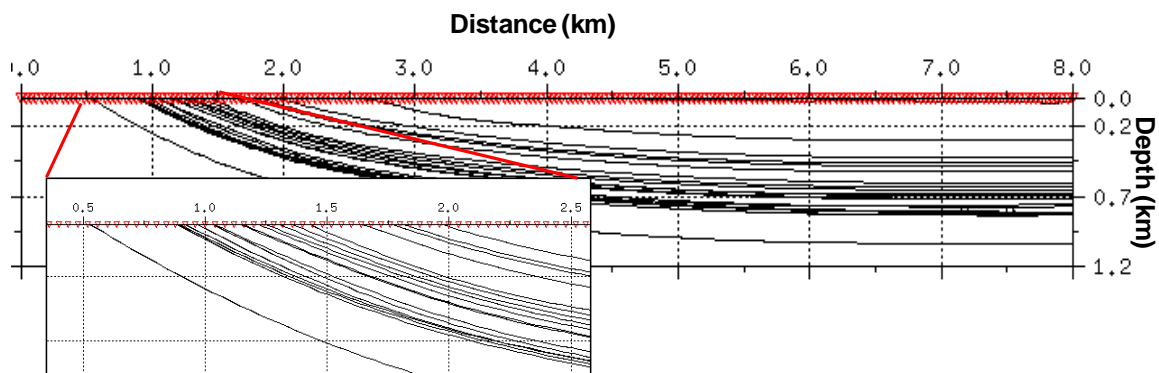
Figure 4-4: 8 km long geological model. Receivers were located at every 10 m, shots at every 80 m and 120 channels per shot.
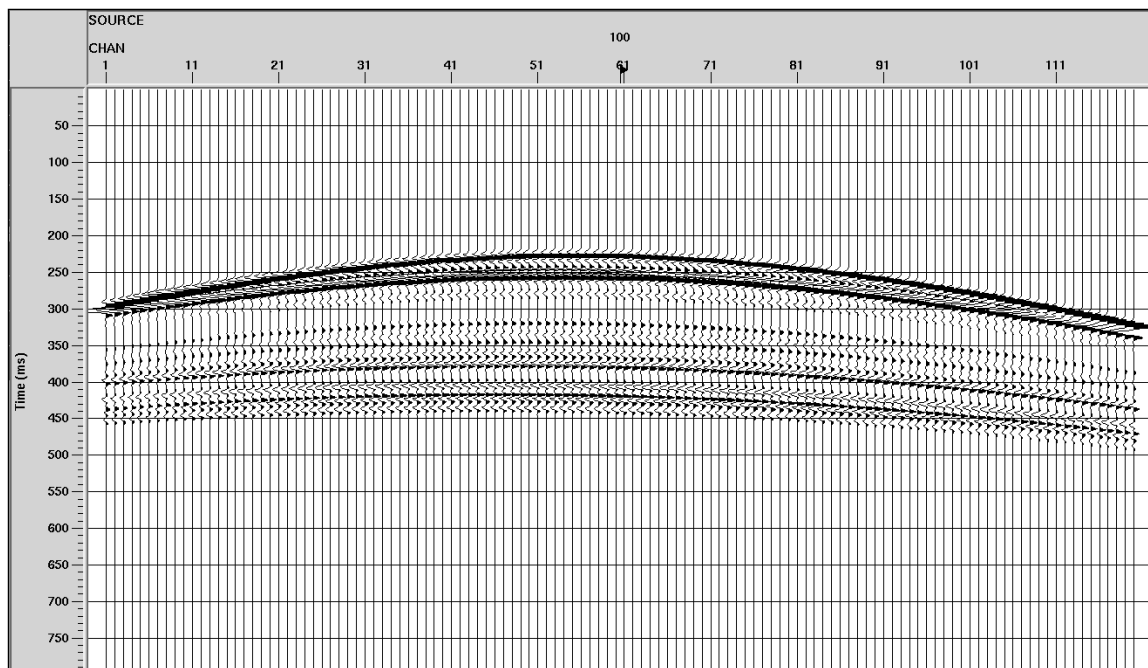
Figure: 4-5: 2D Shot gather from shot number 100, 120 channel spread.

4.6 Data Processing

The resulting seismic file was imported into Promax used for processing through to a CDP stack section.   In Chapter 2, the basic processing of field data was explained. In this case the data is modeled therefore the processing flow is much simpler, especially

given an ideal model without noise or statics effect. The first step is the 2D geometry assignment having the Norsar2D generated SEG-Y as input.

Given the presence of an ideal case, the next step is the velocity analysis, without need of static correction and noise attenuation. The geological model is already known and the velocity values established for each layer. The velocity model was created using "Interactive Velocity Editor", as shown in Figure 4-6 which follows similar principles as the geological modelling in Norsar2D. The velocity model with the approximate same interfaces as the geological model, was reproduced, and assigning the corresponding P-wave velocity values to the blocks. The velocity values are interval velocities, which were then converted into RMS velocity (V_{RMS}) and utilized for NMO correction. The interval velocity for a layer n (V_n) can be expressed through Dix's equation (Dix, 1955):

$$V^2{}_n = \frac{v^2{}_{RMS_n} t(0)_n - v^2{}_{RMS_{n-1}} t(0)_{n-1}}{t(0)_n - t(0)_{n-1}} \tag{4.5}$$

where $t(0)$ is the zero-offset travel time to the *nth* layer. *Vn* can be converted to V_{RMS} by:

$$V_{RMSn}{}^2 = \frac{\sum_i^N v^2{}_i \Delta t_i}{\sum_{i=1}^N \Delta t_i} \tag{4.6}$$

where Δt_i is the 2-way travel time of *ith* layer.
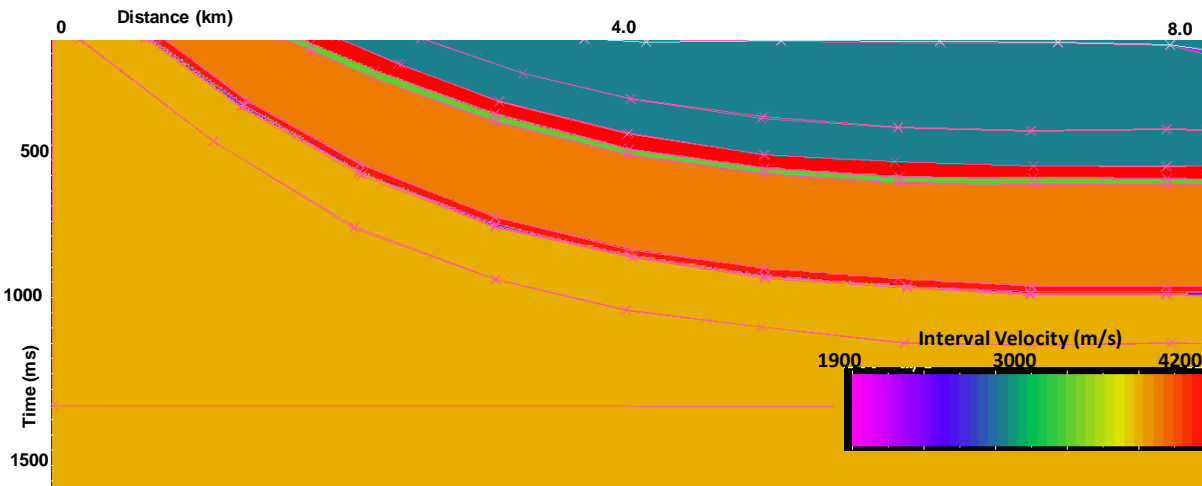
Figure 4-6: P-wave velocity model constructed in Promax velocity editor.

After the application of the NMO correction, the CDP stack function was applied in order generate the stack section. The CDP stack sections for the 0% and 100% CO_2 saturation cases are shown in Figure 4-7. Figure (a) shows the baseline CDP stack which has the same characteristics than the geological model showed in Figure 4-1. Figure (b) is the 100% CO_2 saturation scenario and presents the exact same characteristics, but including the injection zone, evident in the seismic section due to the time shift of the reflections in the target zone and bellow it (red square).

4.7 Monitoring Results

The changes in physical properties, such as velocity, reflectivity and time shift, caused by the injection of CO_2 in a sandstone aquifer were evaluated in Chapter 3 using a Gassmann approach and Shuey`s AVO analysis. In this chapter, I attempted to recreate the geology in the area and simulate the seismic response in order to examine changes produced by CO_2 injection. Figure 4-7 shows the monitor CDP stack section compared with the baseline for the 100% CO_2 saturation case. It is possible to see the injection zone and time shift. The effect of the CO_2 injection can be determined by subtracting the monitor CDP stack sections from the baseline section (0% CO_2). Figure 4-8 shows the difference between the 0% CO_2 section and the 100% CO_2 section. As expected, the rest of the traces outside the area of interest were cancelled whereas the injection region and reflectors underneath it are highlighted due to the difference in amplitude and travel time.

Distance (km)

a)

Distance (km)
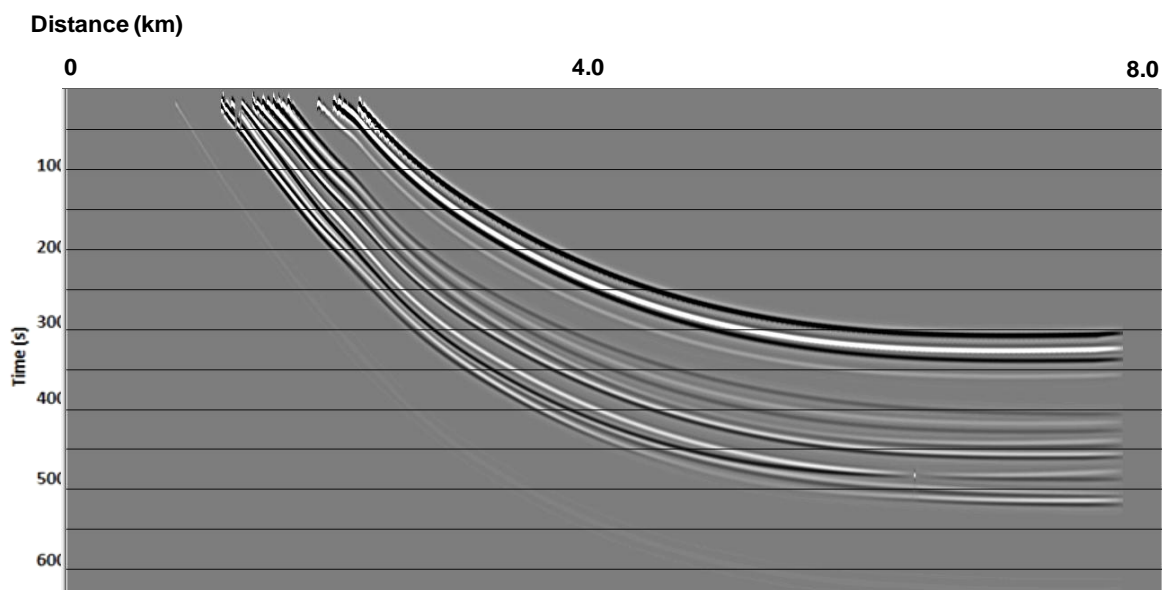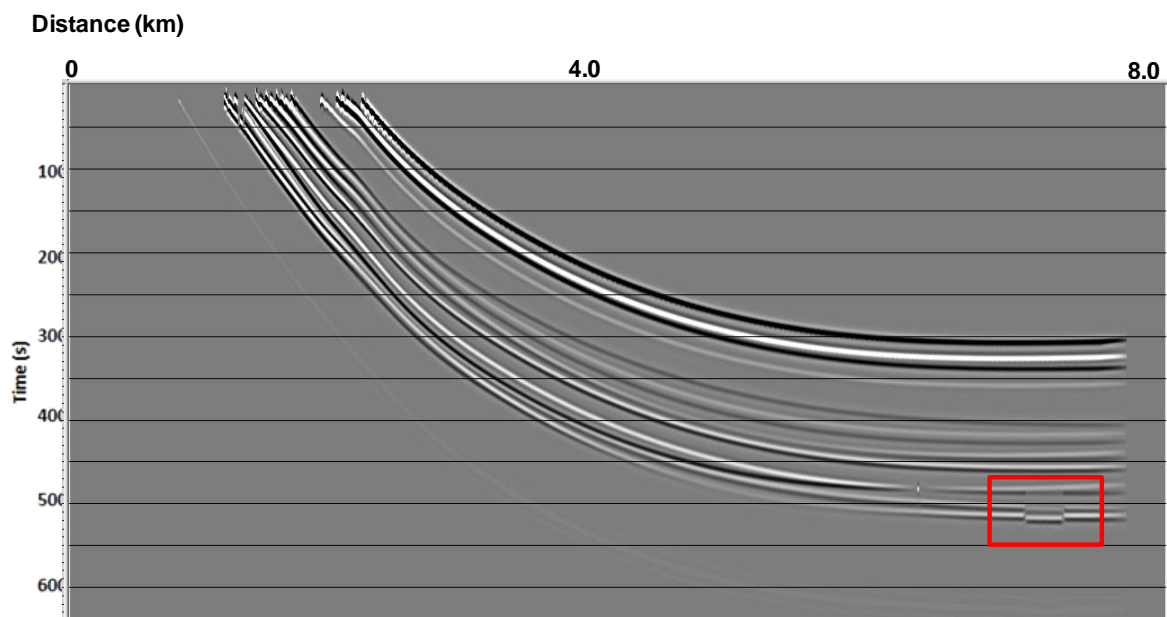
b)

Figure 4-7: a) Baseline CDP stack section. b) Monitor CDP stack section, post-injection with 100% CO$_2$ saturation (Injection zone in the red square).
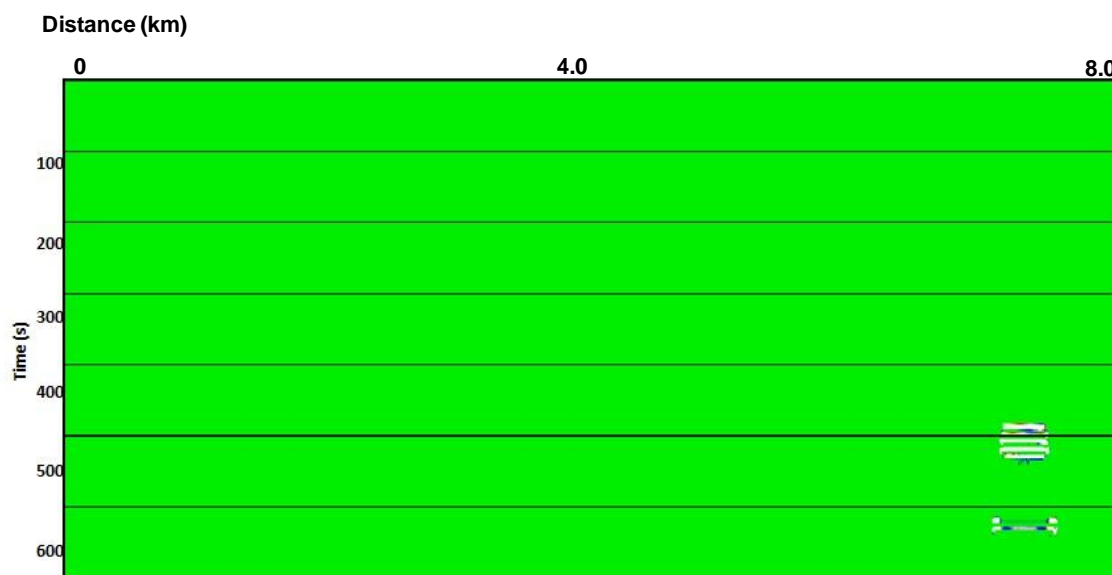
Figure 4-8: Residual 2D CDP stack section resulting from the difference between the 0% CO_2 section and the 100% CO_2 section.

In Chapter 3 it was found that the injection of CO_2 resulted in a P-wave velocity decrease of approximately 8% and a time delay of 1.2 ms. These same effects are observed in the seismic sections given the decrease in velocity, the travel time at the base of the injection zone will increase. This push-down effect also increases the travel time of the lower reflectors. On the other hand, increasing CO_2 saturation reduces the contrast between the overlaying layer and the target zone giving a decrease in reflectivity that combined with the time delay produce the differences on the seismic section seen in Figure 4-8.

In addition, AVO analysis, explained in Chapter 3, was undertaken. The seismic amplitude of the top reflector in the target zone was estimated from the CDP sections. These values were compared with the 0% CO_2 saturation case and the relative changes were calculated, having as 100% amplitude the baseline scenario. Table 4-3 shows the relative values for amplitude decrease with the increment of CO_2 saturation in comparison with the values obtained for the zero reflectivity, calculated in Chapter 3. From Shuey's results, it has been shown that AVO analysis, specifically, the calculation of Shuey's parameters and P-wave reflectivity, are very sensitive elements to measure the

changes in CO_2 saturation. The average change of the zero offset reflectivity is approximately 25 %. From the CDP stack, the comparative amplitude decreases an average value of 40%, specifically 36% reduction from 0% to 20% CO_2 saturation without any major changes in the other stages. The gradient *B* present less change and, as it was mentioned earlier, its trend is similar to the P-wave velocity, starts to slightly increase after 20% CO_2 saturation.

Figure 4-9 shows both, the zero offset calculation (red line) and the measured amplitude from the CDP stack sections (blue line) vs. CO_2 saturation. Both graphs present the same trend with about 10% difference (10% less change in the theoretical calculations). The amplitude has a considerable decrease from 0% to 20% CO_2 saturation, with slight decrease for the next stages (approximated 2% between each stage).Therefore, it is possible to measure from the amplitude change the presence of CO_2, but it is not possible to establish the exact saturation stage at this point of the study.

Table 4-3: Relative amplitude values measured from CDP stack sections with different CO_2 saturation conditions, compared with the relative zero offset amplitude *A* and the gradient *B* calculated from Shuey's equation.

CO_2 Saturation	Amplitude change in seismic (%)	A (R_o) from Shuey's (%)	B (gradient) from Shuey's (%)
0	100	100	100
20	64	74.24	84.96
40	62	73.03	85.22
60	61	72.1	85.65
80	60	71.23	86.12
100	57	70.39	86.62
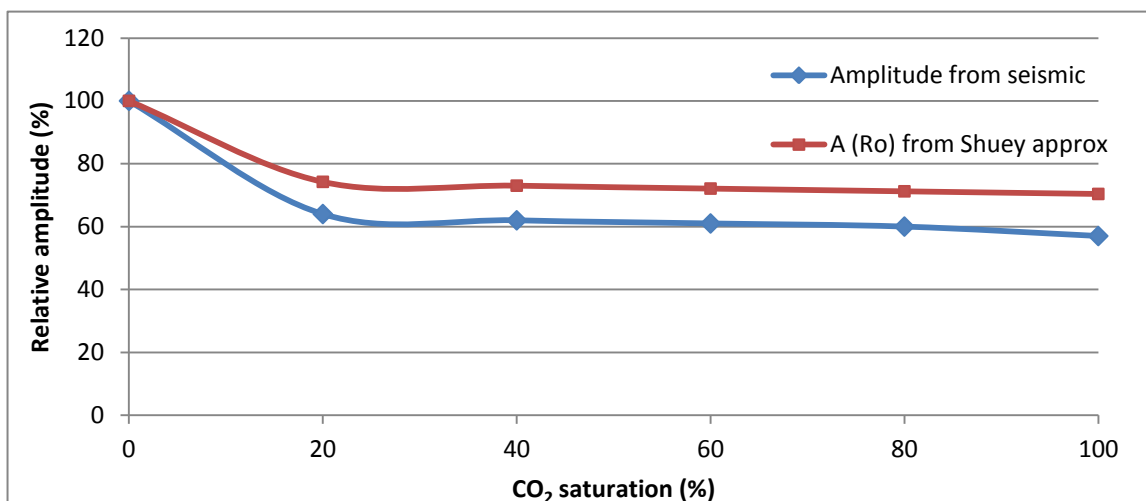
Figure 4-9: Relative change of the amplitude with CO_2 saturation: the blue line measured from CDP stack section and red line is the *A* parameter calculated from Shuey approximation.

4.8 Discussion

The 2D seismic modelling allows us to reproduce the conditions in the region of interest and the seismic changes during the different stages of CO_2 injection. The local geological model was based on the seismic analysis discussed in Chapter 2. In this case, an 8 km long 2D section attempts to characterize the structural scenario from the injection zone to the eastern flank of the Rocky Mountains Foothills. The post-injection seismic model shows a time delay of the basal reservoir reflector and amplitude reduction of the top reflector, with respect to the baseline. The changes are more evident after performing the difference between sections. The amplitude reduction measured from CDP stack sections and from Shuey's theoretical calculations at different CO_2 saturation values, showed a P-wave reflectivity reduction of approximated 30% to 40% from 0% to 20% CO_2 saturation, but not much variation for the other phase. Finally it is not possible at this stage of the study to establish any conclusion or correlation from the reflectivity values observed in seismic and a specific CO_2 saturation value.

Chapter Five: 3D Seismic Modelling

5.1 Introduction

The purpose of this chapter is to create a 3D reservoir and seismic model for examining the response to CO_2 injection. The model attempts to represent more accurately shallow geology, being based on the 2010 2D seismic line. The 3D survey would cover only the expected injection zone trying to give a reasonable simulation of the post-injection case.

5.2 3D Local Geological Modelling

5.2.1 Local Geological Model Design

A 3D geological model was generated using Norsar3D with the goal of producing a detailed representation of the injection zone using as a guide the geological and seismic data previously discussed. Chapters 2 and 4 describe the use of the seismic data, geological background and well information to design geological models. In this case, it is attempted to recreate the real injection zone. The result was a 2.5 km E-W (towards the foothills) and 1 km N-S 3D model. The generation of this model was based on the interpretation of the main horizons, shown in Figure 5-1: Middle Paskapoo A sand (MPA), Middle Paskapoo B sand (MPB), Lower Paskapoo sand (LP), Edmonton Group (E), Upper Detachment (UD), Lower Detachment (LD), Belly River (BR), Milk River (MR), Cardium (C) and Mississippian (M). In addition, a reference horizon named "Seal" was selected from the well logs as the next significant shale section on top of Lower Paskappoo in case of needing a secondary closure for the CO_2.

In this case, the horizons of the model were generated by creating grid maps. The grids were obtained from the interpreted horizons by using Kingdom Suite grid module and specifying the size of 2.5x1 km. In order to obtain a geological model it is necessary to convert the seismic data to depth. Moreover, the average velocity between each Formation was determined from the sonic log from well 12-33-21-2W5. Using these values, each of the time grids were multiplied by its corresponding average velocity. Finally the depth representation of each of the horizons was obtained. Figure 5-2 is one of

the map examples generated for the LP horizon. The combination of all the grids yielded the final 3D model shown in Figure 5-3. The grids where exported as ASCII files.

The grids were used as interfaces in the generation of the geological model. Figure 5-4 is the result from Model Builder module from Norsar3D, which was used in the seismic modelling. The density and P-wave velocity values of each of the layers were obtained from well information and are shown in Table 5-1. Layers 1, 2 and 3 were averaged in order to avoid the distorting effect of the low densities and low velocities of the first two layers.
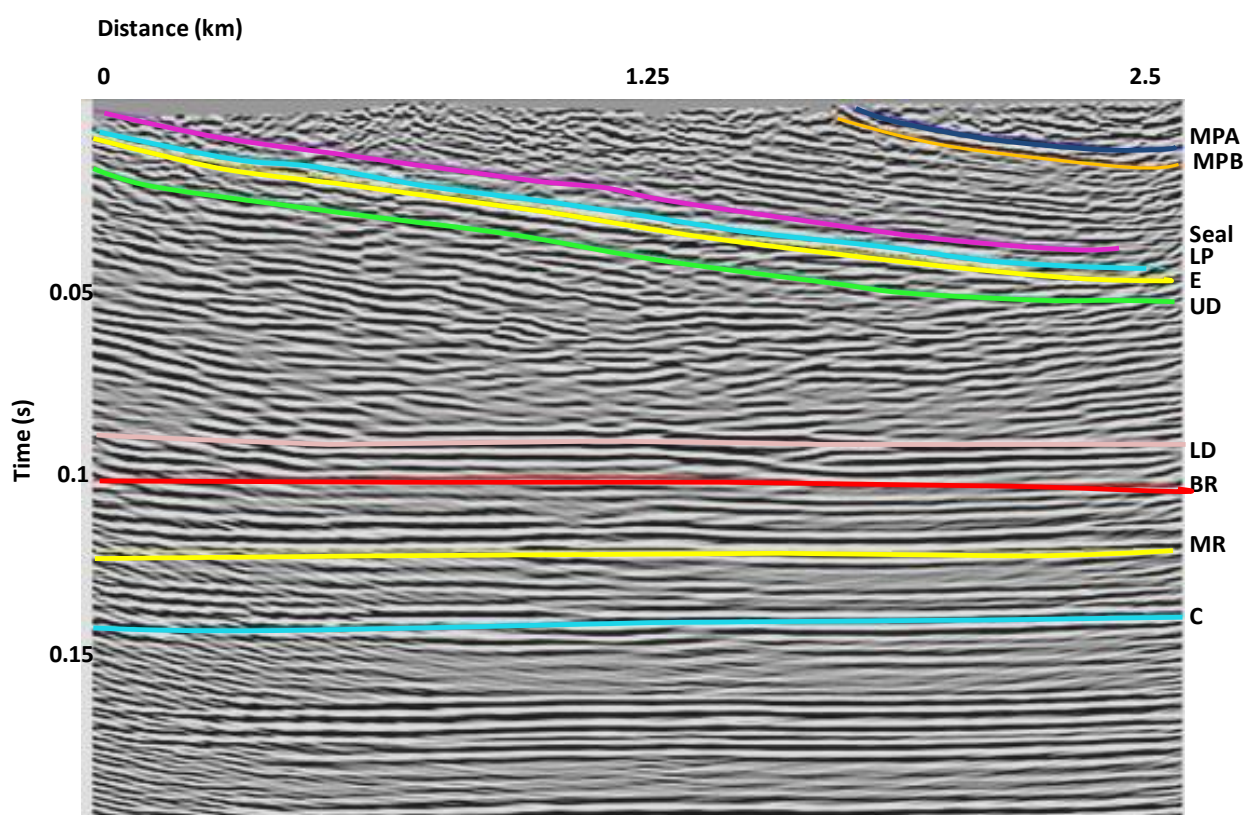
Figure 5-1: 2010 2D seismic section with the interpretation of: Middle Paskapoo A sand (MPA), Middle Paskapoo B sand (MPB), Seal, Lower Paskapoo sand (LP), Edmonton Group (E), Upper Detachment (UD), Lower Detachment (LD), Belly River (BR), Milk River (MR), Cardium (C).
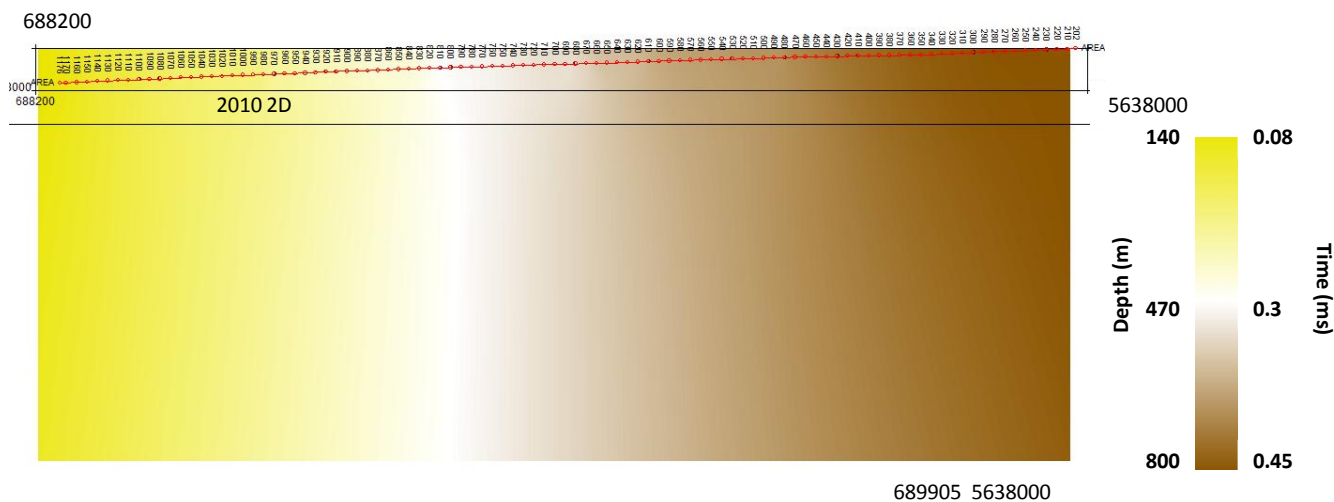
Figure 5-2: Grid map generated from the LP horizon. The scale is shown in depth and time. The red line in the upper side is the 2010 2D line.
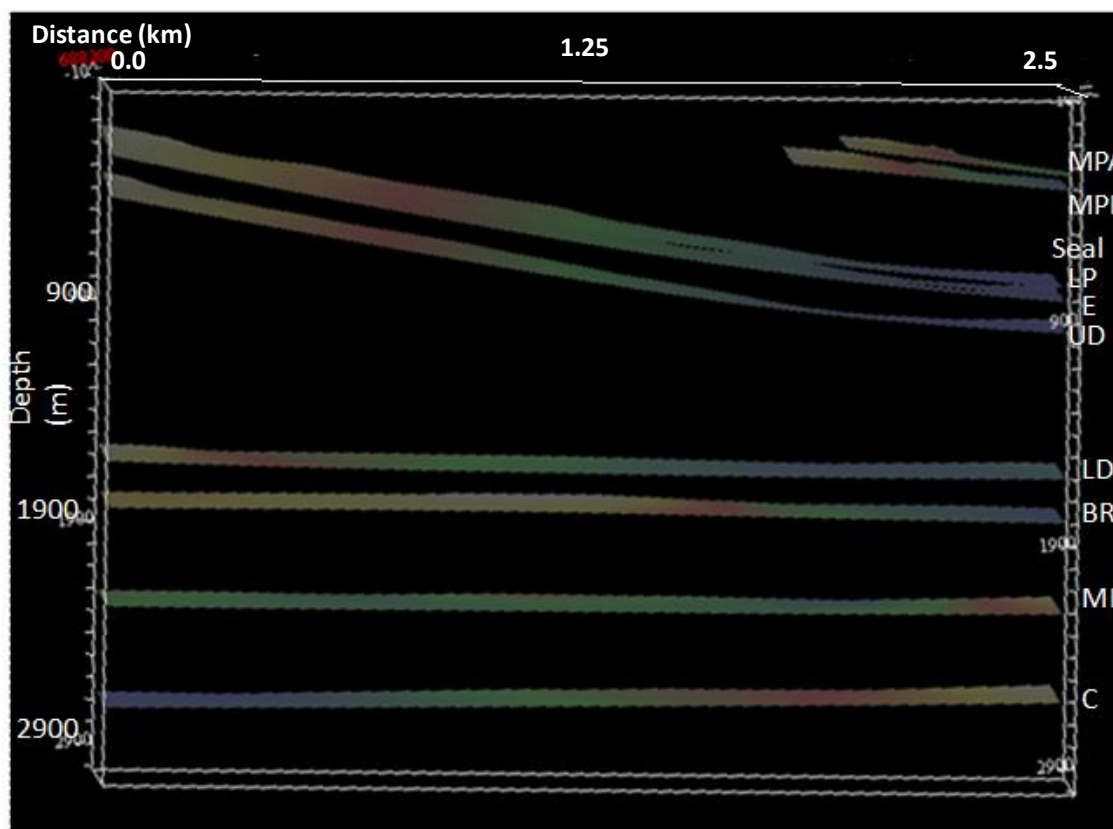
Figure 5-3: 3D view of the depth grids for ten horizons of the model.
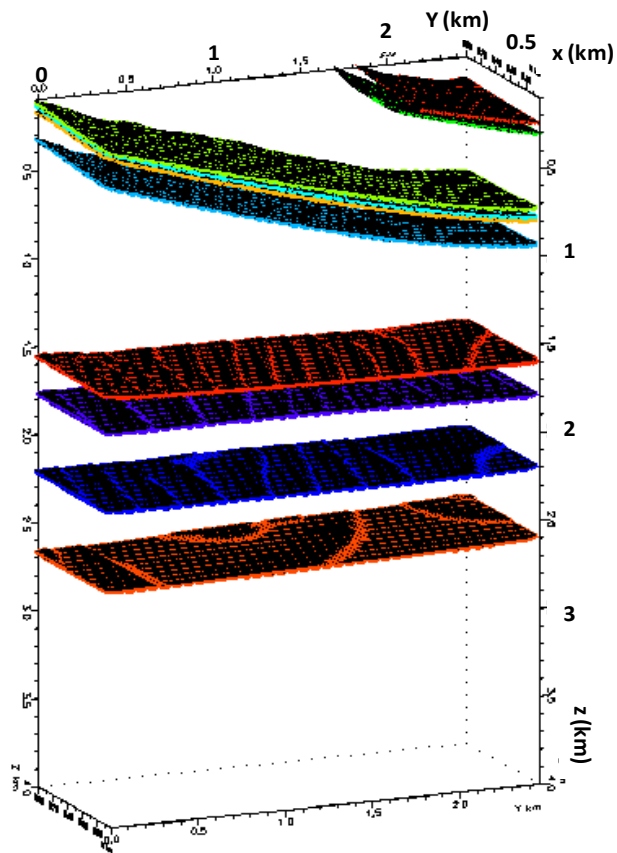
Figure 5-4: 3D model in Norsar3D obtained after importing the horizon grids.

Table 5-1: Density and P-wave velocity values for each of the layers in the model

Layer	Intervals	Density (kg/m³)	V_p (km/s)
1	Surface-MPA	2300	3.7
2	MPA-MPB	2300	3.7
3	MPB-Seal	2300	3.7
4	Seal-LP	2400	3.9
5	LP-ED	2500	4.1
6	ED-UD	2400	3.6
7	UD-LD	1700	3.3
8	LD-BR	2300	3.8
9	BR-MR	1900	4
10	MR-C	2000	4.2
11	C	2300	4.4

5.2.2 Reservoir Modelling

Schlumberger Carbon Service, on behalf of this project and thesis work, developed a reservoir modelling and monitoring simulation for the Priddis site making use of some of Schlumberger commercial software. This contribution gives an idea of the different scenarios of injection having specific injection amounts and its evolution in time. From the 3D geological model developed in this dissertation, Schlumberger Carbon Service created a reservoir simulation of the CO_2 plume and pressure plume using ECLIPSE. This reservoir model complements the models here proposed including factors such as dispersion in timeline and pressure change.

First, the geological model was developed in Petrel using the seismic data and the wells previously mentioned: 12-33-21-2W5, 10-22-21-2W5 and 2-33-021-2W5 (Chapter 1). The wells were extrapolated generating three pseudo wells as shown in Figure 5-5. The tops were correlated with seismic events making it possible to match the well information with the geological model. Figure 5-6 is the seismic volume utilized with the interpreted horizons. Using the well log information the volume shale, the total and effective porosity and the permeability relation from effective porosity and core data was estimated.

Figure 5-7 is the resulting Petrel geological model, extended over an area of 2.7x1.7 km and it is composed of 10x10 m grid blocks. The model of the area is 341m thick divided in 90 layers. According to this model, the injection zone, Basal Paskapoo, has a 30 m thickness and is located at the base. Once the Petrel geological modelling was created, the reservoir simulation was undertaken using Schlumberger Software ECLIPSE. The conditions taken into account, amongst others, are vertical layering; inclusion of drainage and inhibition processes as well a residual trapping and dissolution of the CO_2 into brine. The parameters applied were a ratio of vertical to horizontal permeability of 0.3; the reservoir is initially fully saturated with fresh water, temperature of 18˚C, initial pressure of 60 Bars at 600m and residual saturation of 25% water and 20% CO_2. Two main situations were evaluated: optimistic and pessimistic; the first represent a high permeability case were the CO_2 can be dissolved faster, in contrast with the second case of low permeability.

Three injection scenarios were evaluated: single injection of 600 tonnes over a several day period, shut-in 100 years, five annual injections of 600 tonnes over a several day period, shut-in 100 years and continuous injection of 20,000 tonnes per year for five years, shut-in 100 years (Senel et al., 2010). All these scenarios were evaluated for an optimistic and pessimistic case. The second scenario corresponds to the expected situation and was evaluated for this dissertation; therefore the example images showed here are related to this case. Figure 5-8 shows a plan view and east-west cross-section of the pessimistic model after 5 years of 600 tons/year injection, showing the presence of the CO_2 plume with a color variation given by the saturation change. The plume diameter is approximately 140 m with a height of 35 m. Figure 5-9 is the model after 100 years resulting in considerable dissolution of the CO_2 and a preferential migration towards the up-dip direction. In addition Figure 5-10 is the residual pressure diagram, presenting a maximum of 700 kPa. Figure 5-11 is the view of the optimistic scenario, presenting a diameter of 200 m (higher permeability). Moreover, there is a higher degree of CO_2 dissolution after 100 years of injection (Figure 5-12). The plume of pressure also reduces in magnitude as seen in Figure 5-13.
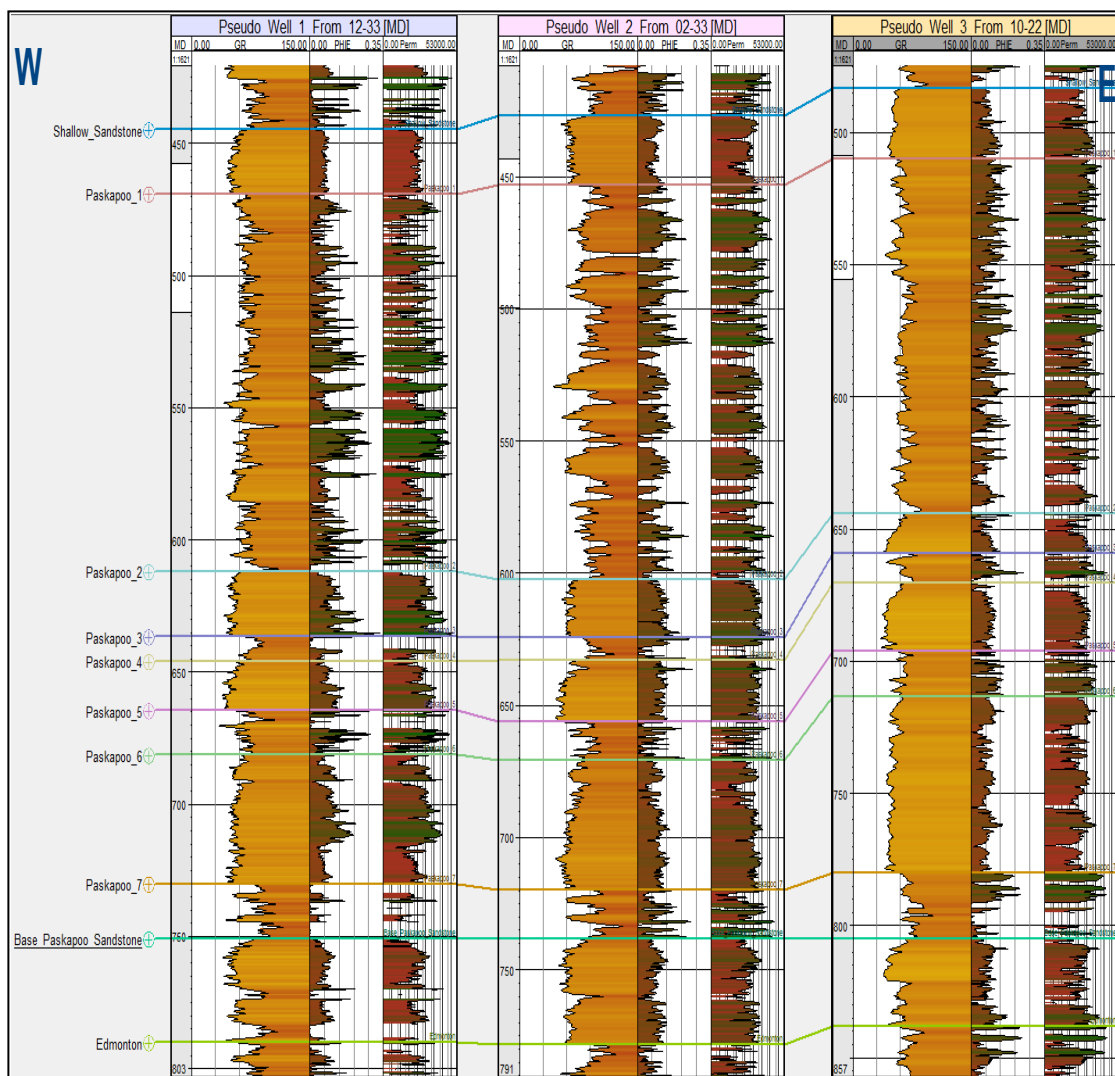
Figure 5-5: Pseudo wells generated from 12-33-21-2W5, 2-33-021-2W5 and 10-22-21-2W5 .
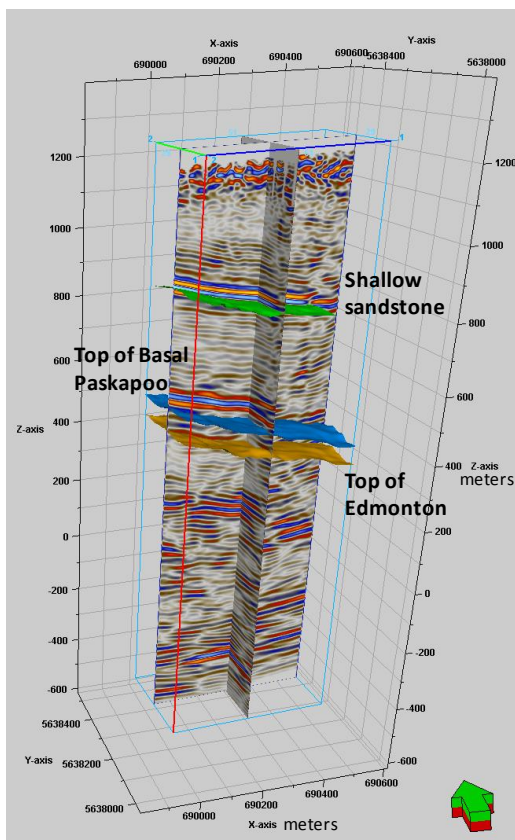
Figure 5-6: Interpreted horizons from seismic volume (Modified from Senel et al., 2010).
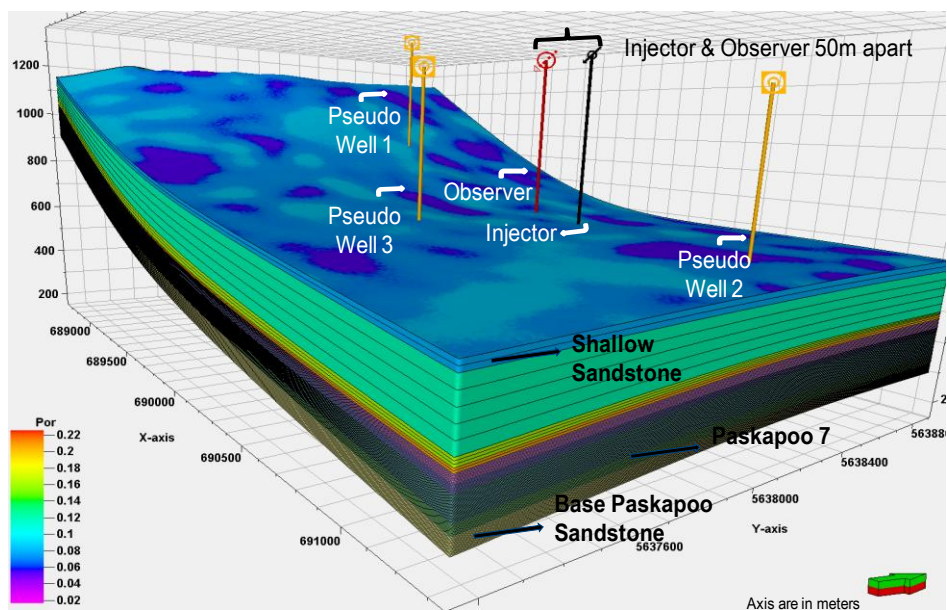
Figure 5-7: Static geological model showing locations of pseudowells and the injector and observation wells (Modified from Senel et al., 2010).

a)   b)
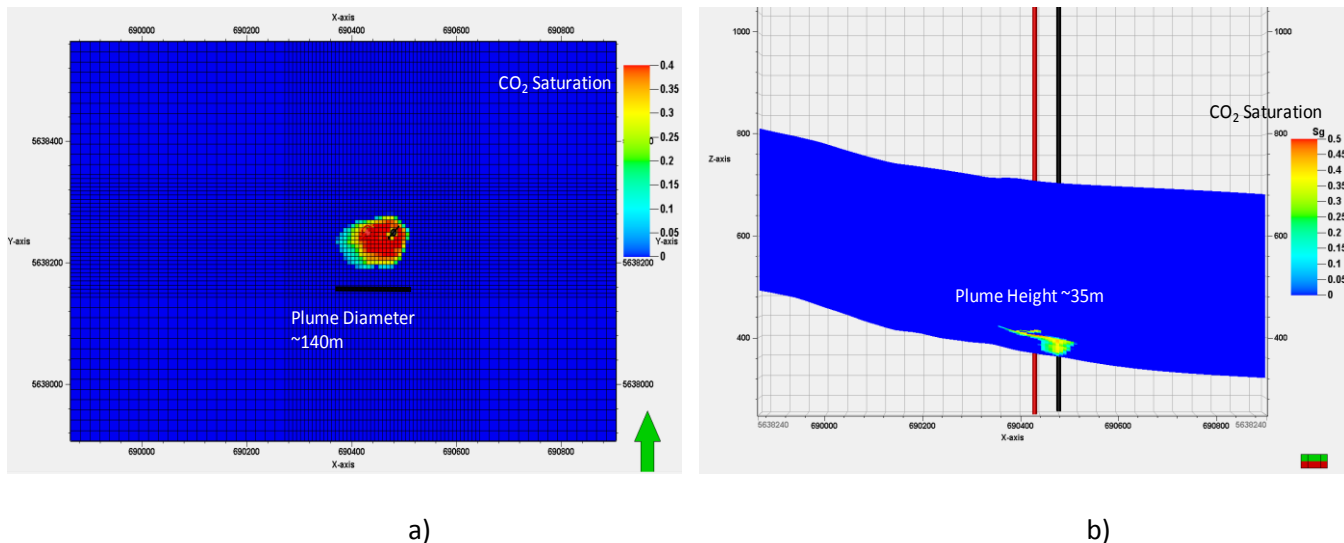
Figure 5-8: a) Plan view of CO_2 plume at top of Base Paskapoo finalized the injection of 3000 tones having the pessimistic scenario, showing a 140m diameter the plume. b) East-West slice view of CO_2 plume at the end of injection showing a height of 35m (Modified from Senel et al., 2010).

a)   b)
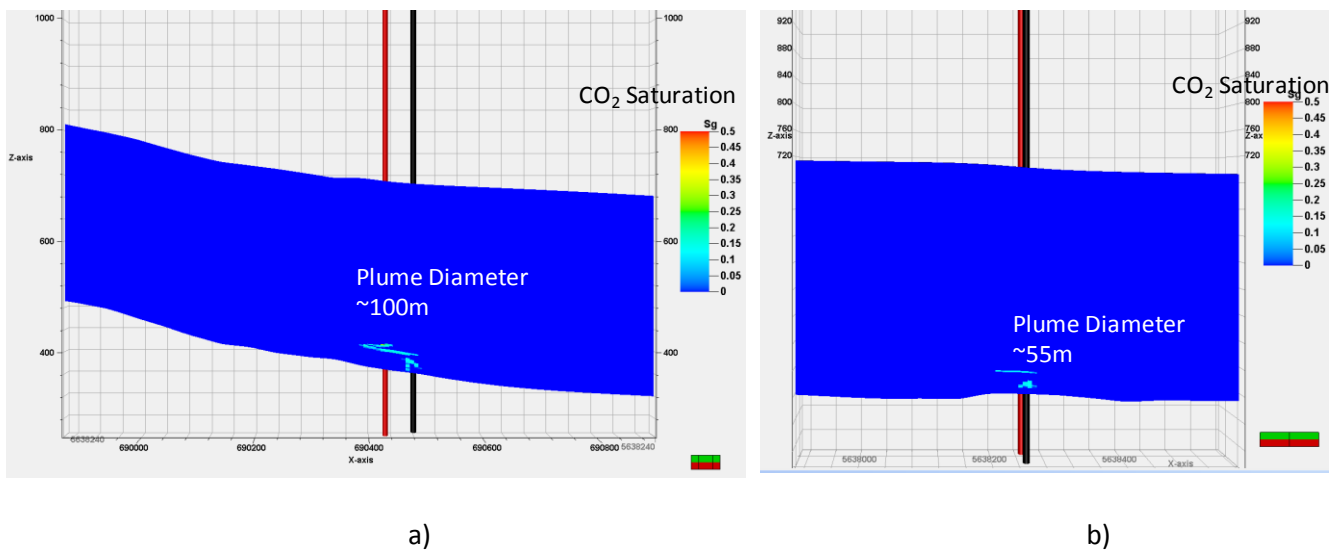
Figure 5-9. a) East-West slice view of the CO_2 plume and shut it in 100 years in the pessimistic case, showing 100 m diameter and up dip migration. b) South-North slice view of CO_2 plume at the end of injection (Modified from Senel et al., 2010).
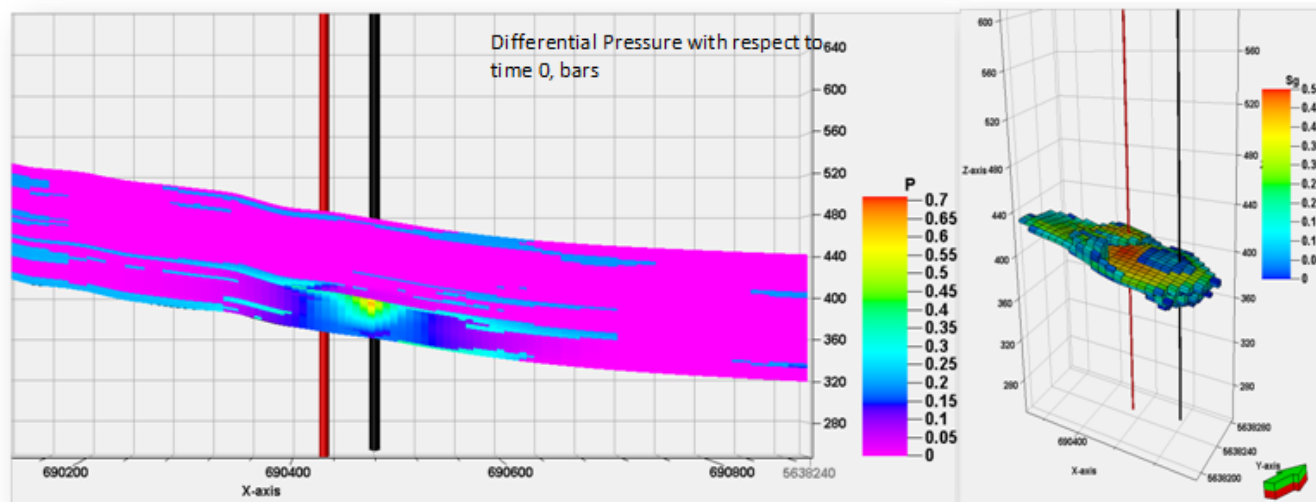
Figure 5-10: a) Pressure pulse generated due to the injection of 3000 tonnes of CO_2 and shut in for 100 years; pessimistic scenario. b) 3D Plume at the end of injection (Modified from Senel et al., 2010).
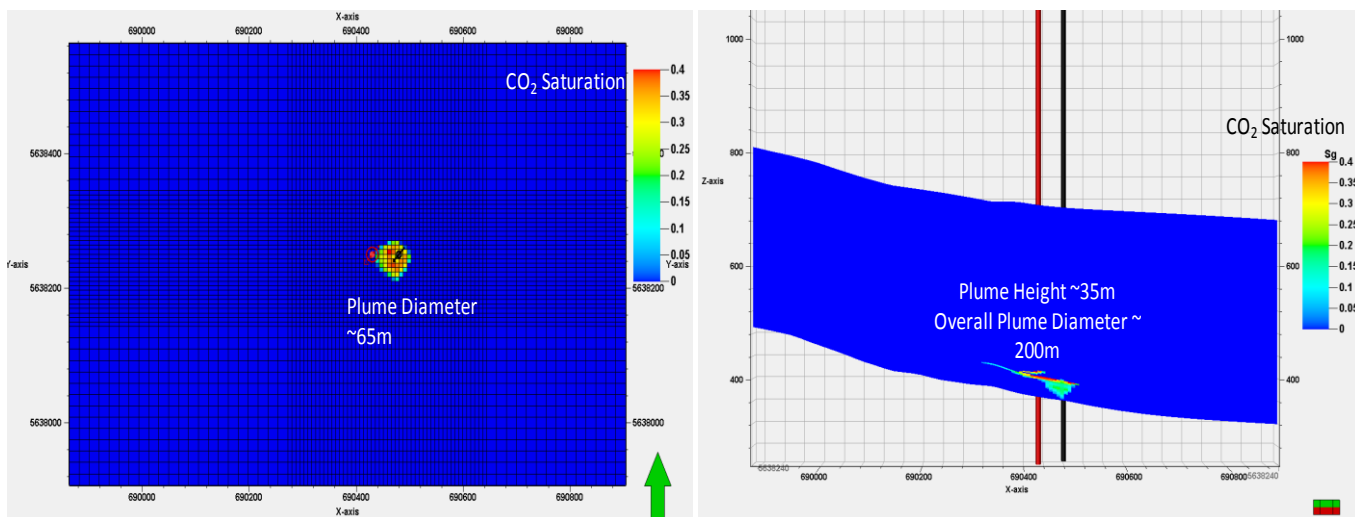
Figure 5-11: a) Plan view of CO_2 plume at top of Base Paskapoo finalized the injection of 3000 tones having the optimistic scenario, showing a 65m diameter the plume. b) East-West slice view of CO_2 plume at the end of injection showing a height of 35m (Modified from Senel et al., 2010).

a)   b)
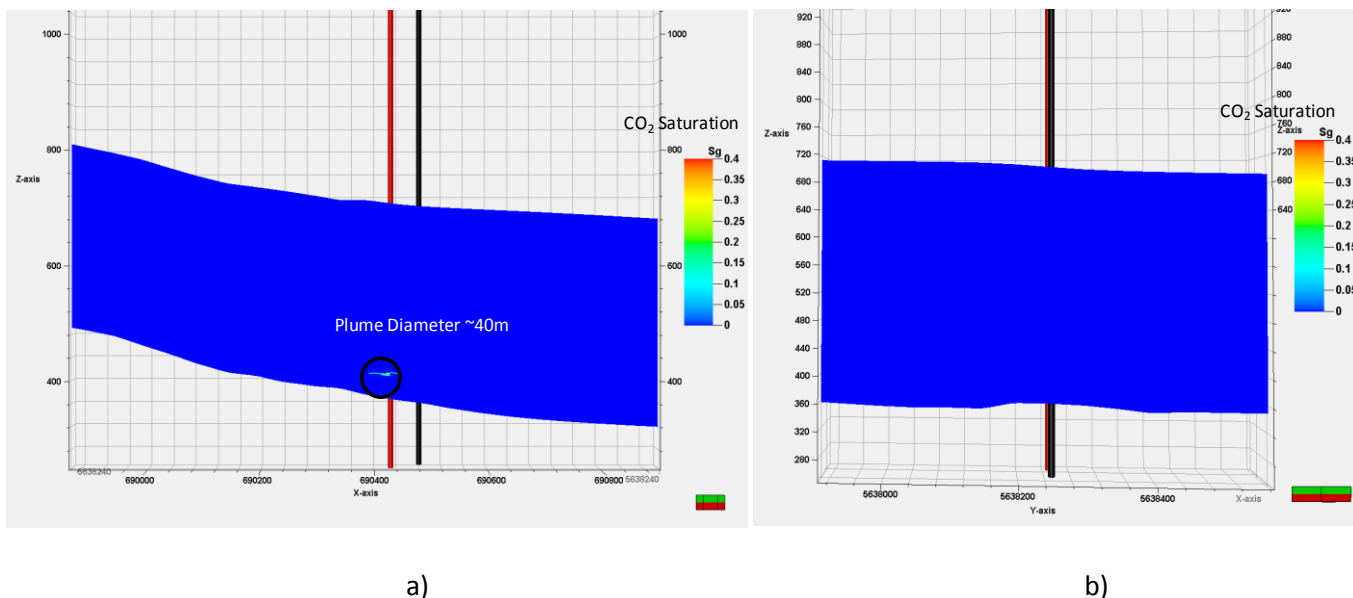
Figure 5-12: a) East-West slice view of the CO_2 plume and shut it in 100 years in the optimistic case, showing 40 m diameter and up dip migration. b) South-North slice view of CO_2 plume at the end of injection, there is no more plume dispersion and the dissolution from the point of view is almost complete (Modified from Senel et al., 2010).

a)   b)
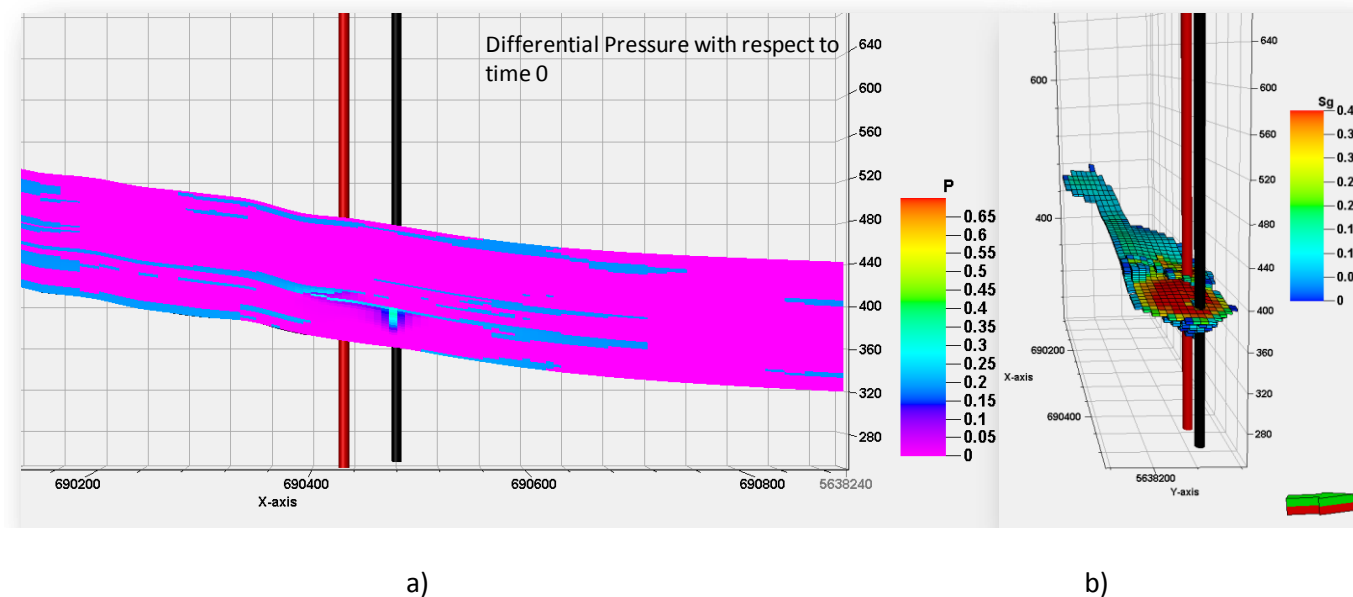
Figure 5-13: a) Pressure pulse generated due to the injection of 3000 tonnes of CO_2 and shut in for 100 years; optimistic scenario (Color scale with the pressure in bars). b) 3D Plume at the end of injection (Color scale with the CO_2 saturation) (Modified from Senel et al., 2010).

5.2.3 Simulated CO₂ plume for seismic modelling

For 3D seismic modelling, a simplified approach to calculating the plume size was undertaken; using the same methodology explained in Chapter 4 based on the volumetric method and the estimation of a cylindrical shape. Again, the simulated amount of CO_2 was 3000 tonnes, considered to be the maximum injected mass after 3 years of injection. In the 3D case it is possible create the disk shape. Furthermore, other complexities were added, including leakage through the LP seal into the next layer and the presence of a transition zone with lower saturation surrounding the main plume.

In this model, I assumed that 25% of the CO_2 would leak upwards into the overlaying formation. That next surface was selected from log information and it is 60 m above the LP. This is the only added interface that doesn't represent a formation top. Thus, the final model is: 75% of the total mass would remain trapped between the top of the Edmonton Fm. and the top of the Lower Paskapoo Fm., and the rest between Lower Paskapoo and the new "Seal" layer. Complementing this, it was also assumed that, in both cases (upper and lower cylinders), 90% of the CO_2 is contained at 50% saturation in the storage formation porous space, while 10% would be part of an outer disk with 2% saturation in an low efficiency annular transition zone. In total the model was composed of four disks, illustrated in Figure 5-14.
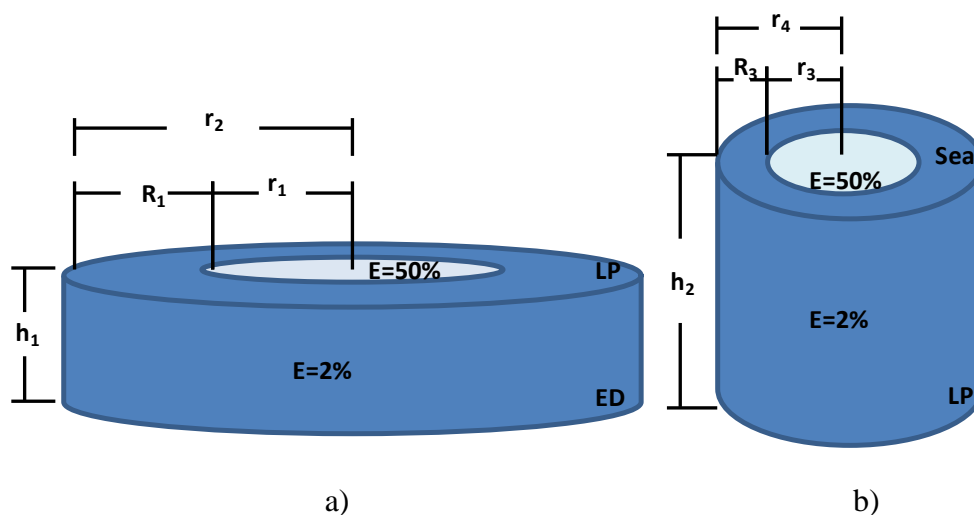
Figure 5-14: Representation of the plume geometry. (a) represents the plume injected between LP and ED and (b) represents the leaked 25% of the CO₂ injected and trapped between LP and the "Seal".

The first two disks were located between the Edmonton (ED) and Lower Paskapoo (LP) formations having: a thickness: $h = 35$ m, porosity $\phi = 9\%$ and a CO_2 density under the LP conditions $\rho = 340$ kg/m^3. The efficiency would be considered as the saturation of CO_2, $E = 50\%$ for inner disk and $E = 2\%$ for outer disk. Between the ED and LP tops, 2250 tonnes remained. The final volume in this first section obtained from equation 4.2 is:

$$V_{LP-ED} = \frac{2,250,000}{340} \, m^3$$

$$V_{LP-ED} = 6,617.64 \, m^3$$

90% of this volume remains in the first dispersion disk:

$$V_{r1} = 6,617.64 \, m^3 \text{x}0.9 = 5,955.87 m^3$$

and the other 10% would represent the outer disk with a volume of:

$$V_{R1} = 6,617.64 \, m^3 \text{x}0.01 = 661.76 m^3$$

This is possible to calculate the ratio of both disks using equation 4.4, first the inners disk "r_1", for which $E = 50\%$:

$$r_1 = \sqrt{\frac{V_{LP-ED}}{h\phi E\pi}}$$

$$r_1 = \sqrt{\frac{5955.87}{4.945}} \, m$$

giving as a result r_1=34.704 m or approximately 35 m. For the calculation of "r_2" we have that the volume of the outer disk will be given by:

$$V_{annulus}(R_1) = V_2(r_2) - V_1(r_1),$$

Therefore, the calculation of the ratio can be simplified in:

$$r_2{}^2 - r_1{}^2 = \frac{V_{LP-ED}}{h\phi E\pi}$$

$$r_2 = \sqrt{\frac{V_{LP-ED}}{h\phi E\pi} + r_1{}^2},$$

where $E = 2\%$, resulting in

$$r_2 = \sqrt{\frac{661.76}{0.1978} + 1225} \ \ \text{m},$$

with a final outer radio $r_2 = 67$ m or approximated 65 m, resulting in a $R_1 = 30$ m.

The same procedure was followed for the second two disks, located between top of the Lower Paskapoo Fm. and the overlaying seal layer having: thickness $h = 60$ m, porosity $\phi = 15\%$ and CO_2 density under the LP conditions $\rho = 323$ kg/m^3. Saturations were the same; $E = 50\%$ for inner disk and $E = 2\%$ for outer disk. This second group of disk contains 25% of the CO_2 resulting in 750 tonnes between LP and the Seal. The volume in this section is:

$$V = \frac{750{,}000}{323} \ \text{m}^3$$

$$V_{seal-LP} = 2{,}321.98 \ \text{m}^3$$

90% of this volume remains in the inner dispersion disk:

$$V_{r3} = 2.321{,}98 \ \text{m}^3 \text{x} 0.9 = 2{,}089.78 \text{m}^3$$

The other 10% would represent the outer annular disk with a volume of:

$$V_{R3} = 2.321{,}98 \text{m}^3 \text{x} 0.01 = 232.19 \text{m}^3$$

Having all this elements it is possible to calculate the ratio of both disks, first the inners disk "r_3":

$$r_3 = \sqrt{\frac{V_{seal-LP}}{h\phi E_{50\%}\pi}}$$

$$r_3 = \sqrt{\frac{2089.78}{4.5}}\ m$$

giving as a result $r_3 = 21.55$ m or approximated 22 m. Following the same process for the second disk, "r_4" is:

$$r_4 = \sqrt{\frac{V_{LP-ED}}{h\phi E\pi} + r_3{}^2}$$

$$r_4 = \sqrt{\frac{232.19}{0.5652} + 484}\ \ m,$$

with a final r_4 of 30m, resulting in $R_3 = 8$m.

5.2.4 Model after CO$_2$ injection

After defining the shape and size of the CO_2 plume it was possible to design it in Norsar3D and make it part of the geological model, representing the post-injection scenario. The same model previously explained was used and the CO_2 plume was created with a new set of interfaces that constitutes individual blocks with the respective velocity and density values obtained after applying Gassmann fluid substitution. Fluid substitution was performed over both lithological sections for a saturation of 50% and 2% CO_2 following the same procedure explained in Chapter 3. Table5-2 summarizes the parameters for each of the disks. These density and P-wave velocity values were added to the property selection in the post injection model. Figure 5-15 is a cross section with the different property blocks, where the different parts of the disk model are included. Figure 5-16 shows the final plume modeled in Norsar3D; the cylinder walls represent the interfaces separating the changes in properties depending on the CO_2 saturation.

Table5-2: Density and P-wave velocity values for the different disks of the CO$_2$ plume.

Disk	Density (kg/m^3)	V$_p$ (km/s)
LP-ED inner (E=50%)	2480	3.89
LP-ED outer (E=2%)	2503	3.94
Seal-LP inner (E=50%)	2350	3.80
Seal-LP outer (E=2%)	2400	3.85
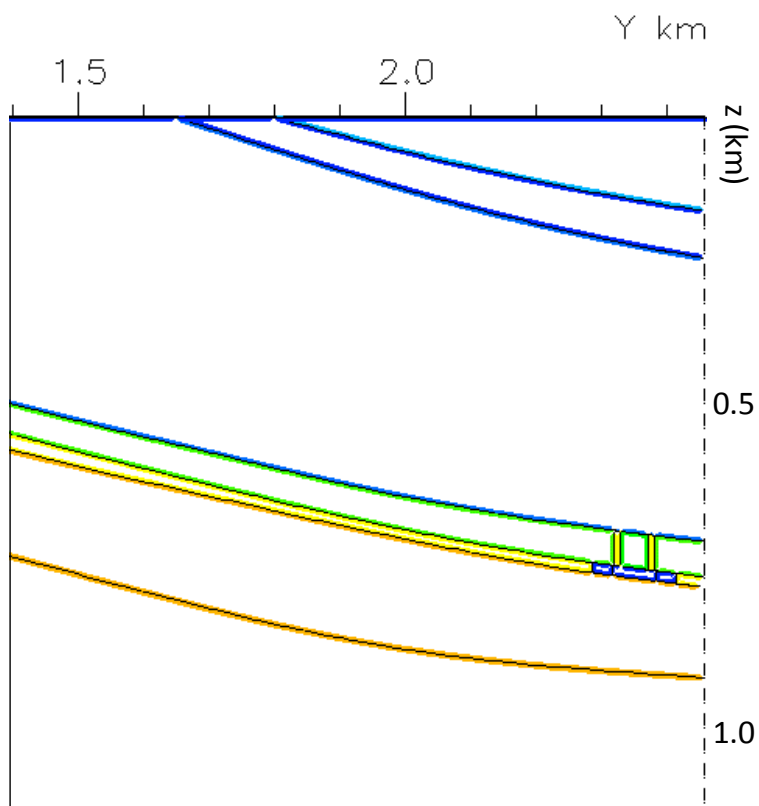
Figure 5-15: Cross section view of the model showing in color the different block limits. In this model it is possible to see the different components of the disk model.
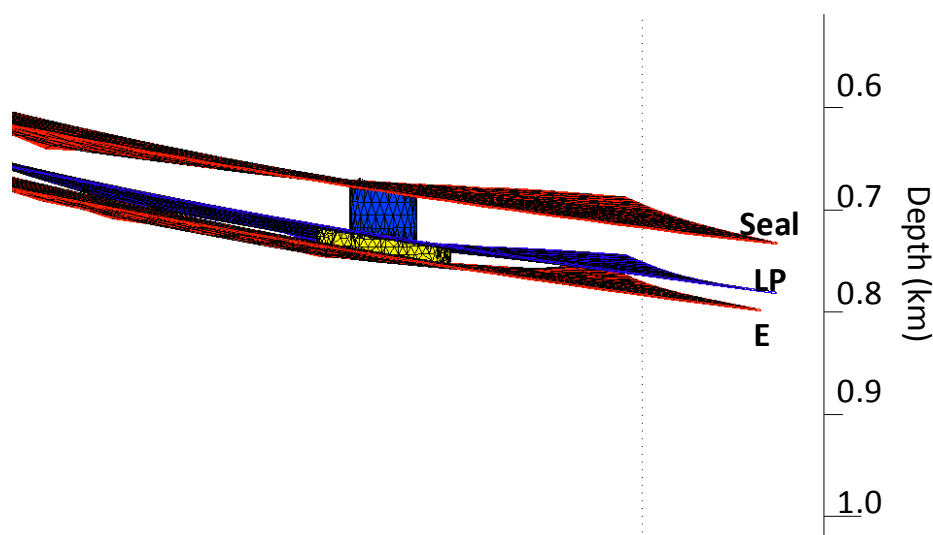
Figure 5-16: 3D view of the plume. The first cylinder is between Lower Paskapoo and Edmonton and the second between Seal and Lower Paskapoo.

5.2.5 3D Seismic Modelling

A seismic survey was designed to image the plume in the Paskapoo Fm. It is important to notice that even when the geological model extends about 2.5 km, the area of the survey will be 700x600 m simulating the acquisition for the CO_2 monitoring in the area of injection. The survey is composed of: seven receiver lines in an east-west direction and fifteen shot lines oriented north-south. The spacing between shot lines is 100 m and receiver lines 50 m, with shot points at every 20 m and geophones at every 10 m (Figure 5-17).

Having the model and seismic survey, Norsar's common shot wavefront tracer was used over the final model, as shown in Figure 5-18. Raytracing was undertaken for 480 shots having the total 511 receivers live for each shot. The same process was implemented over the initial model and repeated after injection and the resulting reflectivity events were used in the synthetic seismogram generation. The synthetic seismogram is the result of the convolution between the reflectivity series with a selected wavelet, in this case a zero-phase Ricker with 70 Hz dominant frequency, which enables the target zone to be resolved. The sample interval is 1 ms and record length is 2 sec.
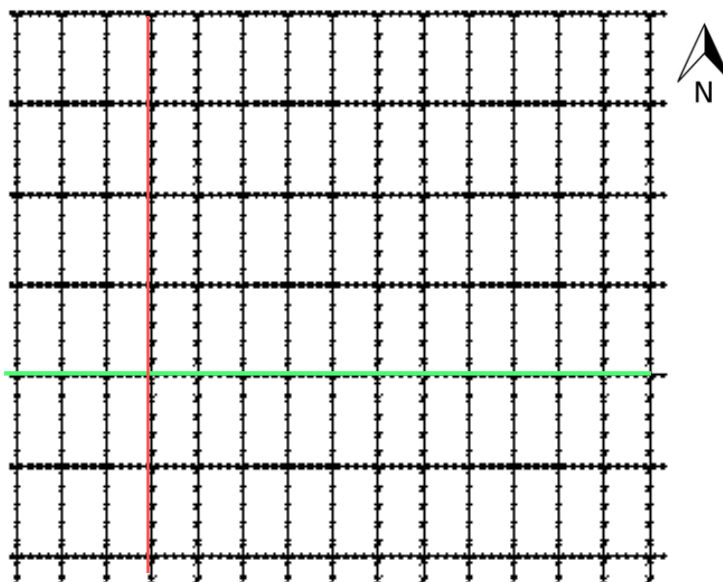
689905 5638000

Figure 5-17: The layout for the 3D seismic model. Receiver lines direction in green and shot lines are in red.
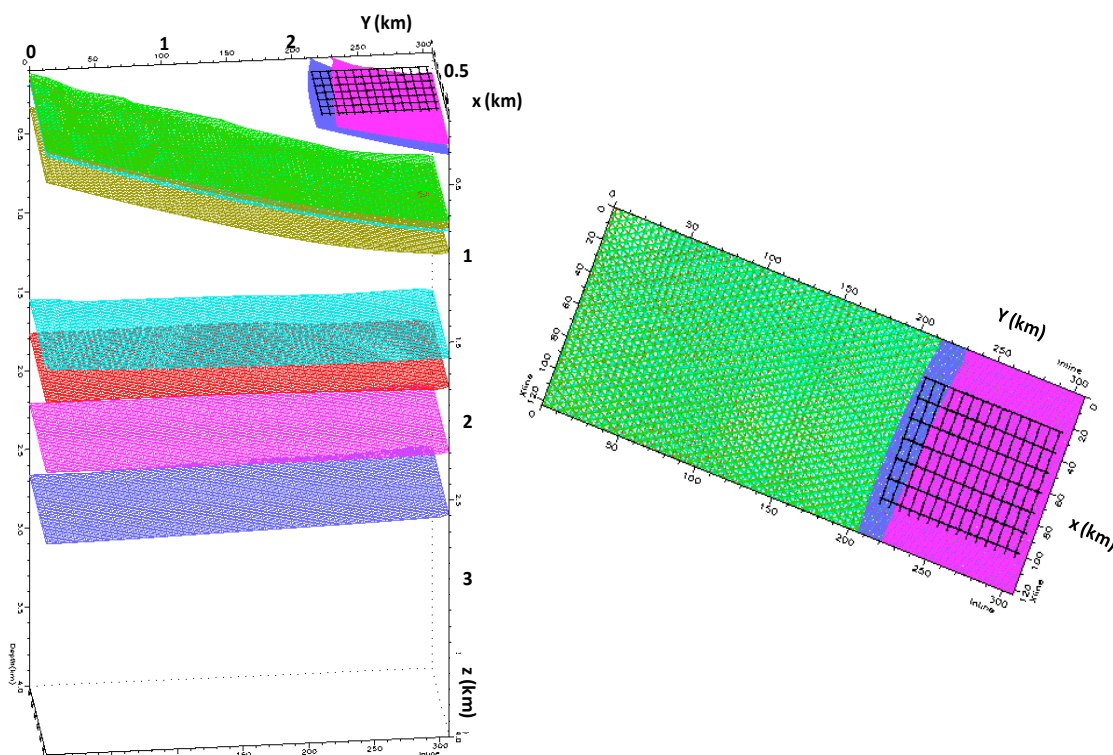
Figure 5-18: Geological model with the survey location.

5.2.6 Data Processing

The seismic file in SEG-Y format generated from Norsar3D was used as input data for the processing. Promax software was used following a basic flow. Figure 5-19 is an example shot gather showing the seven inlines with 73 receivers. It is possible to identify eight of ten reflectors from the model; the first two layers were not included in the modelling. The first step for processing is the 3D geometry assignment and binning of the data imported from Norsar3D. The distance between receivers is 10 m and between shots 20m, with CDP bins of 5x10m having an average fold of 60 and a maximum of 84, located in the center of the survey as shown in Figure 5-20.
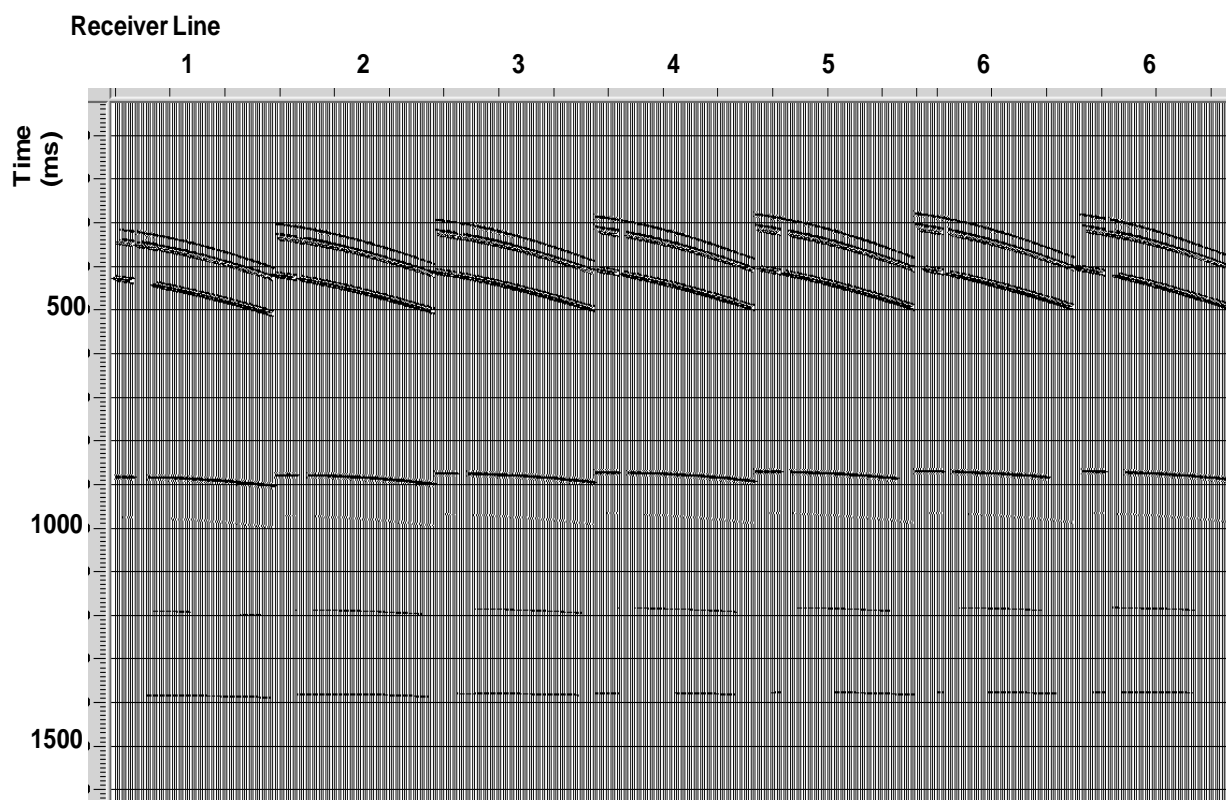
Figure 5-19: An example shot gather showing the seven receiver lines.
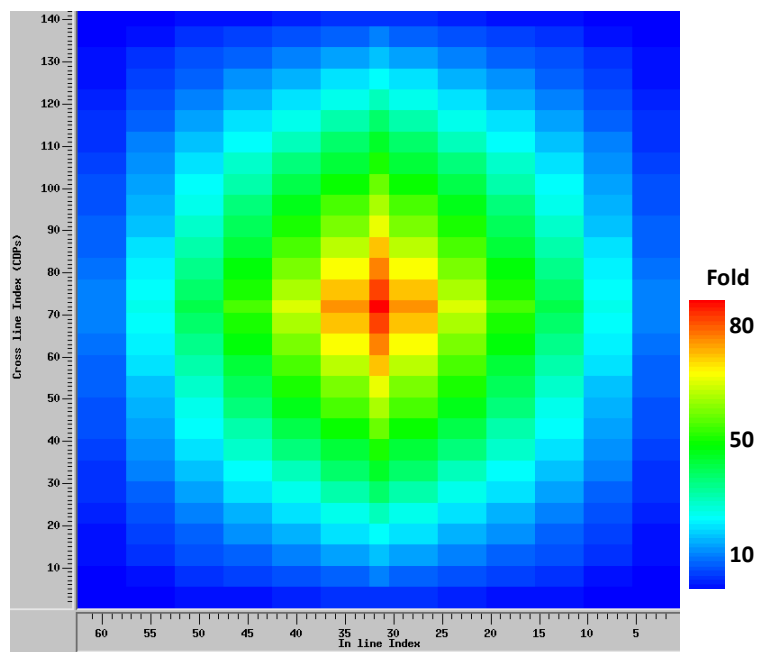
Figure 5-20: CDP fold of the 3D model

This model does not include topography, a weathering layer or noise, so it was not necessary to apply any static correction or noise attenuation. Consequently the next step was velocity analysis. In this case, the velocity and layer distribution it is already known. The velocity model was created in Norsar3D and imported into Promax. Based on the 3D geological model constructed in Model Builder, a P-wave velocity cube was generated and exported as a SEG-Y file. The velocity model from Norsar3D is shown in Figure 5-21 and was used for the processing of the volumes, before and after injection. Finally NMO was undertaken using the RMS velocity calculated from the interval velocity model. The CDP stack is shown in Figure 5-22, an example of the inline number 34 and crossline 130; the eight reflectors are dipping in the inline direction and flat in the crossline direction.
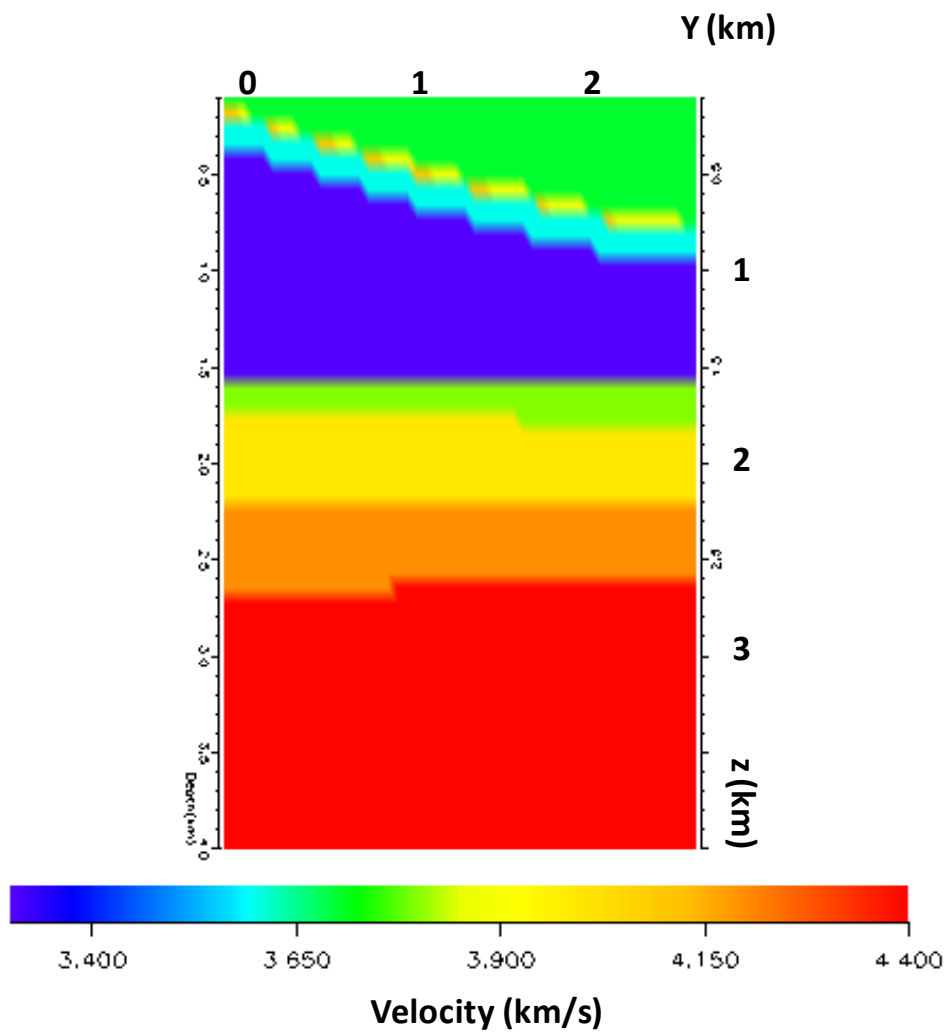
Figure 5-21: P-wave velocity cube obtained from Norsar3D.
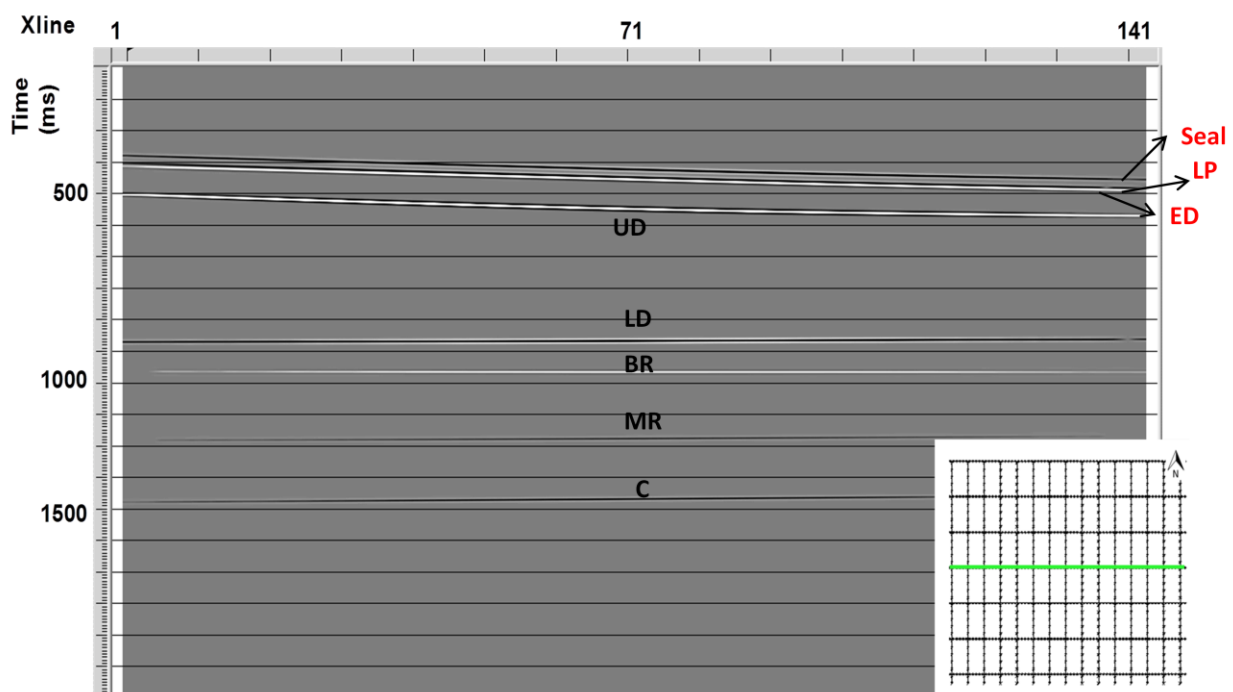
a)
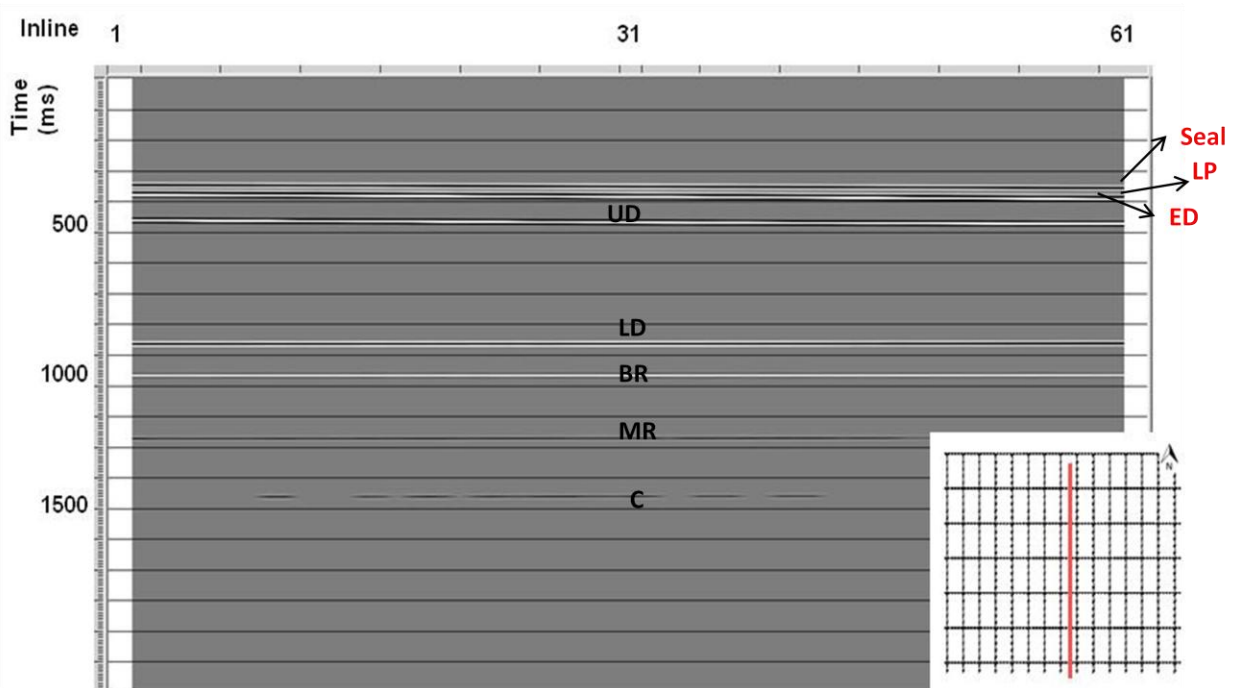
b)

Figure 5-22: CDP stack section, (a) inline (34) and (b) crossline (130) view.

5.3 Monitoring Results

The main objective of this study is to analyse the changes in seismic response after injecting CO_2 in Lower Paskapoo Fm. The goal was to recreate a realistic scenario in terms of geology and seismic imaging results. Two 3D seismic models were generated, one for an initial pre-injection case (baseline) and the second after 3000 tonnes of CO_2 injection (monitor). The simplest way to establish a difference and to monitor changes in the seismic image is by subtracting the post-injection volume from the baseline volume. The presence of the CO_2 plume causes a decrease in density and P-wave velocity; therefore the expected time lapse effect would be a change in the reflectivity values across the injection area and a time delay of the reservoir basal reflectors and horizons underneath it. This velocity push down will affect LP, ED, UD, MR, BR and C. In order to visualize the changes in seismic, inline, crossline and time slice perspectives were obtained by using Hampson-Russell "View 3D" and "Strata" applications.

The first interpretation approach was to evaluate the time delay from the CO_2 saturated CDP stack in comparison with the baseline survey. In order to do this, the LP and E reflectors were picked in the zone of interest in both volumes. Figure 5-23 illustrates the location of the crossline, the injection area, LP and E tops. Times for LP and E are approximately 380 ms and 392 ms respectively for pre injection scenario, with a time delay after injection of only 1ms. However, even this small delay is interpretable from the seismic data. Figure 5-24 shows a detailed view of the injection zone, for the baseline seismic and also for the monitor volume. From this comparison it is noticeable the reduction in amplitude from the baseline to monitor surveys.

In addition, I attempted to establish a relationship between seismic amplitude changes and the CO_2 saturation. In Chapter 4, I showed the application of Shuey's approximation in order to calculate the changes in reflectivity at different CO_2 saturations. In this case it measured the average amplitude of the top reflectors: Seal and LP. The expected tendency was found, which a reduction in reflectivity of approximately 50% in comparison with the baseline. In Chapter 4 it was found, by Shuey`s approximation and seismic modelling, that the amplitude will decrease about 30% to 40%.
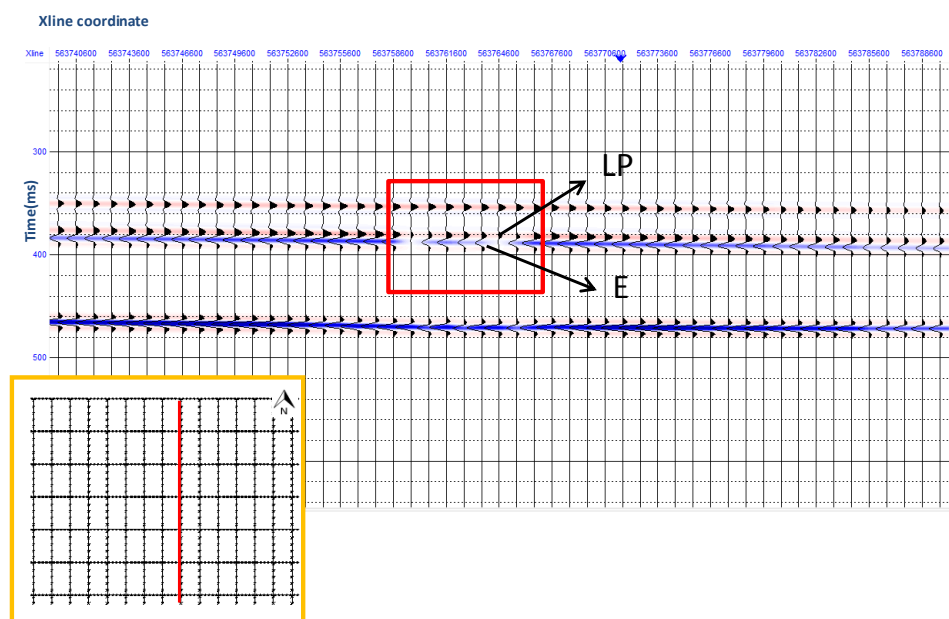
Figure 5-23: Crossline 140 showing the injection area in a red square, LP and E tops.

a)   b)
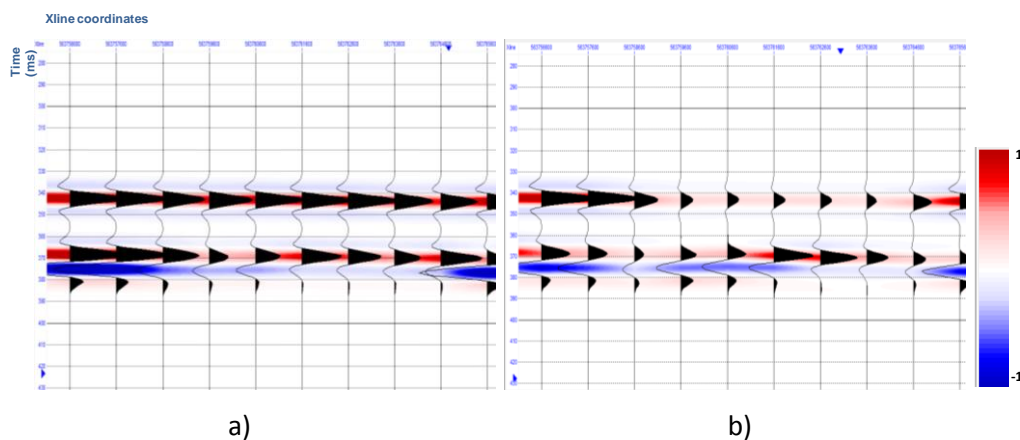
Figure 5-24: a) Detail of the injection zone in the baseline volume. b) Injection zone in the monitoring volume. There is a noticeable reduction of the amplitude (approximately 30%) and time delay (1 ms).

Figure 5-25 is the difference between the monitor and baseline volumes from an inline and crossline perspective. It is possible to observe a difference in amplitude and travel time. As well, a phase change is observed. The difference between both 3D volumes proves to be a more feasible way to appreciate the changes that seemed subtle for individual sections. In terms of size of the plume, it was found that for the first part of the plume (Seal-LP), the diameter is equal to the model. In the second part of the

plume (LP-E) there is an over estimation of the size caused by the presence of gas in the overlying section. In terms of the individual annular disks resolution, it is not possible, in the first disk, to distinguish the interfaces of the transition zone; however for the second disk, it is possible to see a perturbation in the traces that might be attributed to the annular interface. Figure 5-26 shows the 3D perspective of the CO_2 plume and Figure 5-27 illustrates the changes in inline and crossline responses toward the North and East respectively. The anomaly affects the reflector under the injection zone as well. Finally, Figure 5-28 shows a time slice of the differential volume at 338ms (Seal-LP) and 377ms (LP-E), where the location and shape of the CO_2 plume inside the survey is evident.
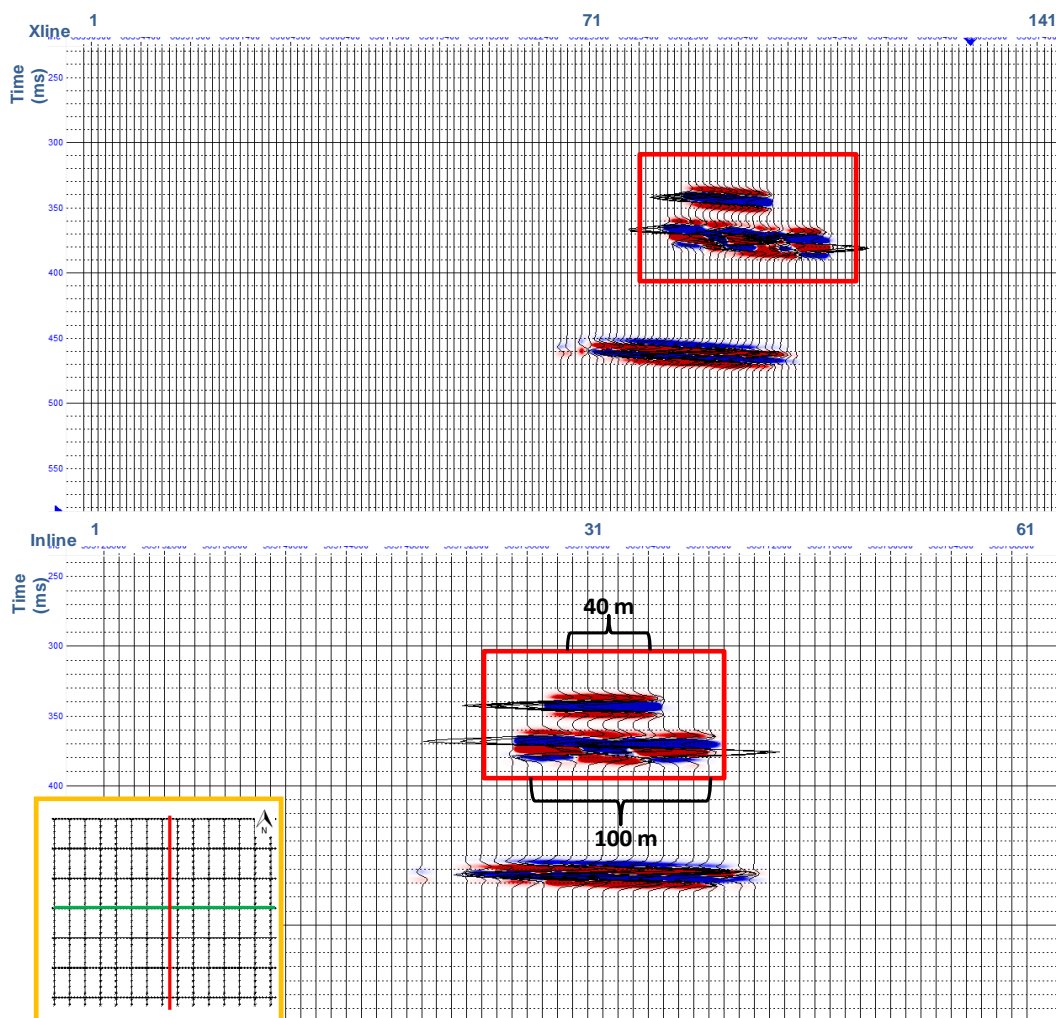
Figure 5-25: Inline (top) and crossline (bottom) view of the volume resulting from the difference between the original model and the CO_2 saturated. The area of injection is marked in a red square.
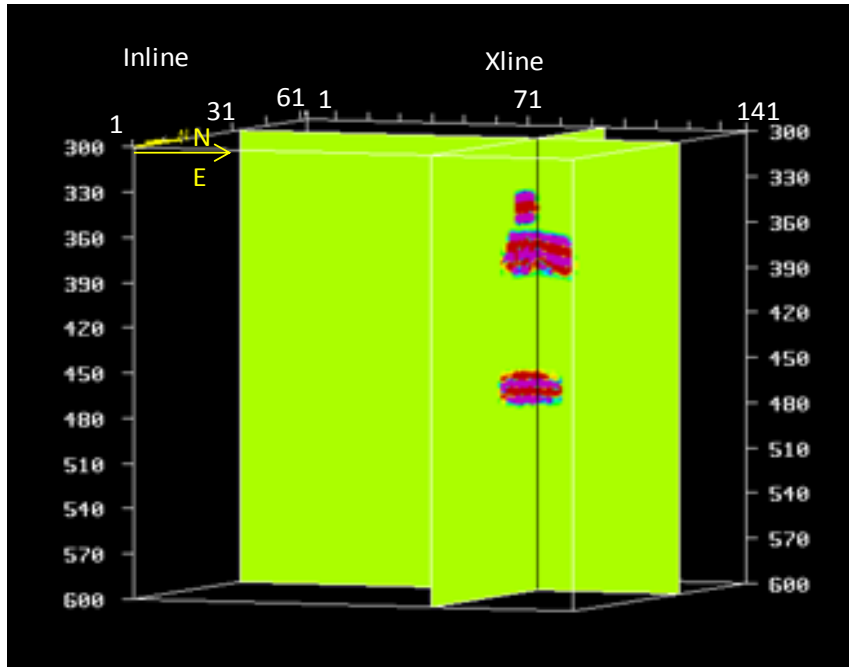
Figure 5-26: 3D view of the difference volume. The anomaly is evident in the area of injection.
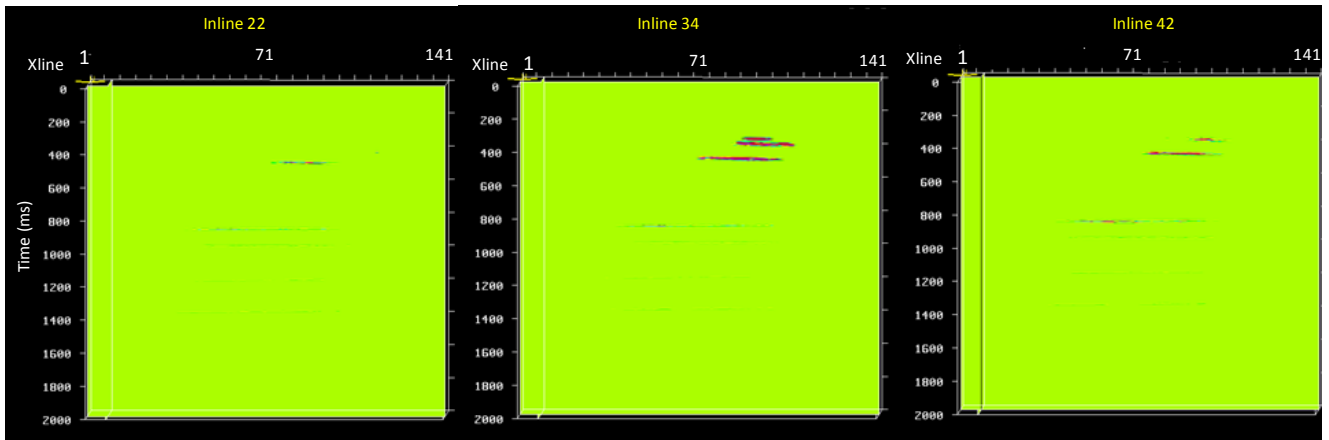
a)
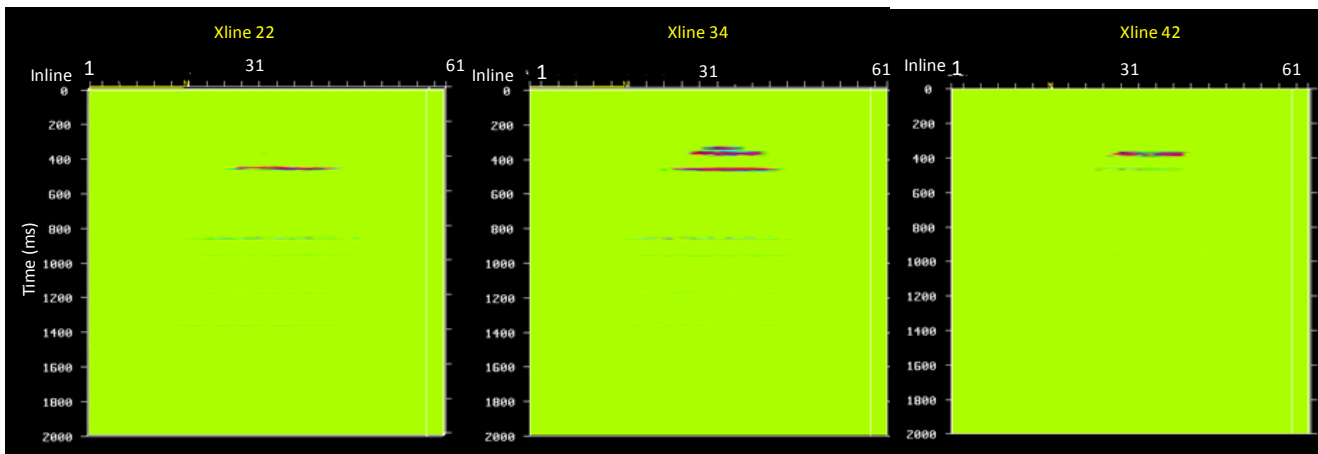
b)

Figure 5-27: (a) inline section from south to north and (b) crossline view from west to east.
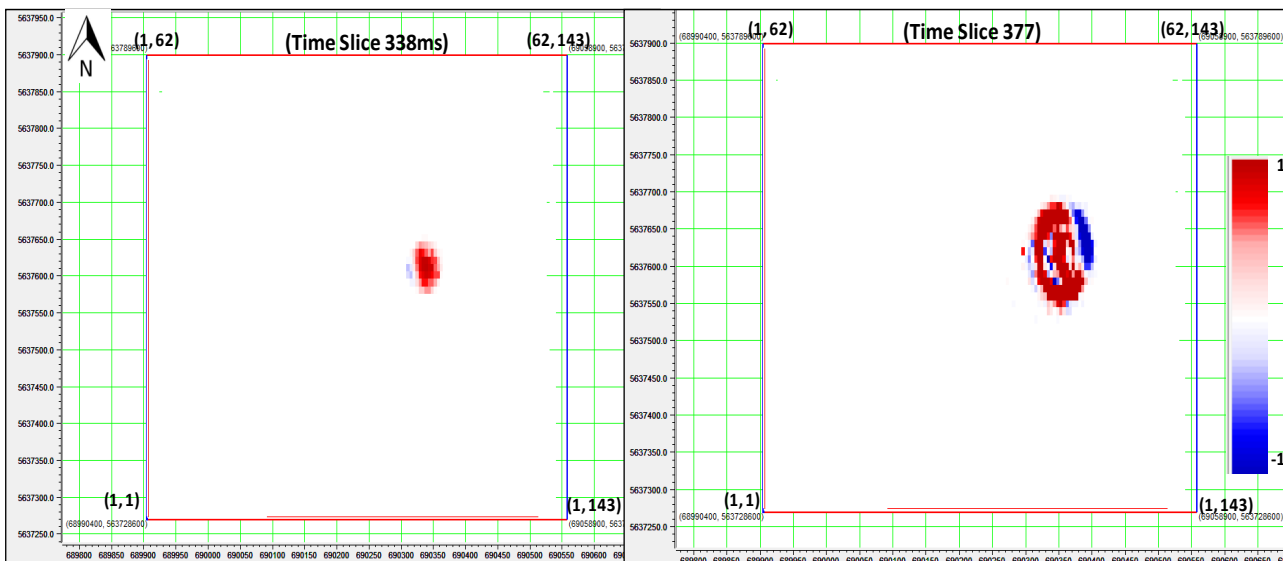
a)

b)

Figure 5-28: Time slices of difference volume (a) at 338 ms and (b) at 377 ms, showing the position on the CO_2 plume.

5.4 Conclusions

The model developed attempted to represent the study site and its geology, based on the seismic data acquired during 2010 field school. Using Norsar3D software, a baseline model and a post-injection model, which includes the CO_2 plume, were obtained. The plume was estimated for 3000 tonnes of CO_2, which is the expected injected amount after 3 years, and 50% CO_2 saturation. The plume size and shape was calculated using volumetric principles and the assumption of radial dispersion. From the resulting seismic volumes it is possible to observe a difference in seismic amplitude and time delay of the reflectors in the injection zone and below it. The changes caused by the presence of CO_2 are recognizable by subtracting the baseline volume from the monitor volume. The reflection time delay measured for the Lower Paskapoo and Edmonton Formations is approximately 1ms; this is a subtle change but it is possible to detect given high quality seismic data. However, even this small change causes considerable changes in the seismic response, and is observable on the difference between the monitor and baseline volumes. The change in reflection amplitude, from the baseline to monitor surveys, is approximated 50%. Corroborating the conclusion of Chapter 4, from these values it is not possible to obtain a certain correlation between amplitude and saturation, because of the non-linear relationship between the velocity change and CO_2 saturation.

Chapter Six: Conclusions

6.1 Discussion

The main goal of the dissertation was to assess the feasibility of monitoring relatively small amounts of CO_2 in the Lower Paskapoo Formation at Priddis area, Alberta. The task is based on the detection of changes in seismic patterns due to the fluid injection. The study was divided in two main parts, first, fluid substitution and second, seismic modelling. For the first part, a Gassmann approach was used in order to recognize the variation in physical properties by replacing the initial 100% water saturated porous space by gradual injection of super-critical CO_2. The target of injection was the Basal Paskapoo sandstone. The initial properties were obtained from a well log close to the University of Calgary land, assuming the continuity of the formation characteristics across the area. The main properties to evaluate were: P-wave velocity, S-wave velocity, V_P/V_S ratio and time shift. In addition, AVO Shuey's approximation was applied showing reduction in P-wave reflectivity with CO_2 saturation and offset.

The second part of the methodology corresponds to seismic modelling; 2D and 3D geological models were generated, in both cases for a baseline scenario as well as a post-injection case. A simulated plume was estimated knowing the final CO_2 volume and applying volumetric calculations. The properties of the plume were taken from Gassmann calculations. Finally the seismic models were created and the monitoring results obtained and assessed.

Six fundamental conclusions can be summarized from the main results of this study:

- Basal Paskapoo Formation (specifically at Priddis area and at approximated 770 m depth) has suitable qualities for a test CO_2 geological storage site; it has considerable section of clean sandstone and being a shallow objective, will reduce monitoring complexities and cost. The analysis of fluid substitution and seismic modeling shows that CO_2 injected in the shallow sandstone of Paskapoo Fm. can

be detected by using time-lapse seismic surveys, showing considerable alteration of seismic patterns even with low CO_2 saturation values.

- Using Gasmann fluid substitution it was found that: P-wave velocity drops quickly from 0 to 0.2 CO_2 saturation, with slight decrease at higher saturations, the average P-wave velocity decrease is 7%, average S-wave velocity increase is 0.6 %, average V_p/V_s decreases by 8% and the two-way time delay trough the reservoir is 1.2 ms. The S-wave velocity increment is directly proportional to the CO_2 saturation but the magnitude of this change is very small in comparison with P-wave velocity variations, therefore it might not be crucial in the monitoring of the CO_2 plume.

- AVO analysis proves to be sensitive in the detection of CO_2 saturation changes, especially through the evaluation of Shuey's parameter *A* (zero offset) and *B* (gradient). These parameters include P-wave velocity, S-wave velocity and density, reflecting, in the final result, the alterations in all of them given the fluid changes. Parameter *A* decreases approximately 25% and *B* decreases approximately 13% with increasing CO_2 saturation, having again the major decrease at low saturation stages. *A* has a slight decrease for later stages of saturation and *B* has a subtle increment, similar to the P-wave vs. CO_2 saturation trend. The changes in Shuey's parameters are considerably high in comparison with P-wave and S-wave velocity changes evaluated earlier from the Gassmann approach. The reservoir type is a high impedance sand that leads to a Class 1 AVO, were the P-wave reflectivity decrease with the offset (or angle of incidence), reaching negative values at the far offsets.

- The seismic methodology applied in the CO_2 injection process has proven to be an efficient technique for monitoring changes at a large scale. Under the conditions presented for the Basal Paskapoo Fm., it was possible to evaluate changes through 2D and 3D seismic modelling. First, it was very important that an accurate simulation of the stratigrapy and structure at the Rothney Astrophysical Observatory is realized in order to generate a realistic baseline scenario. Second, it was important to evaluate the initial rock properties and the

results after the fluid substitution in order to assess the feasibility of seismic detection of the plume after injecting CO_2.

- The presence of the CO_2 plume was detected in the seismic volume by direct interpretation of the seismic sections in the injection zone, but more effectively by performing the difference between the baseline model and the monitor model. There were noticeable changes in amplitude and time delay in the presence of CO_2. A P-wave velocity decrease, diminished reflectivity coefficient of the top reflector of the reservoir and increasing travel time to reach the basal reflector were observed. Also, the reflectors below the injection zone are affected by the time shift. The reflection time delay measured for the Lower Paskapoo and Edmonton Formations was approximately 1ms.

- In addition to the seismic model, it is important to include reservoir modelling; in this case Schlumberger provided a simulation of the different injection scenarios showing the extent and pressure distribution of the plume. The reservoir model proves that injection would not represent a hazard, the migration up dip will not reach shallow depths and most of the CO_2 will be dissolved after 100 years of shut in down the injection.

6.2 Recommendations

In the course of this study some assumption and idealizations have been included; starting by the intrinsic considerations of Gassmann and an ideal baseline scenario with 100% water saturation. In addition, the physical properties of the target formation and other tops were estimated, taking into account the log information of one well that is not exactly in the area of injection. In terms of plume design, the calculation of shape and size is a simplified case that only attempts to estimate the plume and verify that it can be detected in seismic. In order to get more realistic scenarios it is recommended to evaluate several factors in more detail, such as:

- The initial fluid composition of the aquifer in terms of mineral concentration and density values. In the current study it was considered fresh water with 1000 kg/m^3 density. The presence of different minerals and saturation levels will affect the

dissolution rate of the CO_2. In addition, the reaction water-CO_2 and the generation of carbonates were not taken into account in the post-injection seismic modelling scenario.

- A more detailed study of the effective porosity and permeability. These factors are crucial in order to define the level of diffusion of the CO_2 in the aquifer and therefore, the radius of the expanding plume. Also, it is important to consider the total volume of water, as this is fundamental in the dissolution process, knowing that 3gm of CO_2 will need 100 ml of water to be dissolved.

- The buoyancy of the supercritical CO_2, which is related to the density difference of the dissolved fluid and the surrounding media. This will affect also the diffusion process.

All these elements will have an effect in the plume estimation, and very important element to take into account during the seismic modelling, especially in order to verify if it is possible to detect the CO_2 in seismic data. Given the basic calculations proposed here, it was assessed for 50% CO_2 saturation, having a 70 Hz seismic wavelet and 35 m thickness of reservoir; the minimum amount of CO_2 that can be detected is 300 tonnes. This volume will produce a 30 m diameter plume, which is in the limit of the horizontal resolution for the seismic data modelled. But the size of the plume can change after we take into account all the elements previously mentioned.

In addition, it would be reasonable to consider what would be the most reliable factor in the long term storage. Are we relying in the dissolution of the CO_2 in the aquifer? Is there enough water volume to dissolve the expected amount of CO_2? Or is our major certainty is the trapping of the CO_2 under the shale seal proposed here? In this case, is this reliable in the long term given the buoyancy of the CO_2? What is the real permeability of this seal?

There are many elements that need to be confirmed through more detailed studies; nevertheless, this dissertation represents one of the first approaches to evaluate the possible CO_2 injection in shallow sandstone aquifers in Alberta. Some complexities can be added to the methods used, but even with all the mentioned assumptions, the present work can be used as guideline to analyze the feasibility of monitoring CO_2 in any other

sandstone aquifer. It is been demonstrated the potential of using Basal Paskapoo sandstone as a CO_2 geological storage site, but also, the results and methodology can be extrapolated to other locations with similar stratigraphy.

References

Bachu, S., 1995, Synthesis and model of formation water flow in the Alberta Basin, Canada: American Association of Petroleum Geologists Bulletin, 79:1159-1178.

Bachu, S., Gunter, W.D., and Perkins, E.H., 1994, Aquifer disposal of CO_2: hydrodynamic and mineral trapping: Energy Conversion and Management, 35:269-279.

Bachu, S., Michel Brulotte, Matthias Grobe and Sheila Stewart, 2000, Suitability of Alberta Subsurface for Carbon-Dioxide Sequestration Geological Media: Aberta Energy and Utilities Board, Earth Science Report: 11, 1-88.

Batzle, M., and Wang, Z., 1992, Seismic properties of pore fluids: Geophysics, 57, 1396–1408.

Benson, S., and Lawrence Berkeley, 2008, Carbon Dioxide Capture and Storage in Underground Geologic Formations: "The 10-50 Solutions: Technology and Policies for a Low-Carbon Future".

Bertram, M., Kevin L. Bertram, Kevin W. Hall, and Eric V. Gallant, 2010, Seismic acquisition projects 2010: Crewes Research Report, vol 22.

Brown, S. and Gilles Bussod, 2007, AVO monitoring of CO_2 sequestration: A benchtop-modeling study, The Leading Edge, 1576-1583.

Castagna, J. P., and Smith, S. W., 1994, Comparison of AVO indicators: A modeling study: Geophysics, 59, no. 12, 1849–1855.

Chadwick A., R. Arts, O. Eiken, P. Williamson, and G. Williams, 2006, Geophysical Monitoring of the CO_2 Plume at Sleipner, North Sea: Advances in the Geological Storage of Carbon Dioxide, 303-314.

Clearbout, J. F., 1975, Slant-stacks and radial traces: Stanford Expl. Project Report SEP-5, 1-2.

Dawson F., C. Evans, R. Marsh, and R. Richardson, 2008, Uppermost Cretaceous and Tertiary Strata of the Western Canada Sedimentary Basin, Alberta Geological Survey, Chapter24,
http://www.ags.gov.ab.ca/publications/wcsb_atlas/a_ch24/ch_24.html#scoll2

Demchuk, T.D. and Hills, L.V. 1991. A re-examination of the Paskapoo Formation in the central Alberta Plains: the designation of three new members. Bulletin of Canadian Petroleum Geology, v. 39, no. 3, p. 270-282.

Dix, H. C., 1955, Seismic velocities from surface measurements: Geophysics, 20, 68-86.

Domenico, S.N., 1977, Elastic properties of unconsolidated porous sand reservoirs: Geophysics, v. 42, p. 1339–1368.

Frailey, S, 2009, Methods for Estimating CO_2 Storage in Saline Aquifers, *Energy,* 1, 2769-2776. Elsevier Science Ltd, Oxford.

Gibson, D.W. 1977. Upper Cretaceous and Tertiary coal-bearing strata in the Drumheller-Ardley region, Red Deer River Valley, Alberta. Geological Survey of Canada, Paper 76-35, 41 p.

Grasby S., Zhuoheng Chen, Anthony P. Hamblin, Paul R.J. Wozniak and Arthur R. Sweet, 2008,Regional characterization of the Paskapoo bedrock aquifer system, southern Alberta, Can. J. Earth Science, 45, 1501-1516

Hall K., Peter Gagliardi and Don C. Lawton, 2010, GPS accuracy part 2: RTK float versus RTK fixed: Crewes Research Report, vol 22.

Hashin, Z., and Shtrikman, S., 1963, A variational approach to the elastic behaviour of multiphase materials: J. Mech. Phys. Solids, 11, 127-140.

Henley D. C. and Gary F. Margrave, 2008, Gabor deconvolution: surface-consistent and iterative: Back to Exploration, Canadian Society of Exploration Geophysics (CSEG), Alberta, Canada. Expanded abstract.

Henley, D. C., 1999, The radial trace transform: An effective domain for coherent noise attenuation and wavefield separation, 69th Ann. Internat. Mtg., Soc Expl. Geophys. Expanded Abstract, 1204-1207.

Henley, D. C., 2003, Coherent noise attenuation in the radial trace domain: Geophysics, vol 68, no. 4, p. 1408-1416.

Hitchom B., 1984, Geothermal gradients, hydrodynamics, and hydrocarbon occurrences, Alberta, Canada: A*APG Bulletin*,1984, vol 68; no. 6, p. 713-743.

Hovorka, S. Surveillance of a Geologic Sequestration Project: Monitoring, Validation, Accounting. GCCC (Gulf Coast Carbon Center) Digital Publication Series #08-01, 2008.

Isaac H. and Don C. Lawton, 2010b, Processing of the 2010 field school 3D and 2D seismic data from Priddis, Alberta J, Crewes Research Report, vol 22.

Isaac H., 2008, Promax Processing Course: University of Calgary, CREWES.

Isaac, H. and Don C. Lawton, 2010a, Integrated geological and seismic site characterization at Priddis, Alberta: Crewes Research Report, vol 22.

Lawton D., Malcolm B. Bertram, Robert R. Stewart, Han-xing Lu and Kevin W. Hall, 2008, Priddis 3D seismic Surrey and development of a training center, Crewes Research Report, vol 20.

Lerbekmo, J.F., Evans, M.E., and Hoye, G.S. 1990. Magnetostratigraphic evidence bearing on the magnitude of the sub-Paskapoo disconformity in the Scollard Canyon-Ardley area of the Red Deer Valley, Alberta. Bulletin of Canadian Petroleum Geology, v. 38, p. 197-202.

Margrave, G. F., Gibson, P. C., Grossman, J. P., Henley, D. C., Iliescu, V., and Lamoureux, M. P., 2004, The Gabor Transform, pseudodifferential operators, and seismic deconvolution, Integrated Computer-Aided Engineering, 9, 1-13.

Margrave, G. F., Lamoureux, M. P., Grossman, J. P., and Iliescu, V., 2002, Gabor deconvolution of seismic data for source waveform and Q correction: 72nd Ann. Internat. Mtg: Soc. of Expl. Geophys, 2190-2193.

Piri, M., Prevost, J. H., and Fuller, R., 2005, Carbon Dioxide Sequestration in Saline Aquifers: Evaporation, Precipitation and Compressibility Effects: Fourth Annual Conference on Carbon Capture and Sequestration DOE/NETL.

Shuey, R. T., 1985, A simplification of the Zoeppritz equations, Geophysics, 50, 509-614.

Slotboom R., Donald C. Lawton and Deborah A. Spratt , 1996, Seismic interpretation of the   triangle zone at Jumping Pound, Alberta: Bulletin of Canadian Petroleum Geology, vol 44. no. 2, p. 233- 243.

Smith T., Carl H. Sondergeld, and Chandra S. Rai, 2003, Gassmann fluid substitutions: A tutorial, Geophysics, vol. 68, no. 2, p. 430-440.

Sodagar T. and Dr. Don C. Lawton, 2009, Seismic modelling of fluid substitution in Redwater Reef: Crewes Research Report, vol 21.

Stockmal G., Paul A. MacKay, Don C. Lawton and Deborah A. Spratt, 1996, The Oldman Rirver   triangle zone: a complicated tectonic wedge delineated by new structural mapping and seismic interpretation: Bolletin Canadian Petroleum Geology, vol 44, no. 2, p. 202-214.

Wright G., M. Mechan and D. Potter, 2008, Structure and Architecture of the Western Canada Sedimentary Basin; Alberta Geological Survey, Chapter 3, http://www.ags.gov.ab.ca/publications/wcsb_atlas/a_ch03/ch_03.html

Wuerdemann, H., Moeller, F., Kuehn, M., Heidug, W., Christensen, N.P., Borm, G., Schilling, F.R, 2009, CO_2SINK-From site characterisation and risk assessment to monitoring and verification: One year of operational experience with the field laboratory for CO_2 storage at Ketzin, Germany: International Journal of Greenhouse Gas Control, vol. 4, n. 6, p. 938-951

Xu H., 2006, Short Note Calculation of CO_2 acoustic properties using Batzle-Wang equations: Geophysics, vol. 71, no. 2, p. F21-F23.